Investigation of $CaIr_{1-x}Pt_xO_3$ and $CaIr_{0.5}Rh_{0.5}O_3$: Structural properties, physical properties and stabilising conditions for post-perovskite oxides

Shigeto Hirai

School of Geosciences, Centre for Science at Extreme Conditions

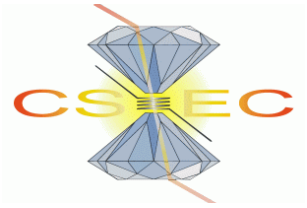

A dissertation submitted to the University of Edinburgh

for the degree of Doctor of Philosophy

5th of January, 2011

Abstract

Our understanding of the nature of Earth's D" region was changed significantly by a recent finding by Murakami et al. (2004)[1], who revealed a phase transition from perovskite to post-perovskite structure in $MgSiO_3$ at about 125 GPa and 2500 K, corresponding to conditions of the lowermost mantle. A perovskite to post-perovskite phase transition accounts for many unusual features of the D" region, including its notable seismic anisotropy, and also accounts for the unusual topology of the D" discontinuity. However, the experimentally synthesised post-perovskite phase of $MgSiO_3$ is not quenchable to ambient conditions, which means that many of its physical properties remain difficult to determine. On the other hand, there are several post-perovskite oxides, $CaIrO_3$, $CaPtO_3$, $CaRhO_3$ and $CaRuO_3$, which can be quenched to ambient conditions, maintaining their structure.

High pressure synthesis of $CaIr_{1-x}Pt_xO_3$ solid solutions (x = 0, 0.3, 0.5, 0.7) and $CaIr_{0.5}Rh_{0.5}O_3$ was conducted at the University of Edinburgh and Geodynamics Research Center, Ehime University, and structures and physical properties of these novel post-perovskite materials determined. Substantial [100] grain growth was observed in all solid solutions leading to pronounced texture even in powdered materials. Temperature-independent paramagnetism above 150 K and small magnetic entropy observed in heat capacity measurements suggest that $CaIrO_3$ is an intrinsically weak itinerant ferromagnetic metal, while electrical resistivity measurements show that it is a narrow bandgap semiconductor, possibly due to grain boundary effects. $CaIrO_3$

undergoes a magnetic transition at 108K and possesses a saturated magnetic moment of 0.04 μ_B. Doping with Pt or Rh induces Curie-Weiss paramagnetism and suppresses the magnetic transition. The anisotropic structure and morphology of $CaIrO_3$ combined with the Ir^{4+} spin-orbit coupling results in a large magnetic anisotropy constant of 1.77 x 10^6 Jm^{-3}, comparable to values for permanent magnet materials.

A new high-pressure phase of $CaIr_{0.5}Pt_{0.5}O_3$ was synthesised at 60GPa, 1900K using a laser-heated DAC (diamond anvil cell) at GRC, Ehime University. Its Raman spectra resemble those of perovskite phases of $CaIrO_3$ and $CaMnO_3$, implying that $CaIr_{0.5}Pt_{0.5}O_3$ undergoes a post-perovskite to perovskite phase transition with increasing pressure. I estimate an increase in thermodynamic Grüneisen parameter γ_{th} across the post-perovskite to perovskite transition of 34 %, with similar magnitude to $(Mg,Fe)SiO_3$ and $MgGeO_3$, suggesting that $CaIr_{0.5}Pt_{0.5}O_3$ is a promising analogue for experimentally simulating the competitive stability between perovskite and post-perovskite phase of magnesium silicates in Earth's lowermost mantle. Such estimation is reliable since the estimated and directly calculated thermodynamic Grüneisen parameter γ_{th} from heat capacity show consistent values. The marked effect that Pt has on stabilising the post-perovskite structure in $CaIr_{1-x}Pt_xO_3$ solid solutions explains why the post-perovskite to perovskite phase transition has not been observed for $CaPtO_3$ in contrast to other quenchable post-perovskite oxides: $CaIrO_3$, $CaRhO_3$ and $CaRuO_3$.Work presented here demonstrates that $CaIrO_3$ solid solutions can be used to provide new insight into factors stabilising post-perovskite structures in Earth's lowermost mantle.

1. Introduction to post-perovskite

1.1 The history and importance of post-perovskite

The physical state of minerals in the D” region of the Earth’s lower mantle, just above the core-mantle boundary, is still not fully understood. The lower mantle is mainly composed of (Mg,Fe)SiO_3 perovskite (containing additional Al and other minor elements) and (Mg,Fe)O magnesiowüstite, which together make up about 90% of its volume (Kesson et al., 1998) [2]. However, a number of unusual seismic properties of the Earth’s lowermost lower mantle are not adequately explained by a silicate-perovskite dominated lithology. The so-called D” discontinuity is observed in many regions around the world approximately 200 - 300 km above the core-mantle boundary, and is marked by an increase of up to 3.0 % in both S- and P-wave velocities (Lay et al., 1998)[3]. On the basis of global seismic tomography, Sidorin et al.(1999)[4] proposed a model of a possibly ubiquitous seismic discontinuity atop the D” layer due to a solid–solid phase transition with Clapeyron slope of 6MPaK^{-1}. The increase of seismic velocities atop the D” layer was attributed to the increase of bulk and shear moduli at the transition. At that time this model lacked direct evidence because no relevant phase transition had been observed in the major constituents of the lower mantle, $MgSiO_3$ perovskite and magnesiowustite. Any such phase transition would also have to account for the marked seismic anisotropy of the D” region, which again cannot be adequately explained by a perovskite-dominated lithology in D” layer. S-waves traverse the mid-mantle (where perovskite dominates the lithology) with little shear-wave splitting, while a considerable splitting of S-waves takes place in the D” region. These observations imply that the D”

layer has a large-scale anisotropic structure. Evidence for such anisotropy has been found under the circum-Pacific regions, where the horizontally polarized S-wave velocity is faster by 1 to 4 % than the vertically polarized S-wave velocity [3]. Since such polarization anisotropy tends to correspond to regions with a D" discontinuity, it is expected that compounds in the D" region adopt a structure which is more anisotropic than the perovskite structure. Our understanding of the nature of the D" region was changed significantly in 2004 following the discovery by Murakami et al.(2004)[1] of a phase transition from perovskite to post-perovskite structure in $MgSiO_3$ at about 125 GPa and 2500 K from a series of *in-situ* X-ray diffraction measurements using a laser-heated diamond-anvil cell. These conditions coincide with those of the lowermost mantle, implying that the perovskite to post-perovskite transition could account for the D" discontinuity. Meanwhile, Oganov /Ono et al. (2004)[5] reported that Fe_2O_3 also undergoes perovskite to post-perovskite transition at 60 GPa. The post-perovskite phase of $MgSiO_3$ is denser than perovskite by 1.4 % [1] and has the same crystal structure as $CaIrO_3$, with lattice parameters: a =2.456(0) Å, b =8.042(1) Å, c =6.093(0) Å, $\alpha=\beta=\gamma=90°$ [1]. Iitaka et al.(2004)[6] performed first-principles calculations for elasticity and stability for both perovskite and post-perovskite $MgSiO_3$. They found that the anisotropy of the S wave is larger in post-perovskite than in perovskite, which is consistent with their crystal structures. The post-perovskite structure possesses anisotropic connectivity due to its layered structure with the mixture of edge- and corner- sharing octahedral linkage in the layer, while perovskite possesses isotropic connectivity composed of a three dimensional network of corner-sharing octahedra.

Therefore, as long as the post-perovskite phase of $MgSiO_3$ is stable at the lowermost mantle, the marked anisotropy of the S wave due to its anisotropic crystal structure can explain the observed polarized anisotropy in D" layer regions [3]. Currently, there is good agreement between the experimental determination and the ab initio calculations[5] of the stability of post-perovskite structure over the perovskite structure in $MgSiO_3$ at lowermost mantle conditions.

While it is important to conduct further studies on $MgSiO_3$, this post-perovskite phase cannot be quenched to ambient conditions; this is also the case for the post-perovskite type binary oxides of Fe_2O_3[7] , Al_2O_3[44] and Mn_2O_3[8]. When pressure is released after high pressure experiments, the post-perovskite phase of $MgSiO_3$ converts to an amorphous phase, while other oxides revert to their initial phase at ambient conditions. As a result, determining the physical properties of materials possessing post-perovskite structures is difficult. However, there are four post-perovskite oxides which can be quenched to ambient conditions. The post-perovskite phase of $CaIrO_3$ (Hirai et al., 2009)[16] can be synthesised at ambient pressure, while the post-perovskite phase of $CaPtO_3$ (4GPa, 1073K) (Ohgushi et al., 2008)[17], $CaRhO_3$ (6GPa, 1473K) (Yamaura et al., 2009)[18] and $CaRuO_3$ (23GPa, 1223K) (Kojitani and Shirako et al., 2007)[19] need high pressure/temperature conditions for synthesis.

It has been shown that $MgSiO_3$[1] can transform into a post-perovskite phase at high pressure and high temperature, but it is not certain whether the post-perovskite phase exists in Earth's lowermost mantle or fully explains the unusual nature of the core-mantle boundary. For example, uncertainties remain regarding the lower mantle geotherm and how this crosses over the perovskite to post-perovskite transition, and the

effect of minor elements on phase relations. Monnereau et al. (2007)[9] noted sensitivity in the shape of the post-perovskite surface in the D" layer (the so-called D" topology) using a classical harmonic approach to the 3D spherical model of mantle convection (Fig.1.1). D" topology greatly depends on the core-mantle boundary. The temperature range over this region is within 200 K of the temperature of the post-perovskite transition, indicating that the perovskite to post-perovskite transition could, in fact, be reversed several times. This greatly increases the number of parameters to be taken into account, such as the internal heating, the Clapeyron slope, and the temperature that post-perovskite transition takes place. As the lowermost mantle is considered to be characterized by strong chemical heterogeneity due to processes such as the accumulation of subducted slab material, partial melting, and metal-silicate reactions, the effect of compositional elements on the post-perovskite transition must be taken into account. Hirose et al.(2008)[10] conducted direct TEM observation on quenched $(Mg_{0.91}Fe_{0.09})SiO_3$ bulk, which was initially synthesised at conditions above 100 GPa and 1700 K using the laser-heated DAC technique, and found that crystalline grains of perovskite phase are enriched in iron compared to the amorphous phase originating from the post-perovskite phase. Such observation implies that Fe^{2+} incorporation stabilises the perovskite phase over the post-perovskite phase in $MgSiO_3$. On the other hand, the incorporation of Fe^{3+} or Al^{3+} is considered to stabilise the post-perovskite phase of $MgSiO_3$ (Sinmyo et al., 2006)[11]. In order to further determine whether the post-perovskite phase exists in the lower mantle and can account for properties of the D" region, the physical properties of the post-perovskite structure must be examined. In contrast to commercially important perovskite oxides, post-perovskite oxides have not been

investigated as a series, and their physical properties remain poorly characterized and understood. As post-perovskite is a high-pressure phase of perovskite with denser structure, the band gap (between valence band and conduction band in its electronic structure) is expected to be smaller and the Coulomb repulsion is expected to be larger compared to perovskite compounds. Thus, post-perovskite oxides with transition metals are expected to have enhanced novel charge-transport and magnetic properties those transition metal oxides (with perovskite structure) possess. The motivation of this study comes from the fact that little is understood about such novel physical properties of post-perovskite oxides with transition metals and their effect on structural behaviour at high pressure and high temperatures. Apart from the work presented here, high pressure synthesis of a post-perovskite phase starting from an orthorhombic structured perovskite was tried up to 25GPa for $CaMnO_3$, $LaMnO_3$, $LaCrO_3$ and $LaRhO_3$ using a multi-anvil apparatus at Bayerisches Geoinstitut, University of Bayreuth, Germany, which did not succeed (no chemical reaction/ phase transition of the initial perovskite detected) due to the sensitive stability condition of the post-perovskite phase (often unquenchable to ambient conditions) and the large lattice induced strain of the post-perovskite structure, which can only be minimized by the large crystal field and the strong metal-metal bonding of the B-site cations.

Fig. 1.1 The D" topology of the earth with the post-perovskite layer (in grey) based on the model of Monnereau et al. (2007)[9]. The thermal field is depicted through the 2500 K isotherm (in orange) and the isosurface of the thermal anomaly up to -350 K temperature difference (in blue)

1.2 Introduction to post-perovskite structure

For a long time, perovskite was thought to be the densest crystal structure for many AMO_3 (M: transition metal) oxides. The perovskite structure consists of a 3-dimensional corner- sharing MO_6 octahedral network with A cations in the cavites between the MO_6 octahedra, where regular MO_6 octahedra gets distorted and tilted due to the large size and Jahn-Teller effect (effect of stabilising the electronic configuration in the octahedral crystal field) of M cations. However, recently it has been shown that many perovskites can adopt an even denser structure isostructural with $CaIrO_3$ in the space group of *Cmcm* commonly known as post-perovskite structure. Post-perovskite: AMO_3 possesses a structure where MO_6 octahedra share their edges in the *a*-axis direction, and share their corners in the *c*-axis direction forming a layer which is held together by interlayer A-cations.

$CaIrO_3$ [16] is one of the four materials[16],[17],[18],[19] which adopt a post-perovskite structure at ambient conditions. The structure is orthorhombic, with lattice parameters a = 3.1444(1) Å, b =9.8620(3) Å, c =7.2969(2) Å for $CaIrO_3$ (Fig.1.2.1; Hirai et al., 2009) [16].

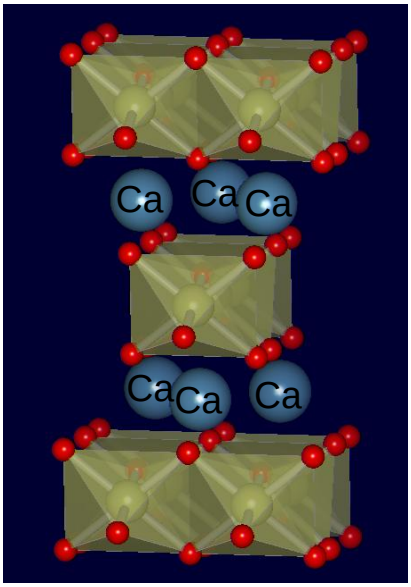

(a)

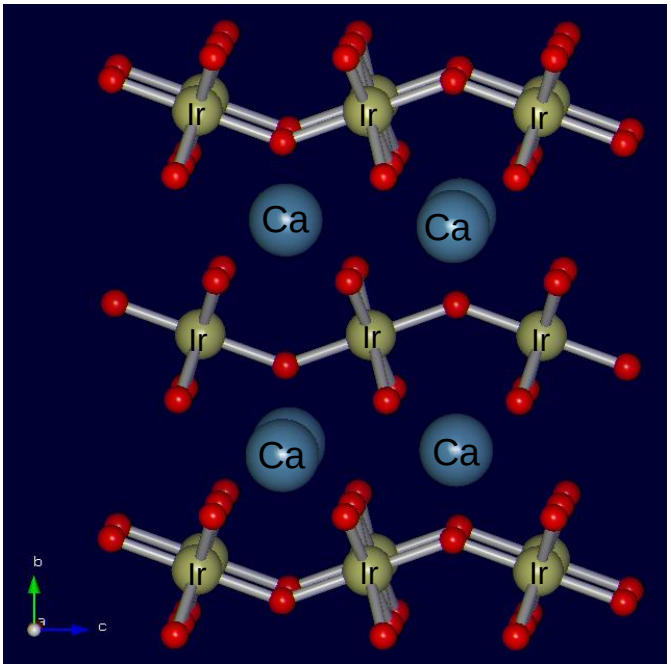

(b)

Fig.1.2.1 Post-perovskite structure in $CaIrO_3$, looking along (a) *c*-axis: edge-sharing octahedra along the *a*-axis and (b) *a*-axis: corner-sharing octahedra along the *c*-axis

The post-perovskite structure was first described for $CaIrO_3$ synthesised at ambient pressure (Rodi et al., 1965)[12]. However, at ambient pressure $CaIrO_3$ post-perovskite can also exist in a metastable state with the perovskite structure, especially in powdered samples (Sarkozy et al, 1974)[13]. In this regard $CaIrO_3$ is a useful material for characterizing factors which determine whether a compound can transform from perovskite to post-perovskite. The sensitivity of different compounds to this phase transition can be seen from the fact that $CaRuO_3$ (ionic radius of Ru^{4+}: 0.62 Å) is perovskite at ambient pressure (He et al., 2001)[14], $CaReO_3$ (ionic radius of Re^{4+}: 0.63 Å) does not adopt any structure (however, $CaIr_xRe_{1-x}O_3$[15] was previously synthesised in perovskite structure), while $CaIrO_3$ (ionic radius of Ir^{4+}: 0.625 Å) is post-perovskite at ambient pressure. Therefore, the cation size is not a decisive factor in the post-perovskite structure, but only a contributing factor in stabilising the structure. A list of known post-perovskite oxides ($CaIrO_3$[16], $CaPtO_3$[17], $CaRhO_3$[18] and $CaRuO_3$[19]) reveals that these oxides have high Crystal Field Stabilization Energies (CFSE) which avoids excessive octahedral distortion and minimizes structural instability held by the anisotropic crystal structure. At the same time, the edge-sharing of the MO_6 octahedra is predicted to come from a highly covalent M-O bond, which can be realized by M-cations with high electronegativity [14], which strongly attract the O_{2P} electrons to the direction of M-cation.

On the basis of this argument, exploration of other potential post-perovskite oxides with high CFSE, such as $CaM^{4d,5d}O_3$, where $M^{4d,5d}$ is Ir, Rh, Pt and Ru, provides an opportunity to determine factors stabilising the post-perovskite structure. These transition metals have a high electronegativity, so also satisfy the covalent nature of the

edge-sharing octahedra in the post-perovskite structure. The presence of heavy transition metal ions in the above $CaMO_3$ (M= Ir, Pt, Rh, Ru) post-perovskites suggests that such phases might have interesting electronic or magnetic properties.

To understand the factors determining the relative stability between perovskite and post-perovskite structure, it is useful to compare the post-perovskite structure with perovskite and hexagonal perovskite–like structures. These structures only differ in the style of octahedral linkages. Before describing the relationship with post-perovskite and these structures, the stacking sequence of perovskite and hexagonal perovskite-like structures will be reviewed.

Materials with layered structures often exhibit polytypism. This is especially true for those which are related to perovskite structure and intermediate between the hexagonal close packing (stacking sequence with ABAB…..) and cubic close packing (stacking sequence with ABCABC……). For example, the structure of AMO_3 (A=Ba, Sr) compounds, where M is a transition metal, consists of close packed AO_3 -layers with M^{4+} cations positioned between the layers forming an octahedral network bounded only by anions. If all the AO_3 -layers are cubic close packed, it leads to an ideal cubic perovskite, while hexagonal close packing leads to a hexagonal perovskite-like structure. The ideal cubic perovskite structure has corner-sharing octahedra only, whereas the hexagonal perovskite-like structure has face sharing octahedra.

In order to understand phase transitions from perovskite to post-perovskite structures, Hirai et al.(2007)[20] found it useful to examine the analogous systems $AIrO_3$ (A= Ba,Sr,Ca) and $AMnO_3$ (Fig.1-2). $BaMnO_3$[21] has a one dimensional chain 2H structure in which adjacent octahedra share faces. $BaIrO_3$[22],[23], $SrMnO_3$[24] and

$SrIrO_3$[25],[26] have 2 dimensional zigzag structures with a mixture of cubic and hexagonal close packing. $CaMnO_3$[64] has an orthorhombic perovskite structure and $CaIrO_3$ has a post-perovskite structure. These systems share the following two characteristics.

1) As the ionic radius of the A-site gets smaller (Ba^{2+}>Sr^{2+}>Ca^{2+}), denser structures are adopted.

2) As the ionic radius of the B-site gets larger (Ir^{4+}>Mn^{4+}), denser structures are adopted

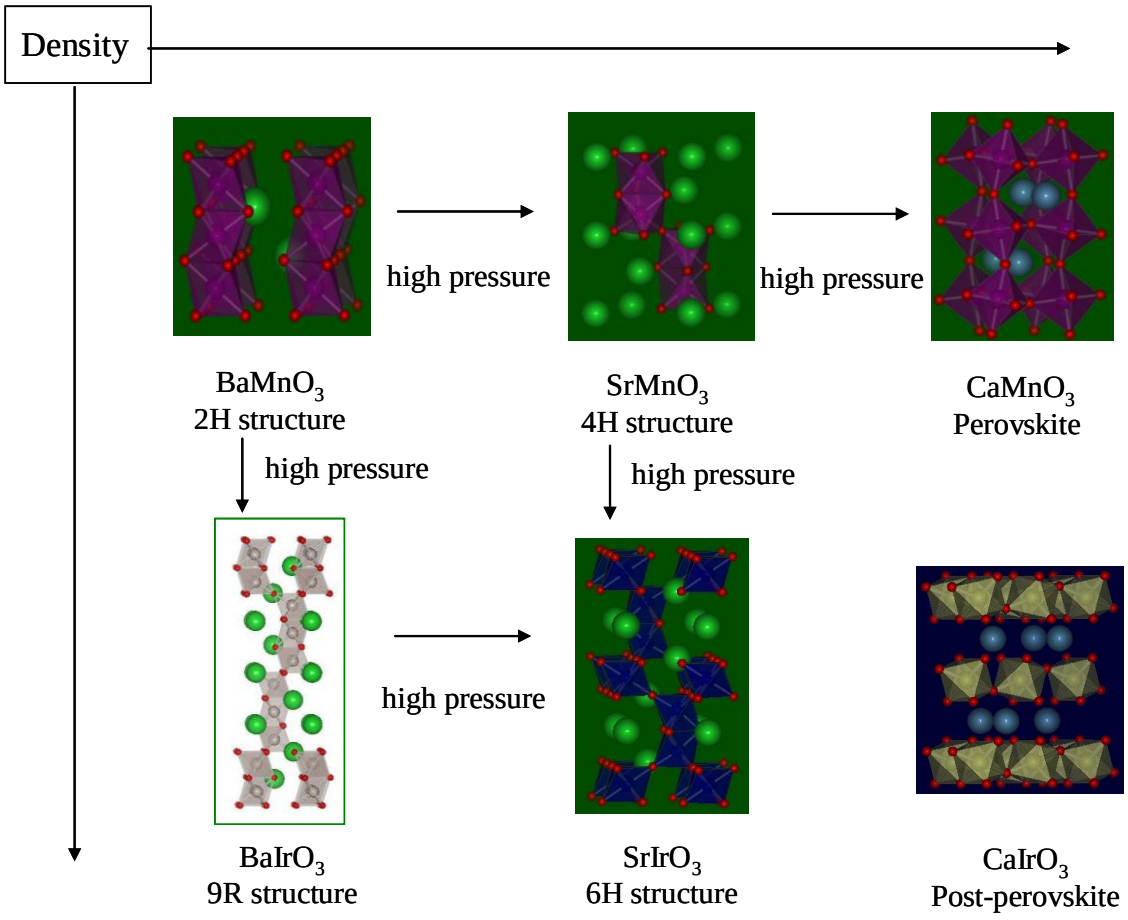

Fig.1.2.2 Crystal structure of $AMnO_3$ and $AIrO_3$ group oxides

(A= Ba, Sr, Ca) (Hirai et al., 2007)[20]

Under high pressure synthesis, $SrIrO_3$ takes the $CaMnO_3$ structure (Longo et al., 1971)[25], showing that perovskite derives from a hexagonal chain structure. In this way, the factor which decides the structure to be post-perovskite is likely to be found from the relation between $CaMnO_3$ and $CaIrO_3$. $CaIrO_3$ is characterized by a layered structure with a mixture of edge- and corner-sharing octahedra, while only corner-sharing octahedra exist in $CaMnO_3$. However, the edge-sharing of the octahedra in $CaIrO_3$ is limited to the *a*-axis direction. Therefore, one would expect that there will be polytypes between $CaMnO_3$ and the $CaIrO_3$ structure, with various mixtures of edge and corner-sharing octahedra in the *a*-axis direction.

The existence of such polytypes was strongly supported in the case of $MgSiO_3$ by Oganov et al. (2005)[27] on the basis of classical and *ab initio* simulations, using a method based on the idea of first-principles metadynamics. In this method, pressure tensors are calculated from constant NVT (N: number of particles, V: volume, T: temperature). Also, by adding a history-dependent Gibbs potential in the simulation, it allows free energy wells to be filled and move the system across the lowest barrier into the domain of another structure. As such, the method is suitable for finding a new pathway of structural transformations. For these simulations Oganov et al.(2005) chose a supercell with 160 atoms (4x1x2 for post-perovskite and 2x2x2 for perovskites) and simulated conditions of 200GPa, 2000K for the classical method and 140GPa, 1500K for the ab initio method. By starting the *ab initio* simulation from perovskite, he first found a 3x1($P2_1/m$) structure characterized by three edge-sharing octahedral units linked by one corner-sharing octahedra in the *a*-axis direction, and then the post-perovskite structure. Classical simulations gave a 2x2 (Pbnm) structure as well as the 3x1 structure,

which has two edge-sharing octahedral units sharing their corners with one another in the *a*-axis direction.

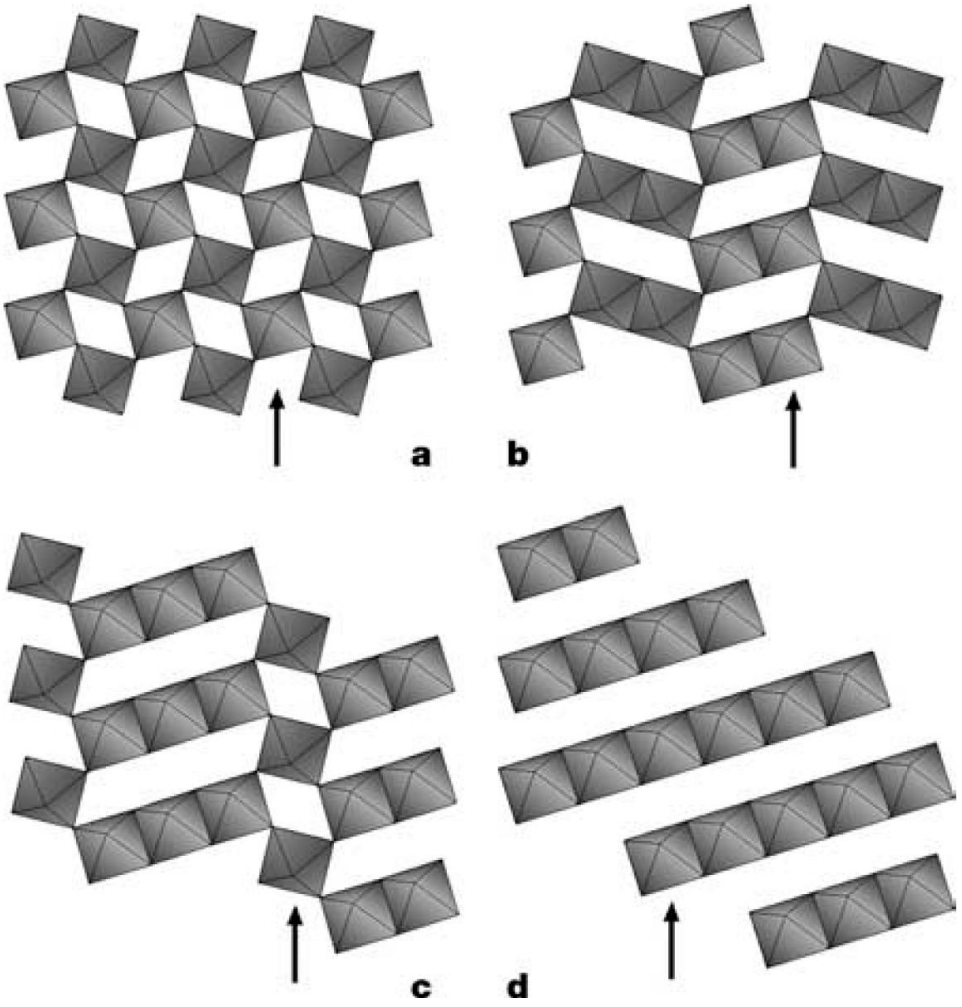

Fig.1.2.3 Crystal structure of $MgSiO_3$ polytypes generated by first-principles metadynamics (Oganov et al., 2005)[25]

(the arrows are representing (0 1 0) planes of $MgSiO_3$ perovskite)

(a) Perovskite (Pbnm) structure (b) 2x2 (Pbnm) structure

(c) 3x1 ($P2_1/m$) structure (d) Post-perovskite structure

The simple sliding of (010) plane of the perovskite structure will generate the 2x2, 3x1 and post-perovskite structures (Fig.1.2.3). Differing only in the stacking sequence, perovskite, 2x2, 3x1 and post-perovskite structure form a continuous family due to (010) slip plane of perovskite structure. Therefore, 2x2 and 3x1 structures are polytypes of post-perovskite structure. These intermediate states are only 20-30meV per atom higher in enthalpy than the post-perovskite structure at 100GPa (100GPa is close to the pressure needed for synthesizing $MgSiO_3$ post-perovskite.) Therefore, these polytypes of $MgSiO_3$ might be easily stabilised by temperature and impurities in the D" layer.

1.3 The structure and the physical properties of post-perovskite oxides at ambient pressure

(1) Structure and physical properties of $CaIrO_3$

The crystal structure of $CaIrO_3$ was solved by Rodi et al.(1965)[12], who synthesised single crystals of $CaIrO_3$ by using a $CaCl_2$ flux method. Single crystal refinement was performed but anisotropic thermal parameters were not refined until 2007, when Hirai et al.[16] revisited the structure in order to find a structural solution with higher accuracy. Other studies have focused on determining the physical properties of $CaIrO_3$. The synthesis of powdered samples of $CaIrO_3$ has been performed at ambient pressure, but it has proved difficult to obtain pure, high-quality samples. The main impurities[13] are metastable $CaIrO_3$ perovskite and Ca_2IrO_4. The metastability of $CaIrO_3$

perovskite has been revealed by DFT studies comparing the energy level of $CaIrO_3$ post-perovskite with $CaIrO_3$ perovskite[28](Stolen et al., 2007). The difficulty of synthesizing pure samples of $CaIrO_3$ post-perovskite can be summarized by the narrow accessible temperature range. A temperature of at least 1273K is required for the synthesis of $CaIrO_3$ post-perovskite, while $CaIrO_3$ decomposes into Ca_2IrO_4 and IrO_2 at 1408K due to volatility of Iridium. In order to minimize such problem, a closed system is required for synthesis. The metastable $CaIrO_3$ perovskite was identified as a $GdFeO_3$-type orthorhombic perovskite by Sarkozy et al.(1974)[13], but no experimental data have been published for the atomic positions or for the refinement of its crystal structure. This is presumably due to the poor quality of metastable $CaIrO_3$ perovskite samples. To date, only physical properties have been studied for the metastable $CaIrO_3$ perovskite. Sakozy et al.(1974)[13] showed that metastable $CaIrO_3$ perovskite is a temperature-independent Pauli-paramagnetic metal. Hirai et al. (2010)[29] suggested that the post-perovskite phase of $CaIrO_3$ is a weak itinerant ferromagnetic (T_c = 108K) metal, and that the large crystal field and strong spin-orbital coupling of Ir^{4+} ($5d^5$) make $CaIrO_3$ a hard magnet with large magnetic anisotropy. The role of Ir^{4+} as a source of spin-orbital coupling has been observed and explained in some iridium-bearing compounds. For example, the mechanism of strong spin-orbital coupling (which comes from the spatially extended 5d state of Ir^{4+} ($5d^5$)) enables the compound to adopt the J_{eff} =1/2 state (where the total magnetic quantum number: J is equal to ½ instead of the spin quantum number S being equal to ½, making the effective magnetic spin: S_{eff} much smaller than in other S = ½ systems). Such J_{eff} =1/2 state of Ir^{4+} ($5d^5$) actually exists for Sr_2IrO_4, which has been proved by use of X-ray resonant scattering (Kim et al., 2008)[30]. On the other hand,

physical properties of $CaIrO_3$ related compounds have not been studied in terms of their strong spin-orbital coupling. The only reported study on solid solutions of $CaIrO_3$ is a metal-insulator transition of $Ca_{1-x}Na_xIrO_3$ (Ohgushi et al., 2006) [31] at x= 0.37 (the whole series was synthesised at 4GPa, 1073K) which has revealed that extended orbitals of 5d electrons mean that the system is in the vicinity of both a metal and an insulator. The paper suggested that in order to further investigate $CaIrO_3$ and related compounds it is essential to understand the role of lattice-electron coupling which originates from strong spin-orbital coupling of 5d transition metals.

Recent discovery of the perovskite to post-perovskite phase transition of $MgSiO_3$ has lead to renewed interest in the post-perovskite oxides, with a number of studies focusing on $CaIrO_3$ [28], [29], [31], [32]. Hirose et al.(2005)[32] performed an ex-situ investigation of the post-perovskite to perovskite transition in $CaIrO_3$, bracketing the phase boundary from 0.9GPa-3.2GPa and 1600-1900K. Unlike the sample synthesised at ambient pressure, the post-perovskite phase of $CaIrO_3$ did not decompose into Ca_2IrO_4 and IrO_2 at high temperature and high pressure. Lattice parameters of both perovskite and post-perovskite phase of $CaIrO_3$ were calculated from diffraction data, although detailed structural refinements of X-ray data were not given. Because of this, the atomic positions and the space group of the perovskite phase of $CaIrO_3$ are still unclear. Recent pressure-temperature dependent monochromatic X-ray powder diffraction studies by Martin et al.(2007)[33] on compressibility and thermal expansion of $CaIrO_3$ show that the interlayer *b*-axis has the largest compressibility and thermal expansion, and that the *c*-axis has a smaller compressibility and larger thermal expansion than the *a*-axis. Such difference between compressibility and expansivity is unusual, but implies that the bulk

modulus at the top and the bottom of the D'' layer could be different, implying variations of S-wave velocities in the D'' region. Recently, Martin et al.(2007)[34] studied the compressibility of $CaIrO_3$ in detail by time-of-flight neutron powder diffraction at high-pressure, and found that CaO_8 polyhedra are more compressible than the IrO_6 octahedra, which agrees with the bond valence theory introduced for post-perovskite compounds by Hirai et al.(2007) [20].

1.4 Post-perovskite structure at high pressure

High pressure studies on post-perovskites have been conducted for only a few materials: $CaIrO_3$[32], $CaRhO_3$[18], $CaRuO_3$[19], $MgSiO_3$ [1] and $MgGeO_3$[35],[36],[61],[64]. The post-perovskite phase of $CaIrO_3$ can be synthesised at ambient pressure using a flux growth method or using an evacuated silica tube in the furnace, while the post-perovskite phase of $CaRhO_3$[18], $CaRuO_3$[19], $MgSiO_3$[1] and $MgGeO_3$[35],[36] can only be synthesised at high-pressure. The phase boundary between perovskite and post-perovskite structure at high P-T has been reported in these materials. The first reported high P-T study on $CaIrO_3$ was performed by Hirose et al.(2005)[32]. They found that the perovskite phase of $CaIrO_3$, which exists as a metastable phase if synthesised at ambient pressure, is stable at 1-3GPa and 1400-1550°C. Based on eight experimental data points, they determined that the Clapeyron slope of perovskite to post-perovskite phase transition is 17(3)MPa/K. Soon after, Kojitani and Furukawa et al.(2007)[37] revisited the equilibrium phase boundary of $CaIrO_3$ and found that it satisfies the equation: P (GPa) = 0.040 T(K) – 67.1, possessing a sharp Clapeyron slope.

While it is important to conduct further studies on $MgSiO_3$, this post-perovskite phase cannot be quenched to ambient conditions; this is also the case for the post-perovskite type transition metal oxides Fe_2O_3[7] and Mn_2O_3[8]. Therefore, the structural properties of $CaIrO_3$[16], $CaPtO_3$[17], $CaRhO_3$[18] and $CaRuO_3$[19] which can be quenched to ambient pressure, become important. The other three oxides were obtained using a multi-anvil apparatus to achieve high pressure-temperature conditions; $CaPtO_3$ (4GPa, 1073K)[17], $CaRhO_3$ (6GPa, 1473K)[18] and $CaRuO_3$ (23GPa, 1223K)[19]. Further studies on these materials have revealed post-perovskite to perovskite structural phase transitions at high pressures and temperatures. These observations imply that the perovskite structure is the high temperature phase and the post-perovskite structure is the high-pressure phase. This is supported by a Raman spectroscopy study of $CaIrO_3$ up to 30GPa (Hustoft et al., 2008)[38] and a synchrotron X-ray diffraction of $CaPtO_3$ up to 40GPa (Lindsay-Scott et al., 2010)[39] which show that the phase transition from post-perovskite to perovskite transition does not occur at room temperature.

2. Introduction to electronic structure, magnetic interaction, spin-orbital coupling effect and polytypes of post-perovskite

2.1 Electronic structure of solids

Solids can be divided into metals, semiconductors and insulators depending on their charge-transport properties. In order to explain the charge-transport property of the solid, it is useful to introduce an energy band model in the picture of electronic structure. The energy bands can be described using molecular orbital theory. The linear combination and overlap of atomic orbitals form molecular orbitals with continuous bands of energy levels which spread over the solid. Since electrons are fermions and two different molecular orbitals are not allowed to occupy the same energy level, molecular orbitals have band gaps between each other. The bandwidth of each orbital band depends on the degree of localization of electrons or the magnitude of the Coulomb repulsion of electrons in the orbital (on-site Coulomb repulsion). The intrinsic charge-transport property of the solid is determined by the highest filled orbital band (valence band) and the lowest empty orbital band (conduction band). In metals, the valence band overlaps with the second highest filled orbital band or with a partially filled orbital band allowing transport of conduction electrons to the unoccupied energy levels. Electrical conductivity of a metal decreases along with the increase of temperature due to the collision between electrons and atoms enhanced by lattice vibrations. In semiconductors and insulators, the band gap between the valence band and the conduction band does not allow the electron transport in the absence of thermal energy or extrinsic effects such as metallic grain boundaries. The band gap (between valence

band and conduction band) of a semiconductor is less than 3eV, while the band gap of an insulator is larger than 3eV. Owing to the thermal excitation that allows a portion of electrons to populate in the conduction band, the electrical conductivity of a semiconductor or an insulator increases along with the increase of temperature. Both in semiconductors and insulators, the effect of lattice vibrations can be ignored under the dominating effect of thermal excitation at high temperatures.

2.2 Magnetic interactions of solids

(1) Localized spin model (Heisenberg model)

In the absence of sufficient thermal energy: k_BT (k_B: Boltzmann constant, T: temperature), electrons in semiconductors and insulators are localized to the orbital bands of each atom due to the energy gap between the valence band and the conduction band. Thus, it is a good approximation to assume that all the electron spins are localized to each atom in semiconductors and insulators. Magnetic ordering in such a localized system is governed by the magnetic exchange interaction between the electron spins localized to each atom. The Heisenberg model describes the quantized energy of magnetic exchange interaction between neighbouring electron spins in the form of a Hamiltonian (H) as:

$H = -2\Sigma J_{ij} S_i S_j$ ($i > j$)

(J_{ij}: exchange constant between the electron spins of the i^{th} and j^{th} atom; Si, Sj: electron spins localized to the i^{th} and j^{th} atom, respectively)

The sign and magnitude of the exchange integral J_{ij} is mainly determined by the

inter-atomic distance and the electronic configuration of the atom *i* and atom *j*, which is the outcome of cation-cation interactions and cation-anion-cation interactions. In order to minimize the magnetic exchange energy, positive exchange integrals lead to ferromagnetic interactions, while negative exchange integrals lead to antiferromagnetic interactions. Cation-cation interaction is based on a electron transfer between the closest neighbouring magnetic cations requiring the direct overlap of electron orbitals, while cation-anion-cation interaction is based on an indirect electron transfer through the intermediate anion between two neighbouring magnetic cations where the sign and magnitude of the exchange integral depends on the cation-anion-cation angle and the electronic configuration of the cation and anion.

(2) Itinerant spin model (Stoner model)

As metals only have conduction electrons, electrons are not localized to the orbital of each atom unlike in semiconductors and insulators. Thus, the Heisenberg model is not suitable for metals. Instead, the Stoner model describes such an itinerant electron system in the concept of a paramagnetic metal (initially having an equal number of up- and down- spins) where the applied magnetic field divides the electron band of conduction electrons into up-spin and down-spin electron bands with different energy levels (Fig.2.2). As the susceptibility of a metal is proportional to the electron density of states at the Fermi energy: $N(E_F)$, the change in the relative number of up- and down-spins (due to the applied field) alters the susceptibility χ as:

$\chi = \chi_p / [1 - J\, N(E_F)]$ ($[1 - J\, N(E_F)]$: Stoner enhancement term)

, where χ_p is the initial susceptibility in the absence of a magnetic field and J is the exchange integral between two parallel spins (either up-spins or down-spins). The Stoner enhancement term is especially important in the case of 5d transition metal oxides since they have a large exchange integral J due to the extending 5d orbitals. If the condition of $J\ N(E_F) > 1$ is satisfied, which is called the Stoner criterion, the instability of the paramagnetic state will alter the system into a either a strong itinerant ferromagnetic metal (the state where all the spins are altered to a parallel configuration) or a weak itinerant ferromagnetic metal (the intermediate state where only a portion of spins are altered to a parallel configuration) .

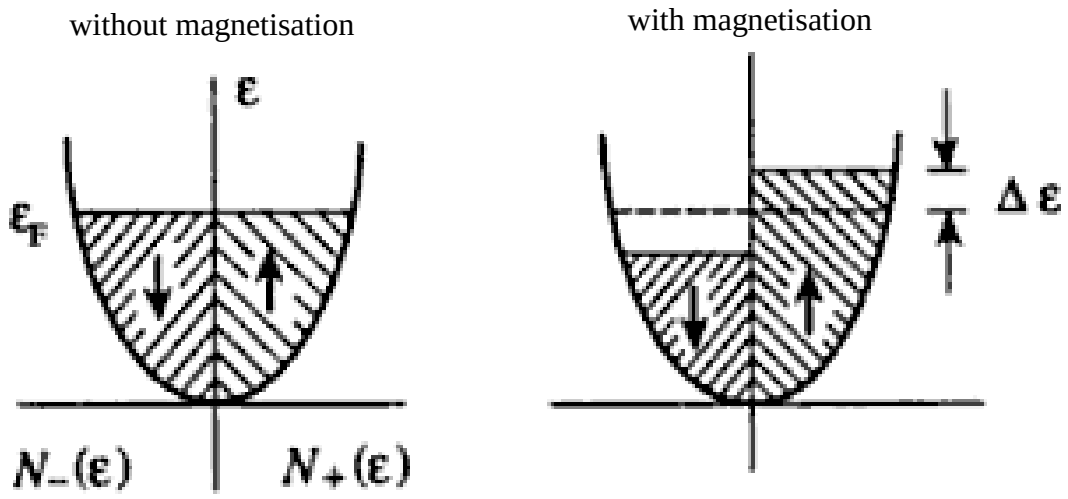

Fig.2.2 Electron density of states without magnetisation and with magnetisation in the picture of Stoner model describing magnetism of metals. ($N_-(\varepsilon)$ and $N_+(\varepsilon)$ denotes the electron density of states with up- and down- spins, respectively; $\Delta\varepsilon$ denotes the gap between the highest filled energy level of electron for metals before and after the magnetisation)

2.3 Spin-orbital coupling effect on 5d transition metal oxides

Recently it has been shown that the Coulomb repulsion in the electronic band combined with strong spin-orbit interactions is responsible for the insulating behaviour of a 5d transition metal: Sr_2IrO_4 (Kim et al, 2008)[30]. While spin-orbital (SL) coupling can be generally treated as a minor perturbation (suppressed by Coulomb interaction) in the description of magnetism ($j = S + L$; j: total angular momentum; S: spin angular momentum, L; orbital angular momentum), the amount of spin-orbit interactions in 5d transition metal is an order of magnitude larger than those in the 3d and 4d transition metal due to the extending 5d orbital which increases the effect of orbital angular momentum. Thus, the spin-orbital coupling is expected to play a significant role in the electronic and magnetic properties of 5d transition metal oxides. In order to explain why Sr_2IrO_4 exhibits unusual weak ferromagnetism with reduced Ir magnetic moments (due to the lowered spin angular momentum), an effective magnetic exchange energy Hamiltonian in the picture of Heisenberg model with not $S = 1/2$ but an effective total angular momentum of spin-orbit integrated $j_{\text{eff}} = 1/2$ state was proposed[30]. A tight-binding model (a model assuming an isolated atom at each lattice point) based on first-principles calculations[30] suggested that if the $j_{\text{eff}}= 1/2$ spin-orbit integrated state exists, it will remain robust even in the presence of on-site Coulomb interactions (Coulomb repulsion of electrons in the same orbital band). Such novel $j_{\text{eff}}= 1/2$ ground state in Sr_2IrO_4 was firstly tested by first principle calculations[30] and then experimentally revealed by X-ray resonant scattering (Kim et al, 2009)[40]. Further investigations of the electronic structures of the $Sr_{n+1}Ir_nO_{3n+1}$ (n = 1, 2, and infinite)

series by Moon et al.(2008)[41] demonstrated a Mott insulator-metal transition with a change of bandwidth as *n* increases(Fig.2.3), suggesting that the change of crystal structure (or the change of parameters such as pressure) accounts for the closing up of the band gap in the spin-orbit integrated j_{eff} = 1/2 state. The presence of a spin-orbit integrated state with strong spin-orbit interactions in Ir^{4+}-bearing transition metal oxides allow abundant opportunities for studies in 5d transition metal oxides, such as $CaIrO_3$ and its solid solutions: $CaIr_{1-x}M_xO_3$ (M: transition metal).

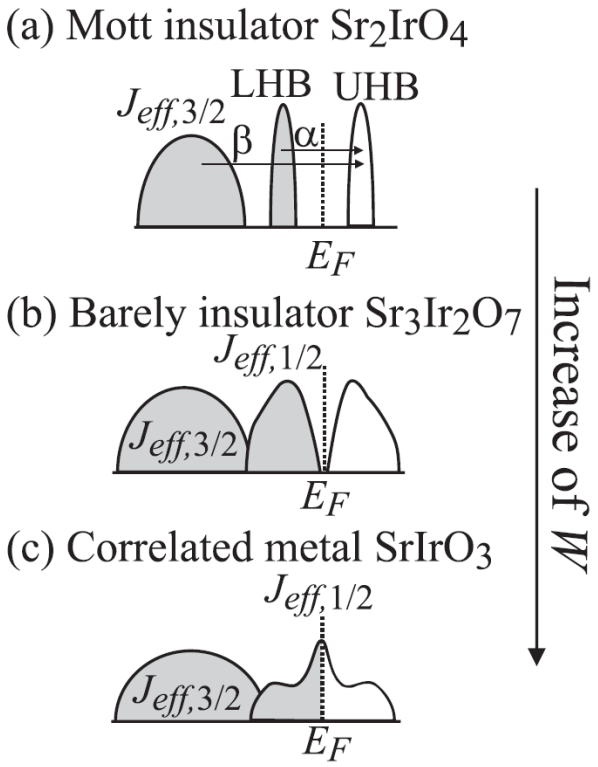

Fig.2.3 The electronic band structure on the basis of j_{eff} = 1/2 model in $Sr_{n+1}Ir_nO_{3n+1}$ (n = 1, 2, and infinite) series established by the strong spin-orbital coupling character of Ir^{4+} (: $5d^5$) (Moon et al., 2008)[41] LHB: lower Hubbard band (which is a valence band), UHB: Upper Hubbard band (which is a conduction band), *W* : band-width

(α and β denote the excitation energy for the photo-induced conductivity of Sr_2IrO_4)

2.4 Perovskite structure

Perovskites have the general formula AMX_3, where A and M are cations and X is an anion. The perovskite structure consists of a 3-dimensional corner-sharing MX_6 octahedral network with A cations in the cavities between the MX_6 octahedra (Fig.2.4.1). Cubic perovskite, which has no tilting between MX_6 octahedra and no distortion in each MX_6 octahedron, is regarded as the aristotype of perovskites.

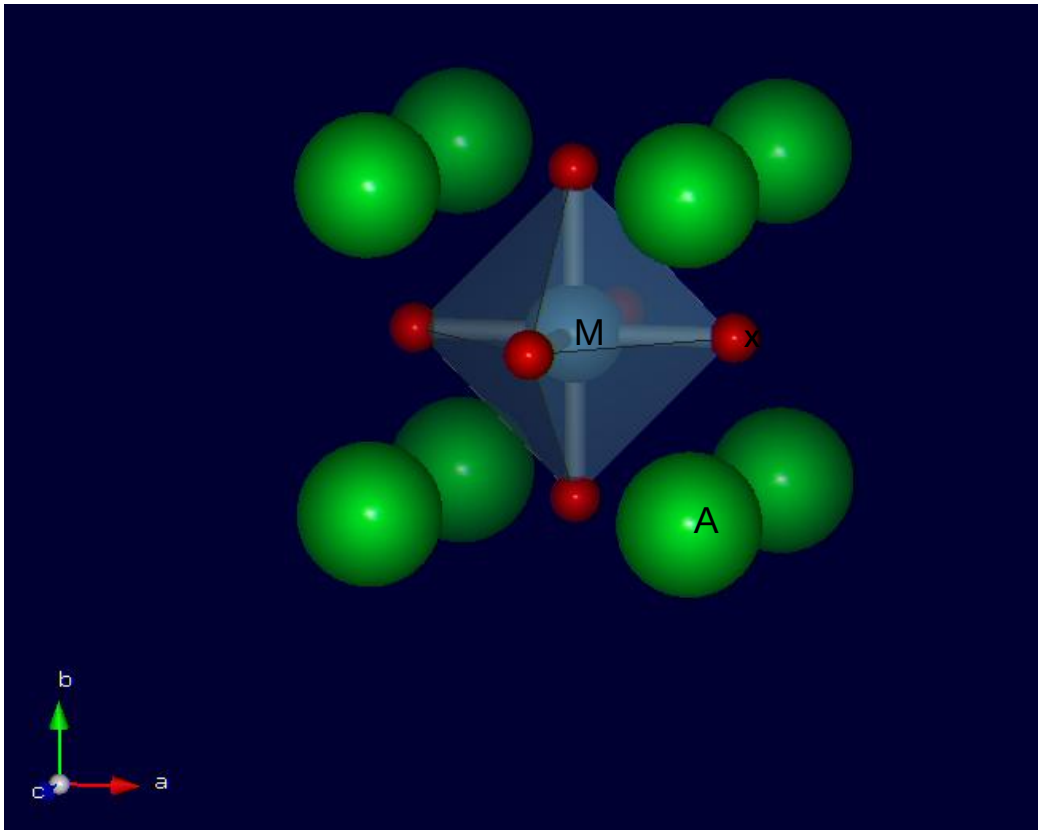

Fig.2.4.1 Crystal structure of prototype cubic perovskite AMX_3

Assuming the close packing of X anions, the lattice parameter *a* can be written as:

$a = 2r_M+2r_X$ (r_M: ionic radius of M cation, r_X: ionic radius of X anion)

If the A cation fits into a 12 coordinate site, the ionic radius of the A cation must satisfy the geometrical requirement:

$\sqrt{2}\, a = 2r_A+2r_X$ (r_A: ionic radius of A cation, r_X: ionic radius of X anion)

By combining these two equations, the relationship between ionic radius of the A cation, M cation and X anion is:

$$r_A+r_X = \sqrt{2}\,(r_M+r_X)$$

This equation is only satisfied in cubic perovskites, such as $SrTiO_3$ at room temperature. Factors such as octahedral tilting (such as in $CaTiO_3$), movement of the M cation off the centre of MX_6 octahedra (such as in $BaTiO_3$) and distortion of MX_6 octahedra (such as in $CaMnO_3$[64]) result in deviations from the equation written above.

When the M cation is a transition metal and X is oxygen, perovskites adopt a special electronic structure. This electronic structure is the origin of the interesting physical properties of perovskites. Transition metals have electrons in d orbitals. The

degree of the degeneracy of the d orbital in transition metals is 5. These d orbitals are split into t_{2g} orbitals and e_g orbitals. In the perovskite structure, the electron clouds of t_{2g} orbitals for the M cation point towards the cavity between O^{2-} ions, while the electron clouds of e_g orbitals extend in the direction of O^{2-} ions (Fig.2.4.2). This results in splitting of the energy state of the two sets of d orbitals in the perovskite structure. Electron clouds of e_g orbitals will be closer to O^{2-} ions and the orbital will have higher energy state than the t_{2g} orbital. This phenomenon is called crystal field splitting and the energy gap between e_g and t_{2g} orbitals is represented as 10Dq ($D = -\frac{35Ze}{4a^5}$, $q = \frac{2e}{105}\langle r^4 \rangle$, Z: valence, r: distance between the d-electron and the origin, a: distance between the oxygen and the origin). Crystal field splitting in perovskites is important because it can influence the electronic structure, the distortion of the octahedra and the conductivity of the compound. The Jahn-Teller effect which accompanies the distortion of octahedra arises from the crystal field splitting. If only one electron occupies the degenerated orbits, the total energy of the crystal field will reduce after the splitting of the orbitals. The crystal field prefers a lower energy state, so it will lead to the splitting of orbitals in such a case. However, if the splitting of the orbits happens, it will lower the symmetry of the perovskite structure due to distortion of the octahedra. This is called the Jahn-Teller effect and it is one of features which characterize the transition metal oxides.

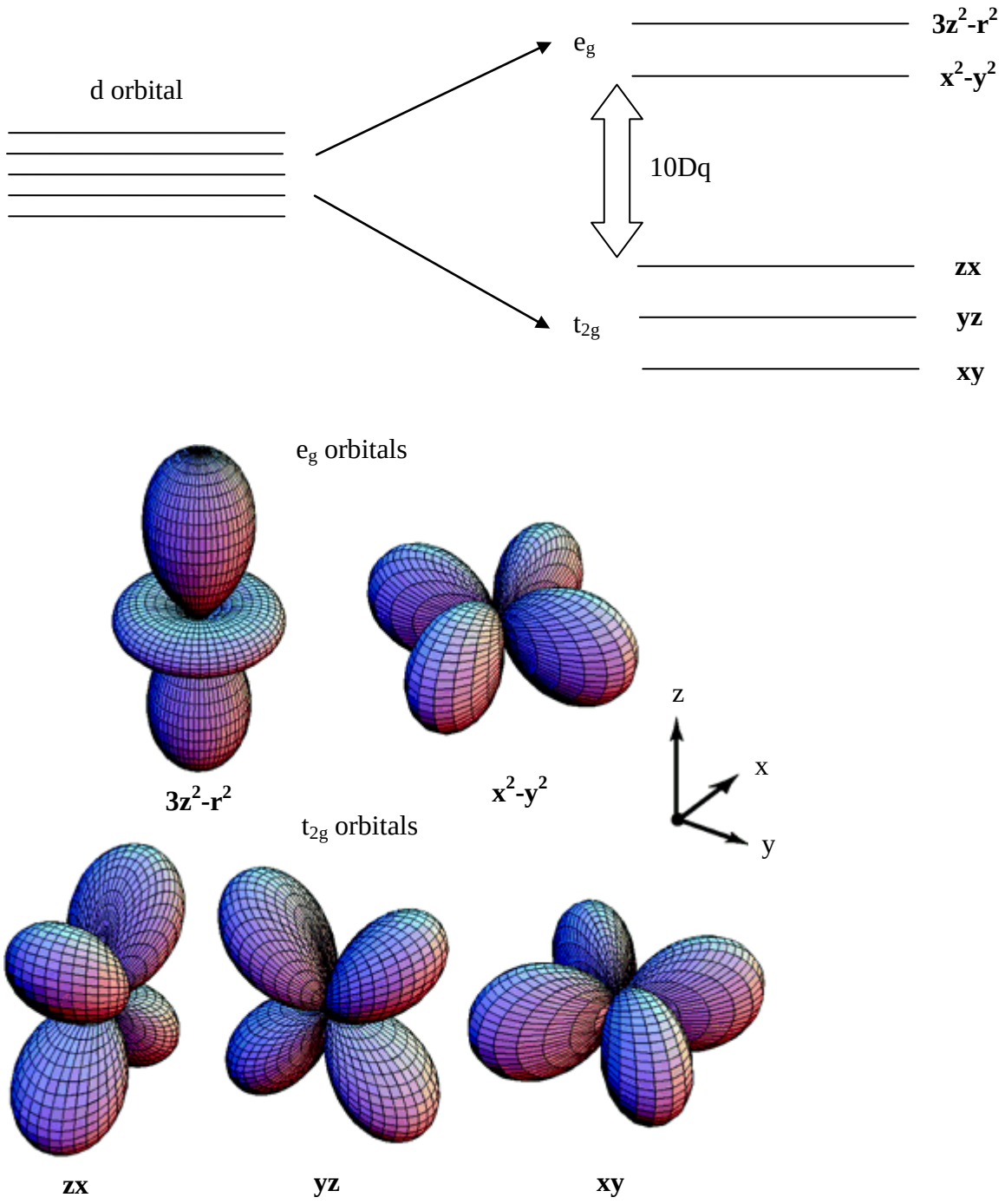

Fig.2.4.2 Crystal field splitting of degenerated d orbitals and their orbital orientation for transition metals in the perovskite structure

2.5 Octahedral tilting in perovskite

In an ideal cubic perovskite AMX_3 the coordination number of the A cation is 12. However, this ideal perovskite structure is distorted in many perovskites, especially in $A^{2+}B^{4+}O_3$ and $A^{3+}B^{3+}O_3$ perovskites, which are characterized as the $GdFeO_3$ group. In this group, distortion of the perovskite structure results in reduction of the coordination of the A cation from 12 to 8. Distortion of perovskite arises from tilting of the MO_6 octahedra in any of the three crystallographic directions relative to the ideal cubic perovskite structure, and results in a lowering of the symmetry. The tilting causes the M cation- X anion bond in one octahedron to rotate in an opposite direction to that in a neighboring octahedron. In this way, doubling of the repeat distances perpendicular to the tilt axis occurs. To maintain the M cation- X anion bond distance, the M cation- M cation distance has to become shorter, reducing the axial length of the structure. The pseudo-cubic sub-cell in Fig.2.5.1 is useful when describing the nature of octahedral titling in perovskites. If the tilt angles of the pseudo-cubic [100], [010] and [001] directions are written as alpha, beta, gamma, the new axial length for the distorted perovskite becomes:

$$a_p = a_0 \cos\beta \cos\gamma$$

$$b_p = a_0 \cos\gamma \cos\alpha$$

$$c_p = a_0 \cos\alpha \cos\beta$$

(a_p, b_p, c_p : pseudo-cubic sub-cell length, a_0: ideal perovskite cell length)

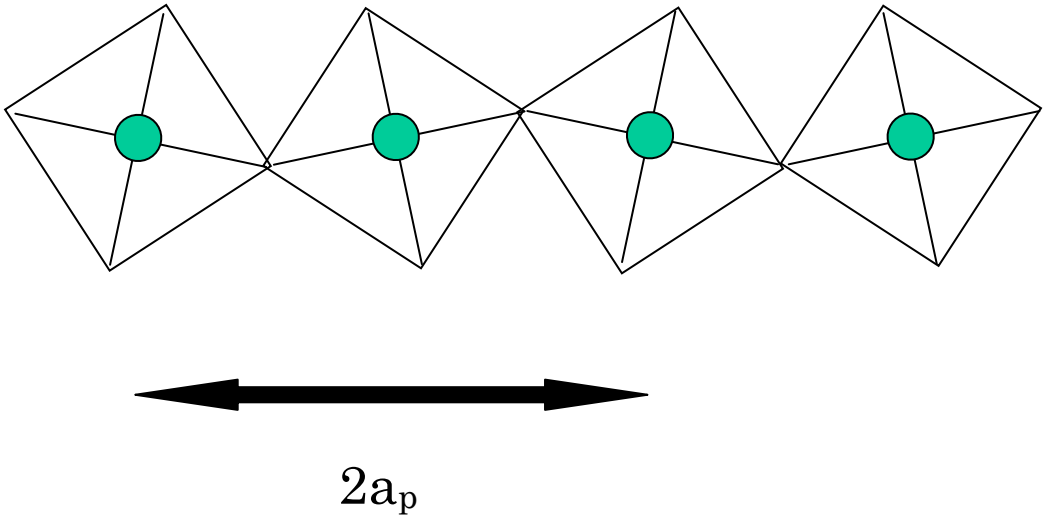

Fig.2.5.1 Demonstration of octahedral tilting with pseudo-cubic sub-cell

The pseudo-cubic sub-cell length is an indicator of the tilting system. If two of the sub-cell lengths are equal to each other, octahedra are equally tilted in two axes. When considering the behaviour of the tilting system, it is generally thought reasonable to ignore distortion of the MO_6 octahedra. Glazer et al.(1972)[42] introduced a notation to represent the tilt from the particular tilt axes using the equality of pseudo-cubic sub-cell length to characterize the system. For example, **aac** means equal tilts about [100] and [010], and **abc** means unequal tilts in three axes. The two types of tilt were also symbolized. If the octahedra along a tilt axis are tilted in-phase about the axis, superscript + is added to the symbol (Fig.2.5.2 (a)). If the octahedra along a tilt axis are tilted anti-phase about the axis, superscript- is added to the symbol (Fig.2.5.2(b)). If

there is no tilt in the axis, superscript 0 is added. For instance, the tilt system for $CaMnO_3$[64] will be represented as $\mathbf{a^+b^-b^-}$.

(a)In-phase octahedral tilting

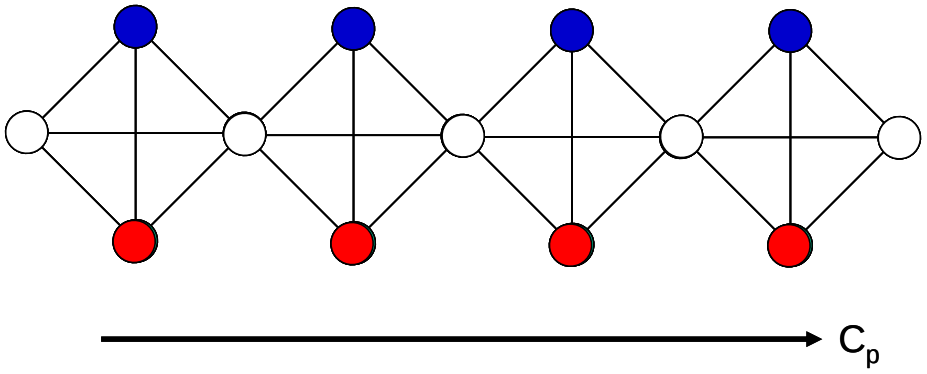

(b)Anti-phase octahedral tilting

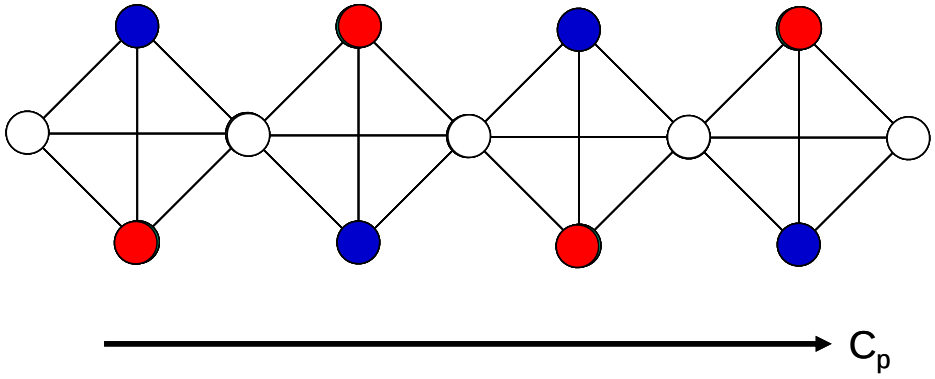

Fig.2.5.2 (a) In-phase ($\mathbf{c^+}$) and (b) anti-phase ($\mathbf{c^-}$) octahedral tilting about the pseudo-cubic *c* -axis representing the change of oxygen positions (○: on the paper, ●: above the paper, ●: below the paper)

This representation is very useful because the symbol can be used as a parameter of the tilting system. This representation can be used not only for perovskites but also for other structures containing an octahedral network. Any two + tilts or one + or – tilt out of three tilt axes mean that the relevant unit cell axes are normal to each other. Any two – tilts out of three tilt axes mean that the relevant cell axes are inclined to each other. In the $GdFeO_3$ group (such as $CaIrO_3$ perovskite[13] and $CaMnO_3$ [64]) cell axes are inclined towards each other. This structure group is a candidate for forming post-perovskite structure at high pressure, and some of them have already known to form a post-perovskite structure at high pressure due to the lower energy minima required for adopting post-perovskite structure compared to perovskite structure, which has been derived from first-principles calculation[6], [37]. The cell axes may have to be inclined to each other in perovskite in order to transform its structure into a post-perovskite at high pressure.

2.6 Rh_2O_3-structure

Tsuchiya et al.(2005)[43] and Oganov/Ono et al.(2005)[44] predicted that a phase transition from the Rh_2O_3 (II)-structure (Fig.2.4; Shannon et al., 1970)[45] to post-perovskite structure will take place in Al_2O_3 at P/T conditions above 150GPa on the basis of first-principles calculations. This theoretical prediction was proved experimentally by Oganov/Ono et al.[44]. Oganov/Ono et al.(2005)[44] heated the Al_2O_3 specimen at 200GPa up to 2500K using laser-heated diamond-anvil cell (DAC)

technique, and detected the diffraction peaks of a new post-perovskite phase using synchrotron X-ray diffraction. This post-perovskite phase remained stable even after being quenched to 163GPa, 300K. Al_2O_3 undergoes a phase transition from corundum to the Rh_2O_3 (II)-structure above 96 GPa[46],[47] in combination with high temperature above 1000 K. Thus, Rh_2O_3 (II)-structure is a direct polymorph of post-perovskite structure for Al_2O_3 and it gives us a new polymorph regime from perovskite-structure. In other words, Al_2O_3 transforms from Rh_2O_3 (II)-structure to post-perovskite structure without undergoing the transition to perovskite structure, unlike $MgSiO_3$. Rh_2O_3-structured Al_2O_3 can be described by two edges of each AlO_6 octahedron being shared with other AlO_6 octahedra, adopting the space group of *Pbcn* with 8 metal atoms and 12 oxygen atoms per unit cell (Fig.2.6). The unit cell of Rh_2O_3-structured Al_2O_3 is similar to that of an orthorhombic perovskite, while the structure is similar to that of corundum containing pairs of face sharing AlO_6 octahedra. What makes Rh_2O_3-structured Al_2O_3 different from corundum is that the AlO_6 octahedra are highly distorted, with interatomic bond distances ranging from 1.690 Å to 1.847 Å at 113 GPa (Lin et al., 2004)[47]. Fe_2O_3[7] is another example of an oxide which undergoes a phase transition from the Rh_2O_3 (II)-structure to post-perovskite structure. Shim et al.(2009)[7] experimentally observed the phase transition from the Rh_2O_3 (II)-structure (stable at 70GPa) to post-perovskite structure (stable at 73GPa) for Fe_2O_3 using a laser-heated DAC up to 73GPa, 2000K and synchrotron Mössbauer spectroscopy. As such, the Rh_2O_3 (II)-structure needs to be considered as a potential polytypes of post-perovskites when high pressure synthesis is applied for finding new post-perovskite compounds. There is no ABO_3-type oxide known to adopt Rh_2O_3 (II)-structure up to date, so it will be

challenging to directly synthesise the Rh_2O_3 (II)-structured compound from raw materials.

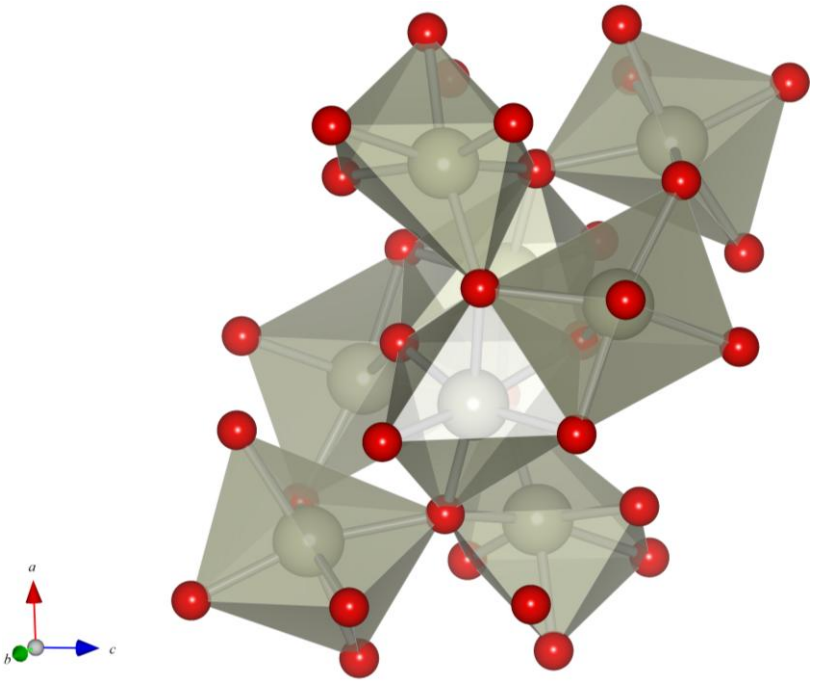

Fig.2.6 Crystal structure of Rh_2O_3(II)-structure: *Pbcn*, Z=4 (Al_2O_3 adopts this structure at high pressure/temperature conditions above 96 GPa/1000 K)[46], [47]

2.7 C-type rare earth oxide (R_2O_3) structure

Mn_2O_3 undergoes a phase transition from the initial C-type rare earth oxide-structure (Adachi et al., 1998)[48] to post-perovskite structure (Santilla ń et al., 2006) [8]. Santilla ń et al.(2006) heated Mn_2O_3 at 40.4GPa up to 1000K using laser-heated DAC (diamond-anvil cell) and detected the diffraction peaks of a new post-perovskite phase using synchrotron X-ray diffraction. This post-perovskite phase remained stable when quenched to 30GPa, 300K, but further decompression resulted in the initial phase of Mn_2O_3. In other words, Mn_2O_3 is not quenchable to ambient conditions, just like $MgSiO_3$ and Al_2O_3. Mn_2O_3 transforms directly to the post-perovskite structure without undergoing any other transition to perovskite or the Rh_2O_3 (II) - structure. Thus, C-type rare earth oxide- structures are another promising polymorph of the post-perovskite structure, and give us a new polytype series apart from perovskite and Rh_2O_3 (II) – structure. Fig.2.7 shows the crystal structure of C-type rare earth oxide adopting the cubic space group of *Ia*3. It contains 32 metal atoms and 48 oxygen atoms per unit cell, where every atom is in the 6 coordinated environment. Compared with the RO_2 (R: rare earth metal) fluorite- structure, one-fourth of the oxygen sites are vacant. C-type rare earth oxide structures are found as a stable phase at ambient conditions for oxides with a rare earth metal above Tb [47]. Such accessibility at ambient condition gives us opportunity for applying laser heated DAC techniques on rare earth oxides, such as Yb_2O_3. Meyer et al.(1995)[49] conducted high-pressure studies on Yb_2O_3 up to 20GPa without laser heating, and found a pressure induced transition from cubic to monoclinic structure at 13GPa. High pressure studies above 20GPa using laser-heated DAC

technique is expected to find a post-perovskite phase of Yb_2O_3 just like Mn_2O_3 or another polymorph of post-perovskite structure.

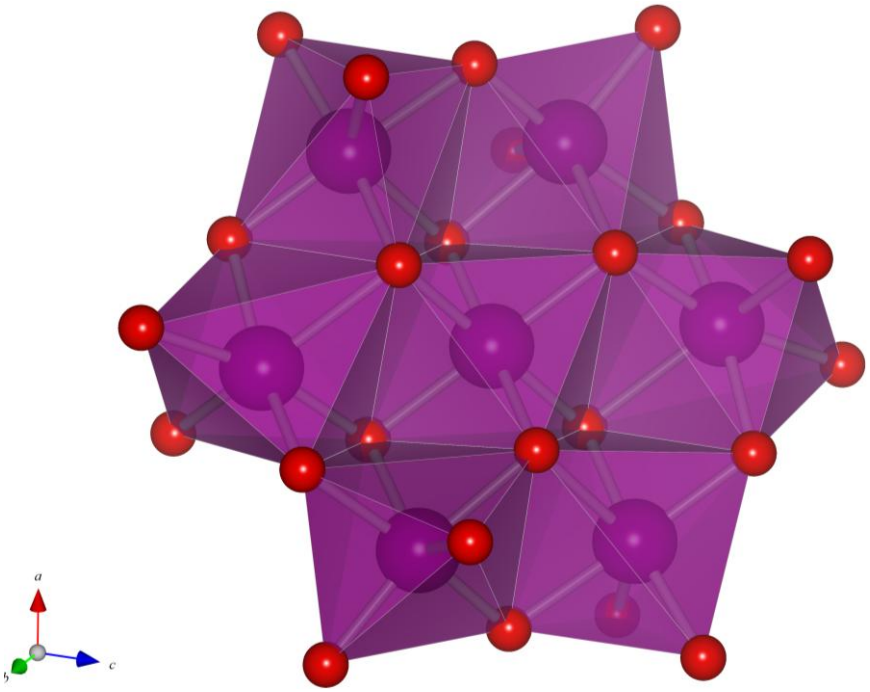

Fig.2.7 Crystal structure of C-type rare earth oxide structure: *Ia*3, Z = 16 (Mn_2O_3 initially adopts this structure at ambient conditions; Santilla ́n et al., 2006[8])

3. Experimental basics

3.1 Theory of X-ray diffraction

X-ray diffraction is a commonly used technique for revealing information on the crystallographic structure, chemical composition and physical properties of materials. Although yielding information on the atomic structure of materials, X-ray diffraction is based on the elastic scattering of X-rays from electron clouds of individual atoms in a sample.

In 1913, W.L.Bragg and W.H. Bragg determined the theory of interference of X-rays in crystalline lattices, commonly known as Bragg's law. The model can be derived from a simple lattice consisting of a periodically arranged set of atoms on an infinite set of planes separated by distance d (figure 3.1). When X-rays are scattered from the lattice, peaks in intensity are observed when X-rays scattering off planes at different depths in the lattice are in-phase. This occurs when the pathlength difference between X-rays is equal to an integer number of wavelengths. This is known as the Bragg equation, and can be expressed as:

$$2d\sin\theta = n\lambda \quad (n = 1,2,3,...)$$

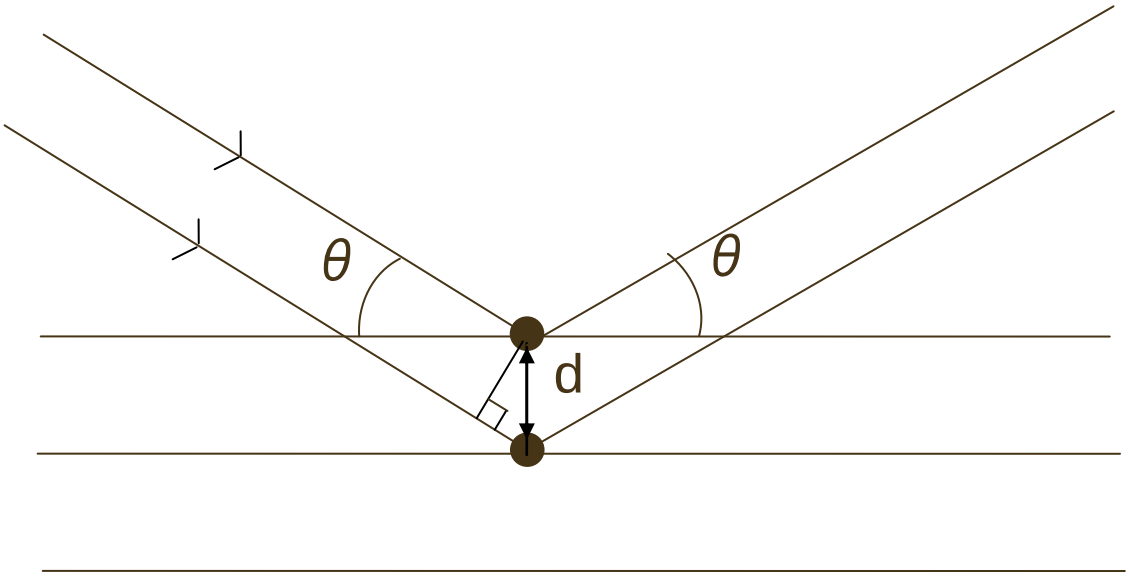

Fig.3.1 Image of Bragg reflection

Each of the Miller planes hkl has its specific inter-plane distance d, so the angle of X-ray diffraction differs from one to another. It is difficult to determine the absolute value of the intensity of X-ray diffraction, which depends on the size of the crystal. Instead, it is possible to calculate the ratio of the intensity of X-ray diffraction. The intensity of diffraction from each hkl plane depends on the structure factor, which is defined as below.

$$F(hkl) = \sum_j f_j \; T_j \exp\{2\pi i(hx_j + ky_j + lz_j)\}$$

(f_j: atomic scattering factor of atom j, T_j: function of thermal factor of atom j)

The atomic scattering factor f_j is a function of scattering angle. T_j is a function of thermal factor defined as below in the context of thermal vibration.

$$T_j = \exp\{-(h^2B_{11}+k^2B_{22}+l^2B_{33}+2klB_{23}+2lhB_{31}+2hkB_{12})\}$$

(B_{11}, B_{22}, B_{33}, B_{23}, B_{31}, B_{12} : anisotropic thermal parameters)

The structure factor can be synthesised from the continuous summation of the X-ray beams scattered by the electrons over the lattice volume. Therefore, the structure factor can also be written as a Fourier transform of the electron density.

$$F(\vec{K}) = \int \rho(\vec{r}) \exp\{2\pi i(\vec{K} \cdot \vec{r})\} dv$$

($\vec{K}$: scattering vector, $\rho(\vec{r})$: electron density at $\vec{r}$, v: lattice volume)

As the structure factor is nonzero only at the lattice points, the electron density at each lattice point (x, y, z) can be calculated from the structure factor as below.

$$\rho(xyz) = \frac{1}{V} \sum_h \sum_k \sum_l F(hkl) \exp\{-2\pi i(hx + ky + lz)\}$$

The intensity of X-ray diffraction is proportional to the square of the magnitude of the structure factor $F(hkl)$. One has to know the phase of the structure factor in order to calculate the electron density as shown above, while single crystal X-ray diffraction measurements only give the intensity data. In other words, the essential phase information of the structure factor is lost though the measurement. Therefore, the final

purpose of the structural refinement of X-ray diffraction data is to determine the electron density distribution from the measured $|F(hkl)|^2$. In the $CaIrO_3$ structural refinement by Hirai et al.(2007)[16], one of such methods to estimate the phase called Direct Method was used. In Direct Method, one assumes that all the electrons of the atom exist at the atomic nucleus so that one can recalculate and normalize the magnitude of the structure factor. In this way, the magnitude of the structure factor has a certain distribution which has a correlation with the phase of each reflection. In other words, direct method is used for estimating the phase introducing the normalized structure factor. Therefore, one can only obtain a partial structure from direct method with the estimated phase, which includes some probabilities. In order to obtain accurate atomic positions, the successive refinement of the atomic positions with the thermal parameters and difference Fourier synthesis has to follow after direct method. In difference Fourier synthesis, the difference between the estimated electron density of the partial structure and the electron density of the whole structure obtained using all the reflections is calculated. Difference Fourier synthesis is not only used for checking the accurate atomic positions, but also for finding the missing atoms of the structure.

In powdered samples, the grains have multiple orientations unlike the case for single crystals. Therefore, the reciprocal lattice points corresponding to the lattice planes (hkl) have multiple orientations as well. In other words, the groups of reciprocal lattice points form spheres with the radius of $1/d_{hkl}$. Reciprocal lattice points have to form an even sphere in order to obtain reasonable intensities in powder X-ray diffraction. In practice, one has to make sure that the number of grains is large enough and that the

grain size is small enough. If there is any preferred orientation for a certain lattice plane, one has to take this into consideration by running a texture analysis during the structural refinement. There is no infinite repetition of parallel lattice planes in powdered samples unlike single crystals (powdered samples are not mosaic crystals), so the intensity reduction of deeper lattice planes due to multiple scattering (secondary extinction) is negligible for powdered samples. Therefore, one does not have to make an extinction correction in powder diffraction refinement.

3.2 Scanning Electron Microscopy

In scanning electron microscopy, very fine beam of electrons with energies up to about 30kV is focused onto the surface of a specimen and rastered across it in parallel lines. A number of phenomena occur at the surface under electron impact. The most important thing for scanning microscopy is the emission of secondary electrons with energies of 20－30eV, and high energy backscattered electrons. Secondary electrons are emitted from the specimen due to the collision with the high energy incident beam. The backscattered electrons are electrons from the incident beam which have interacted with atoms in the specimen and reflected out again.

The intensity of both emissions is very sensitive to the angle at which the electron beam strikes the surface. The emitted electron current is collected and amplified and this signal is used to vary the brightness of the trace of a cathode ray tube being scanned in synchronism with electron probe. Therefore, the SEM image is a high magnification view of the specimen, analogous to that provided by a reflected light

microscope. Detectors which discriminate between different electron energies are available so that either a secondary electron or backscattered image can be produced. The intensity of emission of the back scattered electrons depends on the average of atomic number of the specimen, as well as surface topography. Heavy atoms produce many more backscattered electrons than light atoms. Therefore, the local variation in average atomic number results in variations in the contrast of the image.

An additional type of radiation resulting from interaction of the electron beam with the sample is emission of characteristic X-ray. An X-ray photon is produced when an outer shell electron in an atom falls to a lower energy inner shell to replace an ejected electron. X-rays produced in this manner have very specific energies, and spectra can be used to determine sample composition. In Energy Dispersive Spectroscopy (EDS or EDX) a solid state detector, cooled with liquid N_2, is used to detect characteristic X-rays. Spectra can be used to give semi-quantitative information on sample composition, or with adequate standards, qualitative analysis (with an accuracy of 0.1 element %) of elemental composition from areas down to 1 μm^3.

3.3 Electron Probe Microanalysis

Electron Probe Microanalysis (EPMA) is performed using an electron microscope specifically designed for X-ray microanalysis. EPMA differs from most other techniques used to analyze materials because it involves the excitation and chemical analysis of selected volumes with diameter and depth in the order of a few microns near the surface. The electron beam, usually in the range of 1 to 30 keV, is

focused on the surface of the sample. For accurate analysis, the sample surface has to be as flat as possible. Characteristic X-rays will be produced within the excited volume by collisions between the primary electrons and the atoms of the sample causing the ionization of orbital electrons. If an inner orbital electron is ionized, the unstable excited atom rapidly achieves its ground state again by emitting characteristic X-rays and Auger electrons. The energy of the characteristic X-ray is element-dependent since its wavelength is directly related to the atomic number of the excited atom. The intensity of characteristic X-rays will be measured using wavelength dispersive (WDX) or/and energy dispersive (EDX) spectrometers. Using an EDX system it is possible to measure all X-ray lines simultaneously during a short time, but the energy resolution will be rather poor, about 130-150 eV. On the other hand, using a WDX spectrometer one can get an excellent energy resolution of 10-15 eV, but the measuring time will be much longer since the X-ray lines have to be measured sequentially. Compared with scanning electron microscope, the main difference is the additional function of WDX X-ray analysis. WDX spectrometer focuses the X-rays from the sample onto the slit of a detector, using a curved analysing crystal, which diffracts the X-rays on the basis of the Bragg equation. The wavelength that is diffracted is adjusted by a mechanical movement of the analysing crystal and the detector. Thus, only a single wavelength can be detected at an instant and slow scanning of the spectrometer is required for obtaining the full spectrum of the sample. EPMA uses quantitative analysis in order to determine the chemical composition of the sample. Regarding the resolution of EPMA, the detection limit for trace elements in the sample is approximately 0.1 weight %. The characteristic

X-ray count rate of the sample is compared to that of a compound with a known chemical composition, which is used as a standard for the analysis. Such comparison against the standard is made taking the sample dependent effects into account, known as ZAF correction. Z is a parameter that stands for atomic number correction, A stands for absorption dependent correction (coming from the unique sample topology, such as the size and shape of excitation volume) and F stands for second fluorescence correction. If one assumes the count rate of the sample is I_s and the count rate of the standard is I_0, ZAF correction term: k_s can be described by the following relationship.

$k_s = ZAF\ I_s/I_0$

The chemical composition of the sample is determined by multiplying the ZAF correction term by the chemical formula of the standard. In this study, $CaIrO_3$ perovskite was used as a standard for determining the chemical composition of $CaIrO_3$ post-perovskite, while $CaIrO_3$ post-perovskite was used as a standard for determining the chemical composition of $CaIr_{1-x}Pt_xO_3$ solid solutions. As such, EPMA is suitable for obtaining detailed information about the local chemical composition of a sample in accordance with its topology.

3.4 Laser-heated diamond anvil cell technique

(1) Diamond anvil cell (DAC)

The diamond anvil cell is a reliable tool for generating high static pressures by compressing a sample chamber between opposing brilliant cut diamond culets. The extreme hardness of the diamond along with its excellent transmittance to almost the

entire electromagnetic spectrum enables a wide range of *in-situ* studies (high pressure Raman spectroscopy, high pressure X-ray diffraction etc.) on pressure-induced phenomena of the specimen. Hydrostatic (as opposed to simple uniaxial) compression of a sample is possible if an appropriate gasket and, most importantly, appropriate pressure medium are used. Firstly, a rhenium gasket is placed between the diamond culets and a small force applied to indent or prepress the gasket. A small hole is then drilled in the centre of the gasket so that it can act as a sample chamber. The sample and pressure medium are placed into this hole. The purpose of inserting the pressure medium is to evenly distribute the pressure within the sample chamber, which enables the sample chamber to maintain a homogeneous hydrostatic pressure at high pressures. Thus, the pressure medium should minimize the pressure gradient in the sample chamber and should not react with the sample under any condition. In practice, different pressure media are used to ensure hydrostatic conditions under different pressure-temperature conditions. Argon and NaCl are commonly used pressure media which satisfy such requirements. For pressure calibration, a small ruby chip can be placed into the sample chamber as well, although the diamond itself can be used as a pressure marker by measuring the pressure-dependent phonon mode frequency using Raman spectroscopy (Akahama et al., 2004)[50].

(2) Laser heating of DAC

The laser-heated diamond anvil cell is the only tool which is able to heat the sample simultaneously to high temperatures over 7000K (Subramanian et al., 2006)[51] at

pressures up to many megabars, thereby enabling experimental simulation of high P/T conditions of planetary interiors. As such, laser heating DAC have had a major impact in high pressure mineralogy and solid state synthesis. The first paper on laser heating using a YAG laser was published by Ming et al.(1974)[52]. Laser heating is based on absorption of infrared radiation by the sample after the beam transmits through the diamond anvils with minor energy loss. The biggest advantage of laser heating DAC technique is that no change of cell assembly is required, since the diamond already has amenability and the pressure medium is contamination-free. However, it is essential to heat the sample for long enough to attain the desired temperature (e.g. long enough to induce a particular phase transition or reaction) but not so long as to melt the sample or the diamond culet.

3.5 Raman scattering

When monochromatic radiation of wavenumber ν_0 is incident on a specimen, most of it is transmitted. However, some portion of radiation will be scattered by the specimen. The scattered light will include not only radiation with the wavenumber: ν_0, but also radiation with pairs of new wavenumbers: $\nu_0 - \nu_M$, $\nu_0 + \nu_M$. Scattered radiation with no change in wavenumber is known as Rayleigh scattering. Scattered radiation with wavenumber: $\nu_0 - \nu_M$ is called Stokes scattering and the radiation with wavenumber: $\nu_0 + \nu_M$ is called anti-Stokes scattering. Such scattering with change of wavenumber is called Raman scattering (Raman et al., 1928)[53].

Stokes and anti-Stokes scattering form Raman bands in the spectrum of the scattered radiation and the wavenumber shift: ν_M stands for the wavenumbers of

molecular vibrations or lattice vibrations, and the energy associated with ν_M directly leads to transitions between energy levels (Fig.3.5) which are characteristic of each specimen. In other words, Raman scattering gives information about the phonon modes in the specimen. However, Raman scattering does not cover all the phonon modes of the specimen. There is a restriction that Raman-active phonons have to accompany the change of polarizability. Therefore, by quantitative analysis of Raman bands, Raman scattering can be used to identify molecular symmetry, thermodynamics and physical properties of the specimen. In order to obtain the Raman-active phonon modes of the specimen, measurements on Stokes scattering with a stronger intensity is merely required, and in most of the literature, Raman spectra is equivalent to Stokes scattering. However, comparing the phonon mode frequency and intensity ratio of Stokes scattering with those of anti-Stokes scattering is useful when one has to estimate the heating of the sample due to the incident laser during the measurement.

Observed intensities of Raman bands vary not only with crystal structure but also with the orientation of the specimen in respect to the polarized incident leaser beam. By changing the orientation of the specimen, the intensities and the number of observed Raman bands will vary. However, the position of the crystal where the incident light goes through must be fixed, or the orientation or the structure of the crystal under different conditions cannot be compared accurately. The detection of phase transitions of the crystals is also an effective use of Raman scattering. When a crystal goes through a structural phase transition the wavenumbers of Raman bands may change. Therefore, low-temperature and high-temperature Raman measurements can be performed to look

for structural phase transitions in crystals.

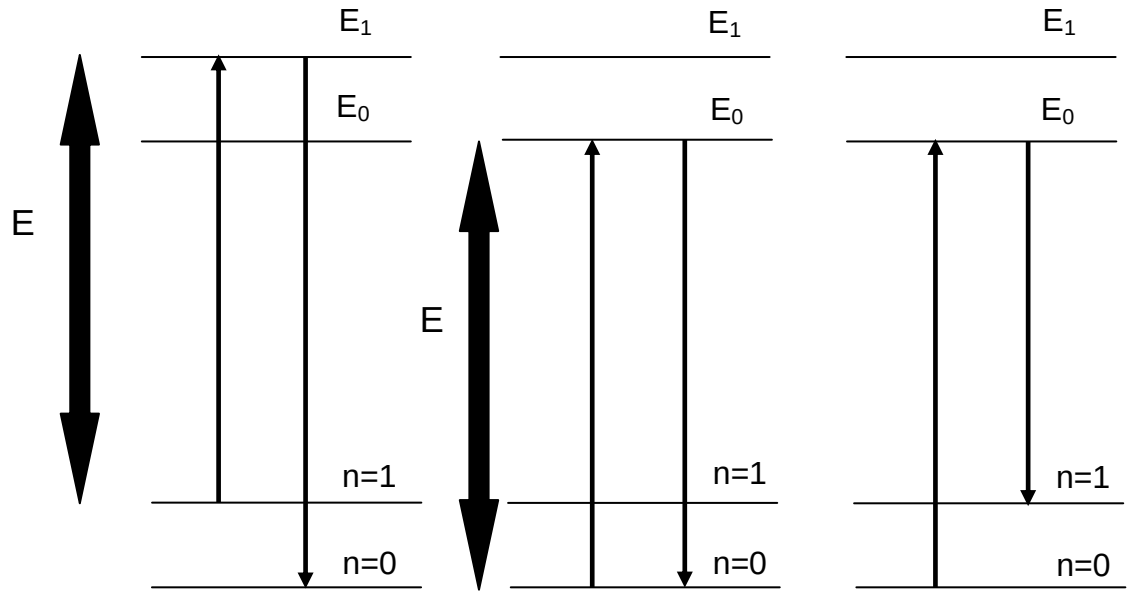

Fig.3.5 Transitions between energy levels during elastic and inelastic scattering

3.6 Multi-anvil cell and piston-cylinder apparatus

High pressure/temperature (P/T) solid state reaction is a useful tool to overcome the energy barriers for formation of materials and in finding new stable phases which are not accessible at ambient or at modest pressures. DAC (diamond anvil cell), multi-anvil cell and piston cylinder are the commonly used apparatus for such high P/T solid state reaction. If one wants to not only synthesise the material but also study further its detailed structural and physical properties, a large cell volume which can

accommodate a large amount of sample is required. Multi-anvil cell and piston cylinder apparatus can accommodate samples over 100mg, while DAC can only accommodate 0.1mg or less.

There are two types of multi-anvil cell configurations which are used to achieve high pressures above 10GPa yet realizing large cell volume. One is the so called 6-8 system developed by Kawai et al.(1970)[54], and the other is the 8-6 system which has cubic geometry (often referred as DIA geometry). 6-8 Kawai-type apparatus was used for this study, In the 6-8 system, a nest of 8 tungsten carbide anvils sits within a cube shaped cavity surrounded by 6 tool steel wedges (Fig.3.6.1). Each carbide cube has a truncated corner positioned towards the centre of the apparatus, thereby accommodating an octahedral sample assembly (Fig.3.6.2). The sample, a thermal insulator (ZrO_2), and furnace (graphite, $LaCrO_3$ or SiC) are accommodated inside the MgO octahedron cell that is placed in the nest of cubes, so that the octahedron can be pressed from all 8 sides by the anvils (for detailed cell assembly used in this study, see Chapter 4). Such geometry is highly stable and capable of sustained pressures and temperatures up to 28GPa and 2000°C. Gasketing is important to achieve the high pressure stability. In order to maintain equal pressurisation over the surfaces of carbide cubes and MgO octahedron cell, pyrophyllite gasket seals (disks) with uniform thickness are used to maintain equal distance between anvil faces. Gasketing not only has the effect of uniform pressurisation, but also the effect of protecting the tungsten carbide (especially the 8 carbide anvils) from the concentrated applied force on the truncations. The pressure capability of a multi-anvil cell apparatus depends on the truncation size of the

carbide. The smaller the truncation is, the higher the maximum achievable pressure is. Theoretically, the attainable pressure is equal to the ram force divided by the area of 4 truncations, so the maximum attainable pressure in a 6-8 system is $P = F/\sqrt{3}\,t$, where the truncation edge length of the carbide and ram force is denoted t and F, respectively. In practice, the experimental attainable pressure is more than 50 % lower than the theoretical value because of the gasketing on both 8 carbide anvils and the guide block. 8 carbide anvils were held together by glue on 6 plates of fiber-reinforced plastic which cover the entire surface of the anvils. A MgO octahedron with edge length of 14 mm, 8 carbide anvils with truncation edge length of 8 mm and 12 gaskets with the thickness of 2.83(3) mm were used in this study for generating desirable pressures over the sample accommodated in a gold capsule with a diameter of 2.5 mm and a height of 4 mm. The generated pressure was calibrated using the relationship between generated pressure and applied press load, which was determined by the fixed pressure point that bismuth undergoes phase transition, which is 2.55 GPa for Bi(I) to Bi(II) and 7.7 GPa for Bi(III) to Bi(IV) (Venkateswaran et al., 1997[55]). In order to detect these pressure-induced phase transitions, the electrical resistance of a thin strip of bismuth wire, which was attached to the top and bottom of the anvils, was measured at room temperature. The sample in the gold capsule was heated to high temperatures by the graphite tube, a pair of molybdenum rods and molybdenum disks accommodated in the MgO octahedron. The graphite tube plays a role as a heater, while a pair of molybdenum rods and disks (they sit at the top and bottom of the MgO octahedron) sandwich the graphite tube so that electron current can pass through the heater. In order to smoothly pass external

current to the cell, two Cu (copper) disks were inserted in to the opening cut made on the fiber-reinforced plastic plates so that they can touch the outer face of the two anvils touching molybdenum rods and the polished face of the steel wedge. In order to reduce heat loss by radiation, cobalt-doped MgO octahedron was used in this study. In order to avoid contamination of the sample, the gold capsule is separated from the graphite heater by a MgO sleeve. ZrO_2 disks surround the molybdenum rods and sandwich the molybdenum disks so that the graphite heater can be thermally insulated. Samples in this study were heated at the rate of 50 K per minute, annealed for 40 minutes at high temperatures achieved by the graphite heater and then quenched to room temperature. Temperature calibration from a previous user of the press was used. His calibration is based on the power-temperature relationship (temperature uncertainties are below 20K) determined by the quenched standard compounds (in the capsule) annealed for 60 minutes at a series of pressure/temperature boundary points that Fe_2SiO_4 glass and (Mg, Fe)SiO_4 glass undergo α- to γ- phase transition (Yagi et al., 1987[56]; Frost et al., 2003[57]).

The piston cylinder is a large-volume, high-pressure apparatus that can be used to routinely generate pressures of 2 to 5 GPa for sample volumes up to 750 mm^3, with simultaneous temperatures up to 1800 ℃. High pressures in this study were generated over the sample accommodated in a welded AgPd (silver palladium) capsule with a diameter of 3mm and a height of 5mm, using a piston-cylinder device converting a small load on a large piston to a large load on a small piston (Fig.3.6.3). AgPd capsule was chosen since it is chemically inert against the compounds of interest in this study. The

small carbide piston is forced into a pressure vessel, known as a bomb, which consists of a carbide core with central hole surrounded by steel support rings. Movement of the piston into the core compresses the sample volume. The sample assembly consists of a soft, deformable pressure medium (talc, NaCl, $BaCO_3$ etc) which is able to convert uniaxial compression into a hydrostatic sample pressure. An internal graphite furnace sits inside the pressure medium. Simultaneous high temperatures can be achieved by passing a large voltage across this internal resistance furnace. There is a Pyrex cylinder between the pressure medium and the heater, which acts as an electrical insulator as well as a trap for water. The AgPd capsule is located in the centre of the sample assembly, surrounded and held in place by machineable ceramics (Fig.3.6.4). Space above and below the capsule was filled with plugs of Al_2O_3 (Fig.3.6.4). The upper plug has a small central hole drilled for the R-type thermocouple. Pb (lead) foil was wrapped around the cell so that it can act as a lubricant at elevated pressure and temperature, and to aid removal of the sample assembly from the bomb after the experiment. The entire assembly is placed into the tungsten carbide core and then an insulated steel plug is placed on top. This plug completes the heating circuit, and once the pressure is applied, clamps the thermocouple in place preventing it from extruding upward. The piston-cylinder apparatus is made up of a frame and two hydraulic rams. The frame usually consists of three or four supporting posts. Pressure is first applied to the whole stack to compress and stabilize the pressure before load is applied to the sample via the piston. Such designs are described as end-loaded. Samples in this study were heated at the rate of 40 K per minute up to desirable temperatures using the empirical power-temperature relationship, annealed for

40 minutes and then quenched to room temperature. Pressure calibration was conducted using the known melting curve of NaCl. Temperature calibration was done by calibrating a R-type thermocouple wire against the melting curve of NaCl. However, even after such temperature calibration, the thermal gradient within the sample space of 5 mm height must be taken into account. Thermal gradient in the sample was determined to be less than 50 K by using two thermocouples.

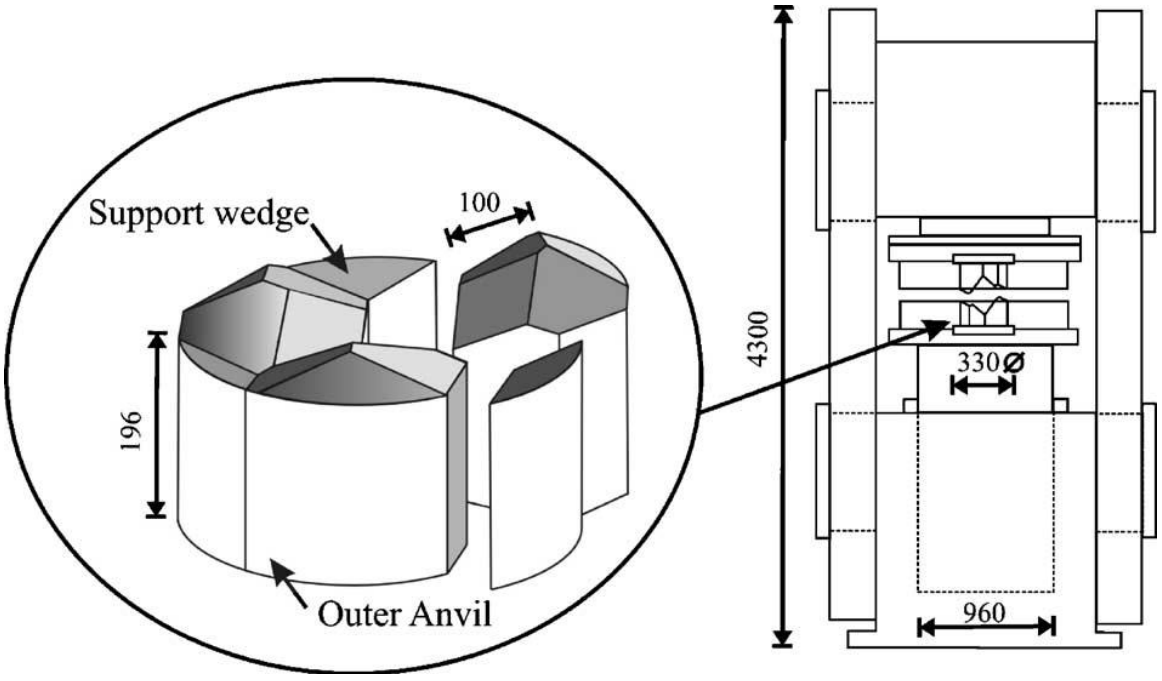

Fig.3.6.1 Schematic diagram of the six steel wedges of the guide block for the multi-anvil cell apparatus used in this study: Kawai-type 2000 tonne split-sphere press (SUMITOMO Inc.) operated in hydraulic ram at Geodynamics Research Center, Ehime University (the units are in mm)

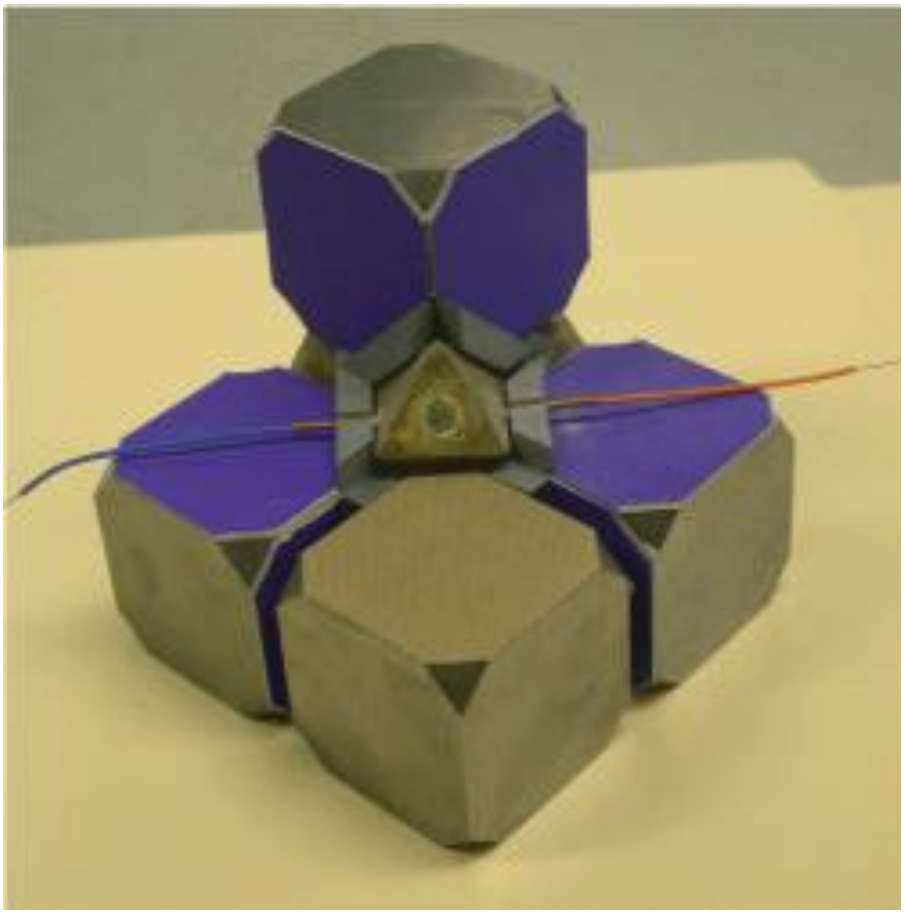

Fig.3.6.2 Photograph of multi-anvil cell used in this study; MgO octahedron (edge length: 14 mm) is sitting in the centre of the cell surrounded by 12 pyrophyllite gaskets (thickness: 2.8 mm) aligned with the truncated corner (triangle edge length: 8 mm) of 4 WC (tungsten carbide) anvils (denoted in blue) out of 8 WC anvils (edge length: 32 mm)

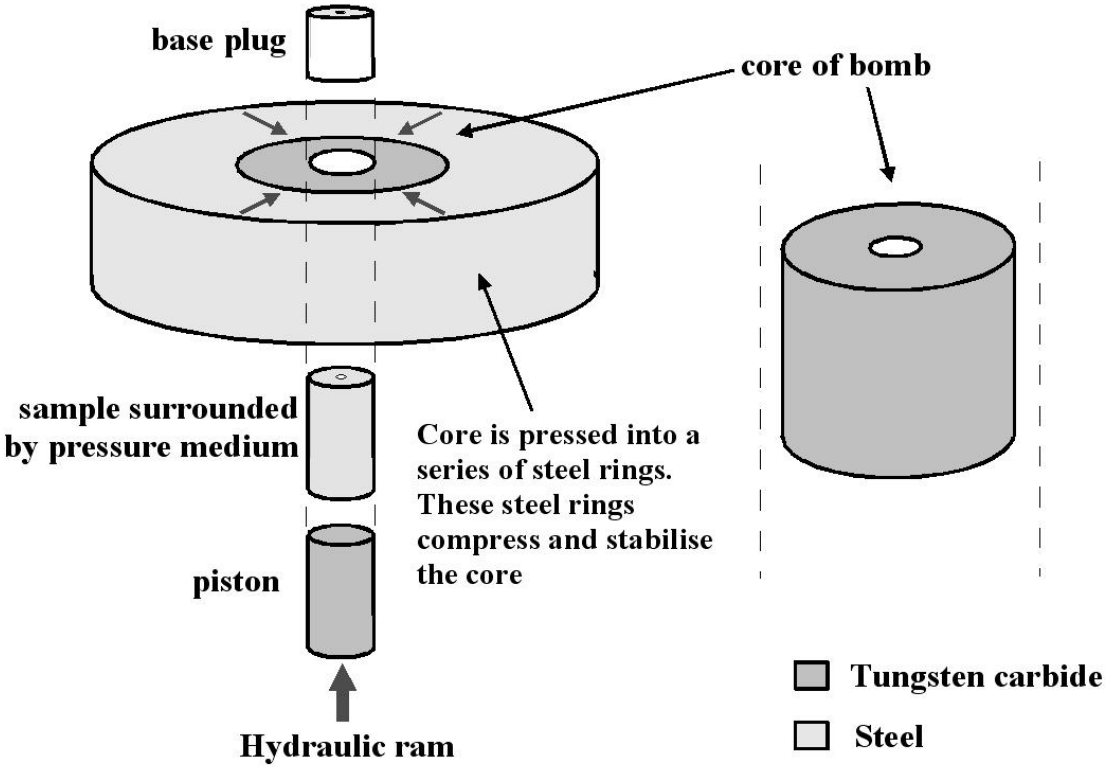

Fig.3.6.3 Schematic diagram describing the set up of piston-cylinder

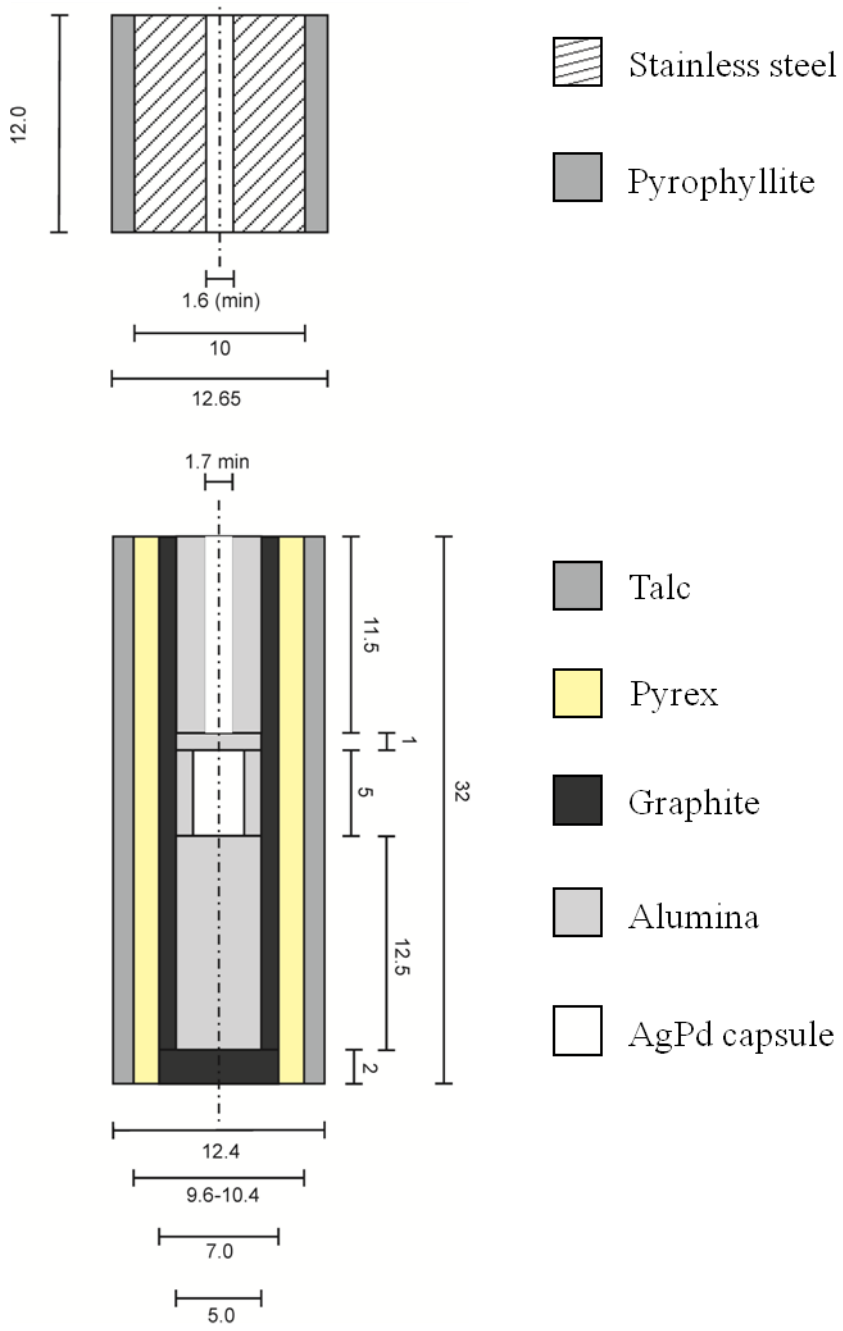

Fig.3.6.4 Cross section of the piston-cylinder sample assembly (all units are in mm), composed of base plug (stainless steel/pyrophyllite) and Talc-Pyrex Assembly

3.7 SQUID magnetometer measurement

A magnetometer is an instrument used to measure magnetic fields. SQUID magnetometers are very sensitive vector magnetometers, and are used to measure extremely small magnetic fields in samples. A Superconducting Quantum Interference Device (SQUID) (Fig.3.7) consists of a loop of superconductor with one or more Josephson junctions, known as 'weak links'. The superconductor used for SQUID is usually an alloy of gold, indium and lead or pure niobium. It can measure magnetic fields with resolutions up to 10^{-15} T or greater. In superconductors, current is carried by pairs of electrons known as Cooper Pairs which create an electron-pair wave. If two superconducting regions are positioned close enough, electron-pairs can tunnel across the gap and the two electron-pair waves will be coupled. Such tunnelling is called Josephson tunnelling, and carry a superconducting current as predicted by Josephson et al.(1962)[58] and confirmed experimentally by Anderson et al.(1963)[59]. The junction between the two superconductors is called the Josephson junction. The magnetic field caused by the sample induces a current around the superconducting loop. This alters the original current flowing through the superconducting loop. Hence, the potential difference across the loop can be measured and converted into the magnetic property measurements of the sample (Fig.3.7). The helium regulating valve in Fig.3.7 achieves continuous helium gas flow and the thermal shield blocks the external heat, hence a stable series of low temperature (cryogenic temperature) magnetisation measurements can be conducted.

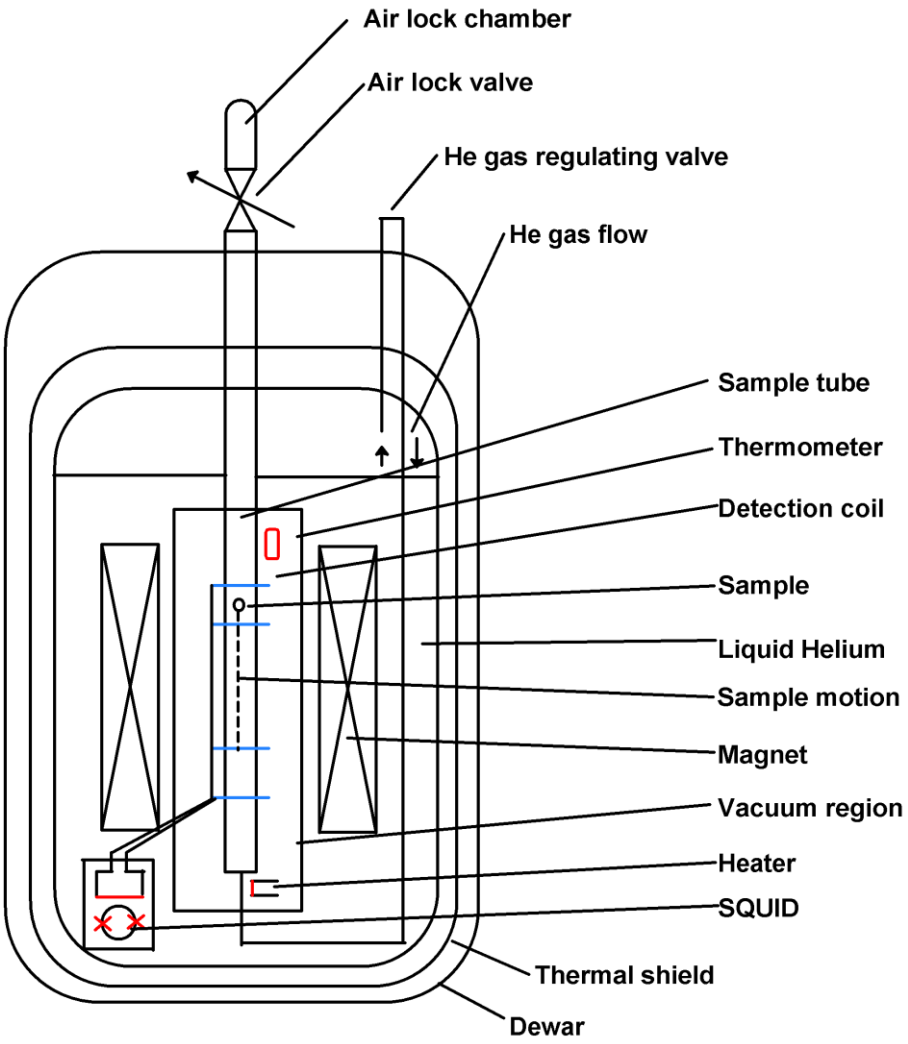

Fig.3.7 The schematic diagram of Superconducting Quantum Interference Device (SQUID)

3.8 Closed Cycle Refrigerator (CCR)

The closed cycle refrigerator (CCR) (Fig.3.8) is commonly used for low temperature measurements of properties such as electrical resistivity or heat capacity measurements down to 5K. It is composed of expander, compressor, vacuum shroud, and radiation shield. The refrigeration cycle takes place in the expander. The expander is connected to a compressor by two gas lines and an electrical power cable. One of the gas lines supplies high pressure helium gas to the expander, the other gas line returns low pressure helium gas from the expander. The compressor provides the adequate helium gas flow rate at the high and low pressure for the expander to convert into sufficient refrigeration capacity. The vacuum shroud surrounds the cold end of the expander in vacuum limiting the excessive heat on the expander. The radiation shield is actively cooled by the first stage of the expander and insulates the second stage from the room temperature heat.

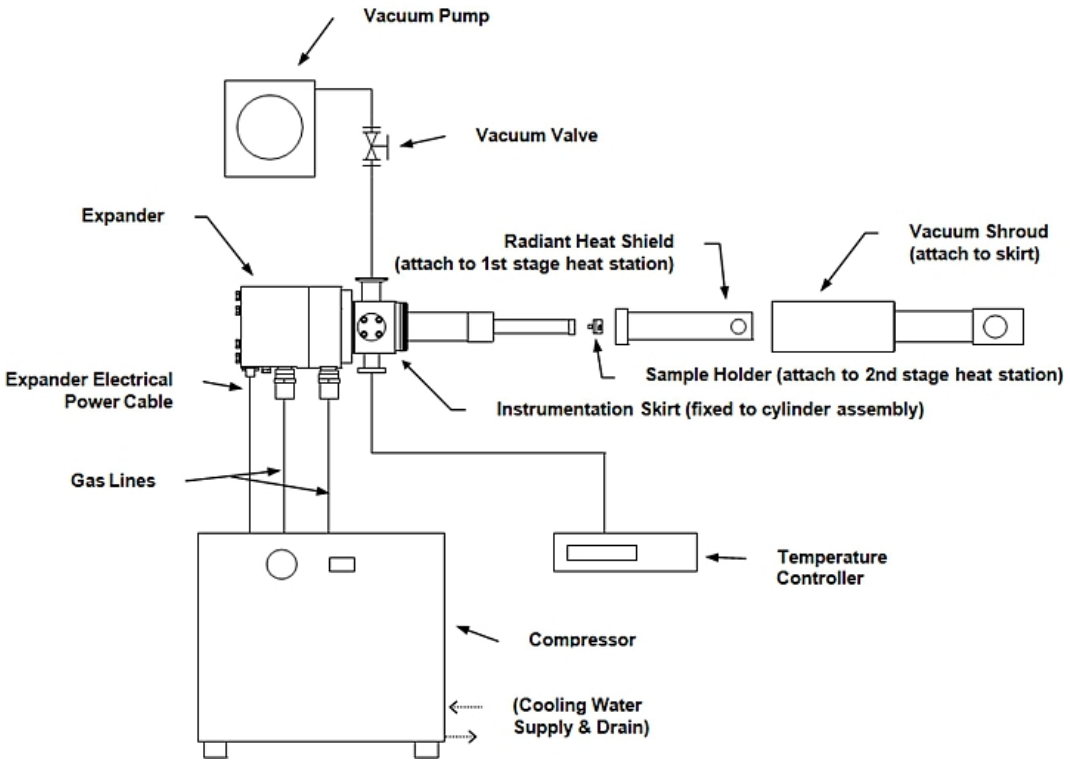

Fig.3.8 Schematic diagram of Closed Cycle Refrigerator (CCR) in courtesy of Advanced Research Systems, Inc.

4. Synthesis of $CaIr_{1-x}Pt_xO_3$ and *in-situ* high pressure Raman studies on $CaIr_{0.5}Pt_{0.5}O_3$: phase transition from post-perovskite to perovskite phase

4.1 Synthesis of $CaIr_{1-x}Pt_xO_3$

The flux single crystal growth method of Rodi et al.(1965)[12] was used for the synthesis of $CaIrO_3$ single crystals at School of Chemistry, University of Edinburgh. $CaCO_3$ powder was dried at 120°C to release any absorbed water and then mixed with the ratio of 1:10:1 for $CaCO_3/CaCl_2$ /IrO_2, where $CaCl_2$ acts only as a flux. The starting mix was then put in an alumina crucible, placed into a furnace and slowly heated to 950°C over 3 hours to ensure slow decarbonation. The furnace was kept at 950°C for 20 hours, and then slowly cooled to 750°C over 48 hours. After the temperature reached 750°C, power to the furnace was shut off, and the furnace allowed to cool down to room temperature. The crucible was taken out from the furnace, and water was added in order to separate the sample from the crucible without breaking crystal grains. The sample was recovered as a black solution, which turned out to be a mixture of $CaIrO_3$ and $CaCl_2$. Sufficient water was added to the sample to completely dissolve the $CaCl_2$. The resulting solution was then passed through filter paper. In this way, $CaIrO_3$ was left on the paper and $CaCl_2$ was eliminated from the sample. The sample left on the paper was filtered repeatedly. Optical examination of the recovered $CaIrO_3$ by SEM revealed that the sample consisted of tiny black needles of $CaIrO_3$ and only a tiny amount of flux stuck to the needles. Raman spectroscopy was used to verify that all crystals were $CaIrO_3$ using

data on $CaIrO_3$ Raman-active modes by Hirose et al. (2005) [32]. No additional phases were noted during this examination.

Two fine grained polycrystalline samples of $CaIrO_3$ were synthesised at ambient pressure (at School of Chemistry, University of Edinburgh) and at high pressures using a piston-cylinder (at School of Geosciences, University of Edinburgh). One sample was synthesised at ambient pressure by heating a stoichiometric mixture of CaO and IrO_2 in a silica tube evacuated to 4 $x10^{-2}$ Pa and annealed in air at 1000 ℃ for 20 hrs, while the other sample was synthesised at a high P/T condition (P: 2 GPa, T: 1100 ℃) in a AgPd capsule by a piston-cylinder apparatus. Both samples were quenched rapidly to ambient temperature before recovering.

A polycrystalline sample of $CaIrO_3$ perovskite was synthesised by heating a stoichiometric mixture of CaO and IrO_2 in a silica tube evacuated to 4 $x10^{-2}$ Pa and annealed in air at 930 ℃ over 20 hrs. The silica tube pressure was set to a higher value than the case of synthesising the post-perovskite phase since the perovskite phase is metastable (Sarkozy et al., 1974) [13] without the help of high-pressure (Hirose et al., 2005) [32] and does not favour reducing conditions.

Polycrystalline samples of $CaIr_{1-x}Pt_xO_3$ were synthesized at high pressure/temperature conditions. $CaIr_{1-x}Pt_xO_3$ (x = 0.3, 0.5, 0.7) solid solutions were synthesized at Geodynamics Research Center, Ehime University by high P/T solid-state reaction of CaO, IrO_2, and PtO_2 powders using a multi-anvil apparatus. CaO powder was prepared from $CaCO_3$ by heating in air at 1000 ℃ for 24 hrs. Well-ground mixtures of the starting material at stoichiometric molar ratios were placed into a gold capsule (ϕ=2.5 mm) sandwiched by BN (boron nitride) composite disks (ϕ=2.7 mm), which

creates reducing conditions and prevents loss of volatiles such as PtO_2. Fig.4.1 shows the cell assembly for the synthesis of $CaIr_{1-x}Pt_xO_3$ (x = 0.3, 0.5, 0.7). Cobalt doped MgO octahedron was used as the pressure medium cell, which was sintered at 800 ℃ (for 5hrs) in advance. The cells were then pressurised to 15 GPa and heated. Samples were annealed at 1300 ℃ for 40 min, followed by rapid quenching to ambient temperature, and finally the release of pressure. Samples were recovered as dense, dark black pellets. A pressure of 15GPa was used to ensure complete reaction of the starting material and formation of homogenous solid solutions. Previous attempts to synthesise solid solutions using a piston-cylinder apparatus at 3 GPa gave samples with a range of Ir/Pt ratios containing IrO_2 and Pt secondary phases.

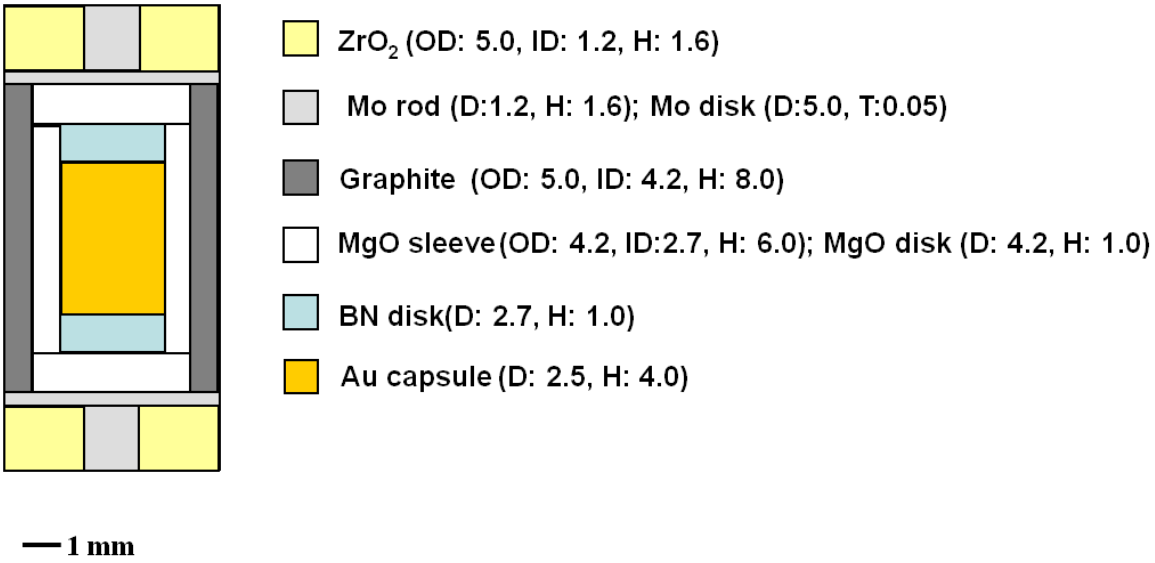

Fig.4.1 Cell assembly for high pressure/temperature synthesis of $CaIr_{1-x}Pt_xO_3$ (x = 0.3, 0.5, 0.7) using Multi-anvil apparatus (it is designed to sustain high P/T condition: 15GPa, 1300 ℃) (OD: outer diameter; ID: inner diameter; D: diameter; H: height; T: thickness)

4.2 Experimental analysis

The needle-like single crystals and polycrystalline samples of $CaIrO_3$ and polycrystalline samples of $CaIr_{1-x}Pt_xO_3$ (x = 0.3, 0.5, 0.7) synthesized at high pressure/temperature conditions were investigated using SEM and Raman spectroscopy and compositions determine by EMPA. Analysis of run products will be explained in detail in the following sections.

4.3 SEM studies: The morphology of $CaIr_{1-x}Pt_xO_3$

SEM measurement was conducted using a Phillips XL30CP, with PGT Spirit X-ray analysis. Samples were carbon coated with the thickness of ~10 nm before measurements to prevent surface charging effects. An acceleration voltage of 20 kV, an acceleration current of 1 nA was used and both secondary and backscattered electron images of the samples obtained. Qualitative chemical analysis was performed using EDX with the counting time of 60 s.

Fig.4.3.1(a) and Fig.4.3.1(b) show secondary electron and back scattered images of the needle-like shaped single crystalline sample of $CaIrO_3$. The grain size of the single crystalline $CaIrO_3$ was found to be around 0.02 mm x0.02 mm x0.1-8.0 mm. Crystal grains (cross section size: 8μm x: 8μm) of polycrystalline $CaIrO_3$ synthesised by piston-cylinder apparatus share the same needle-like morphology (Fig.4.3.3(a)). According to previous TEM studies of fine-grained $CaIrO_3$ (Miyajima et al., 2006)[57], grains of $CaIrO_3$ post-perovskite are expected to grow in the crystallographic *a*-axis

direction. Therefore, the long axis of the single crystalline $CaIrO_3$ will be [1 0 0] in Fig.4.3.1(a) and Fig.4.3.1(b). The cross section of the single crystal was observed by tilting the plane normal to the sample holder (Fig.4.3.2(a)). The motivation of such observation is to obtain more information about the morphology of $CaIrO_3$. The morphology of the single crystalline $CaIrO_3$ is characterized by the repetition of parallel lines as if they are forming layers (Fig.4.3.2(a)). As these lines exist within the cross section, they are perpendicular to [1 0 0]. Therefore, the parallel lines in Fig.4.3.2(a) and Fig.4.3.2(b) are likely to be the crystallographic *c*-axis of $CaIrO_3$ since the crystallographic *b*-axis is the interlayer direction of the layered post-perovskite structure, which is in good agreement with the texture analysis (which will be discussed in Chapter 5), stating that the grains of $CaIrO_3$ tend to lie with the (0 0 1) plane on the sample holder.

EDX analysis of all $CaIrO_3$ and $CaIr_{1-x}Pt_xO_3$ samples revealed peaks from Ca, Ir, Pt and O, with no trace of additional elements. The crystal grains of $CaIr_{1-x}Pt_xO_3$ samples (x = 0.3, 0.5, 0.7) show elongated rod like morphology in SEM image (Fig.4.3.3(b) – Fig.4.3.3(d)) instead of the needle-like morphology observed for $CaIrO_3$ (Fig.4.3.3(a)). Mean cross sectional grain size of $CaIrO_3$ and $CaIr_{1-x}Pt_xO_3$ (x = 0.3, 0.5, 0.7) varies between samples from 1 mm to 8mm as shown in Table 4.3. The grain growth for x = 0.5 is greater than for the other two compositions suggesting that the minimum melting point in the $CaIr_{1-x}Pt_xO_3$ series is near the x = 0.5 position. It is worthwhile to note that solid solutions share *a*-axis elongated needle-like grain-growth feature with $CaIrO_3$ and $CaPtO_3$, which has been previously reported by Hirai et al.[16], Ohgushi et al.[17] and Miyajima et al.[60].

(a) (b)

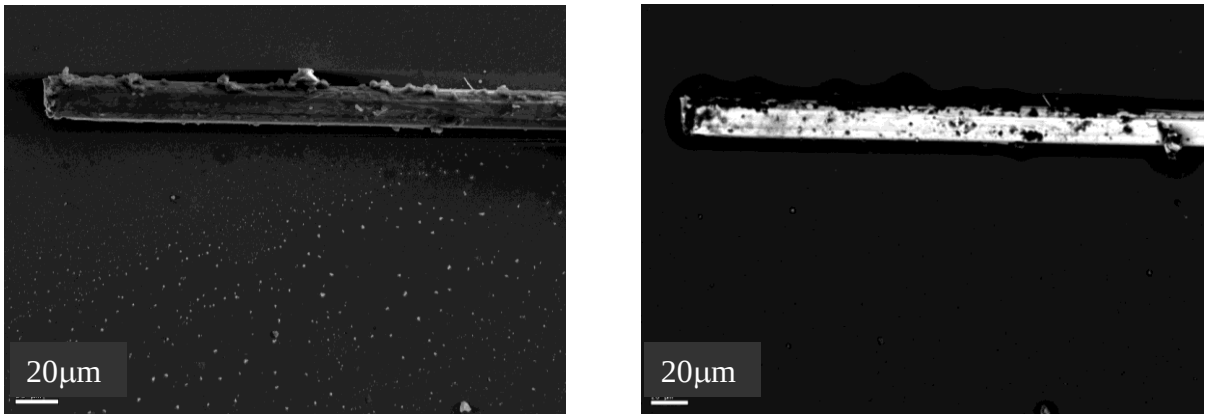

Fig.4.3.1 (a) Secondary electron image and (b) Backscattered electron image of the surface of $CaIrO_3$ single crystal

(a) (b)

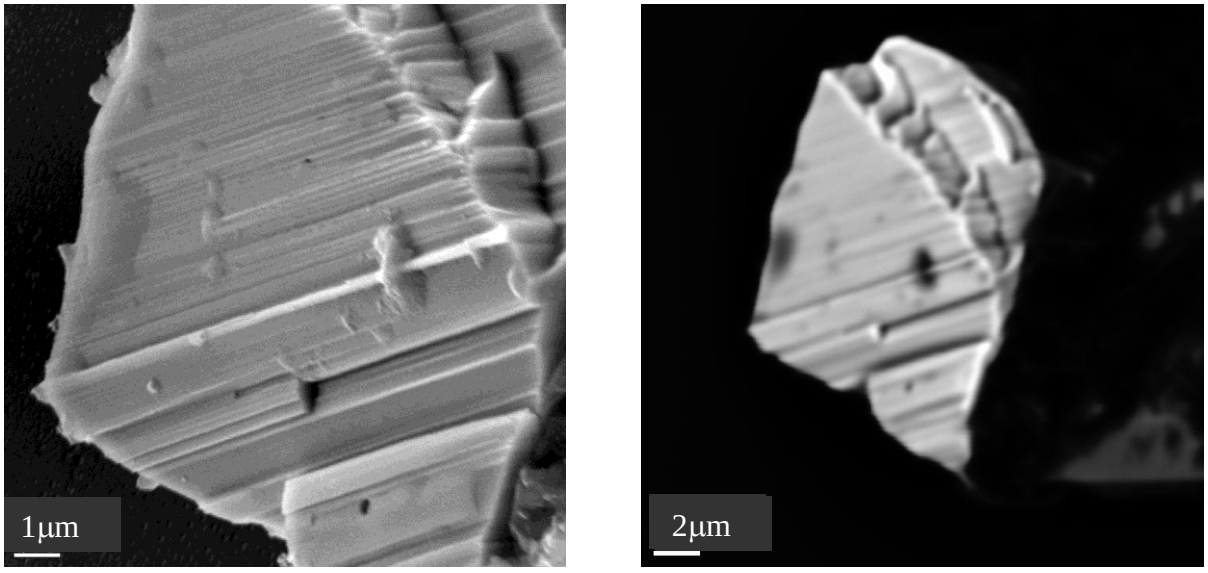

Fig.4.3.2 (a) Secondary electron image and (b) Backscattered electron image of the cross section of $CaIrO_3$ single crystal

(a) (b)

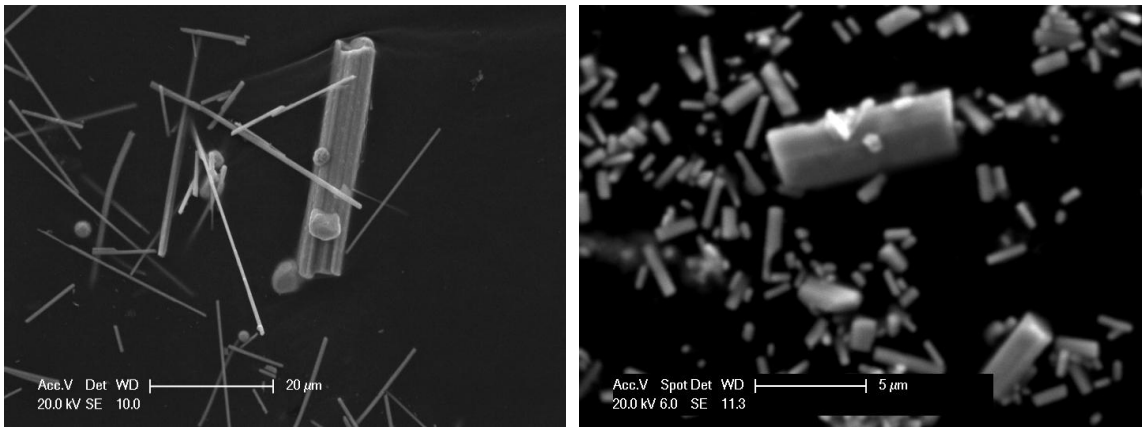

(c) (d)

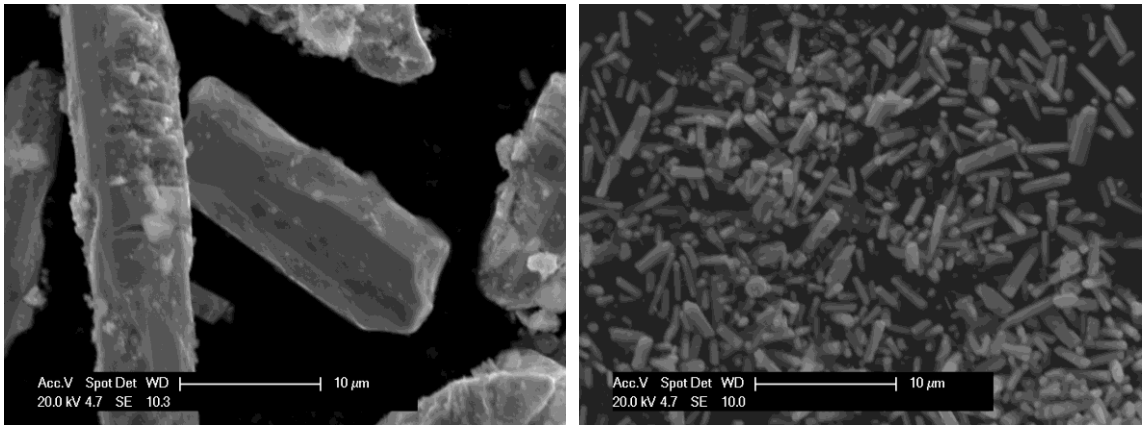

Fig.4.3.3 Typical SEM image of grains of $CaIr_{1-x}Pt_xO_3$ for (a) x = 0 (scale bar: 20 μm), (b) x = 0.3 (5 μm), (c) x = 0.5 (10 μm), (d) x = 0.7 (10 μm)

Table 4.3 Crystal grain size of the $CaIr_{1-x}Pt_xO_3$ (x = 0, 0.3, 0.5, 0.7) series, showing maxima among the series for x = 0 and x = 0.5 sample

Compounds	$CaIrO_3$	$CaIr_{0.7}Pt_{0.3}O_3$	$CaIr_{0.5}Pt_{0.5}O_3$	$CaIr_{0.3}Pt_{0.7}O_3$
Grain size (μm)	8.0	1.0	8.0	2.0

4.4 Electron Microprobe analysis on $CaIr_{1-x}Pt_xO_3$

Samples were embedded in an epoxy resin and polished using diamond paste in order to achieve flat surfaces. Electron probe micro-analysis was conducted under a vacuum of 10^{-5} Pa using a CAMECA SX100 with five vertical crystal WDS spectrometers and a PGT Spirit energy dispersive analyser. Polished samples (including the sample standard) were carbon coated with the thickness of ~10 nm prior to examination. Quantitative chemical analysis was conducted under the condition of acceleration voltage: 15 kV and acceleration current: 20 nA.

$CaIrO_3$ perovskite was used as a WDX standard for Ca, Ir and O in order to solve the stoichiometry of $CaIrO_3$ post-perovskite, while $CaIrO_3$ post-perovskite and a flat platinum disk were used as WDX standards for solving the stoichiometry of $CaIr_{1-x}Pt_xO_3$ solid solutions (x = 0.3,0.5,0.7). Since different thermal expansion parameters of $CaIrO_3$ post-perovskite were reported depending on synthesis conditions, its stoichiometry was solved by the $CaIrO_3$ perovskite. $CaIrO_3$ perovskite was used as a standard since its stoichiometry has been reported previously by McDaniel et al.(1972) [61] and a large crystal grain over 40 μm x 40 μm (Fig.4.4.1(c)) can be grown at ambient pressure. Martin et al.(2007)[33] synthesized the sample at high P/T condition (P: 6 GPa, T: 1223 K) and obtained the thermal expansion parameter: 2.84(3) x 10^{-5} K^{-1}, while Lindsay-Scott et al.(2007)[62] synthesized the sample at ambient pressure and obtained the thermal expansion parameter: 2.42(3) x 10^{-5} K^{-1}. Thus, I conducted WDX analysis on two different samples of $CaIrO_3$ post-perovskite synthesized at high pressure and at ambient pressure. One sample was synthesized in an evacuated silica tube at ambient pressure by sintering CaO and IrO_2

at 1000 ℃ for 20 hrs, while the other sample was synthesized at a high P/T condition (P: 2 GPa, T: 1100 ℃) by annealing CaO and IrO_2 for 30min using a piston-cylinder. Data were collected from selected 20 points of the crystal grains of the samples shown in Figures 4.4.1(a)-(c). Both samples showed no difference in the stoichiometry from $CaIrO_3$ perovskite, with no evidence in either sample of non-stoichiometry related to, for example, presence of oxygen vacancies (Table 4.4.1). In other words, both $CaIrO_3$ perovskite and $CaIrO_3$ post-perovskite have the satisfactory stoichiometry of 1: 1: 3. The standard deviation of oxygen composition is much smaller than others, since the perovskite standard has the same chemical formula as the post-perovskite specimen, and also because all the Ir impurity resulted from the reduced IrO_2, which could not react during the CaO-IrO_2 solid state reaction. Therefore, the difference in the reported thermal expansion parameter must be due to the extrinsic error such as the amount of Ir or IrO_2 impurities coming from different techniques, instrumental artefacts etc. instead of an intrinsic error. On the basis of this observation, $CaIrO_3$ post-perovskite was used as a standard for further WDX analysis in order to identify the stoichiometry of $CaIr_{1-x}Pt_xO_3$ solid solutions (x = 0.3, 0.5, 0.7). The WDX data were collected from 20 selected points of the sample grain (Fig.4.4.2(a)-(c)). Table 4.4.2 shows that the difference between the expected and the experimentally observed atomic ratio of Ir/Pt are within the statistical error, implying the satisfactory stoichiometry of solid solutions, consistent with the observation that samples consist of 100% post-perovskite phase with no additional phases present. This is a good evidence that high-pressure synthesis of $CaIr_{1-x}Pt_xO_3$ solid solutions (x = 0.3, 0.5, 0.7) were successful, and justifies the use of samples for determining physical properties of post-perovskite solid

solutions.

Table 4.4.1 Atomic percentage of elements within $CaIrO_3$ post-perovskite (two samples) and $CaIrO_3$ perovskite (sample standard) calculated from Wavelength Dispersive X-ray analysis data for 20 selected points on the crystal grains, which show that the difference of chemical formula between these samples are only within the standard deviation. The standard deviation of oxygen composition is much smaller than others, since the perovskite standard has the same chemical formula as the post-perovskite specimen, and also because all the IrO_2 residue from the solids state reaction had been reduced to Ir.

(AP denotes that the sample was synthesized at ambient pressure, while HP denotes that the sample was synthesized at a high pressure/temperature condition)

Compounds	Ca (%)	Ir (%)	O (%)
$CaIrO_3$ perovskite	20.0(2)	20.0(14)	60.0(0)
$CaIrO_3$ post-perovskite AP	20.0(2)	20.0(15)	60.0(0)
$CaIrO_3$ post-perovskite HP	20.0(3)	20.0(14)	60.0(0)

(a)

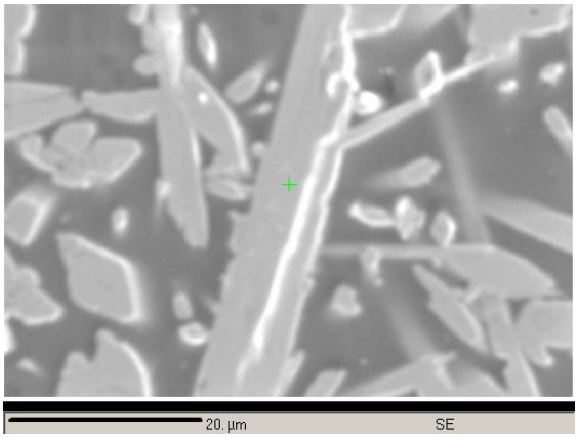

(b)

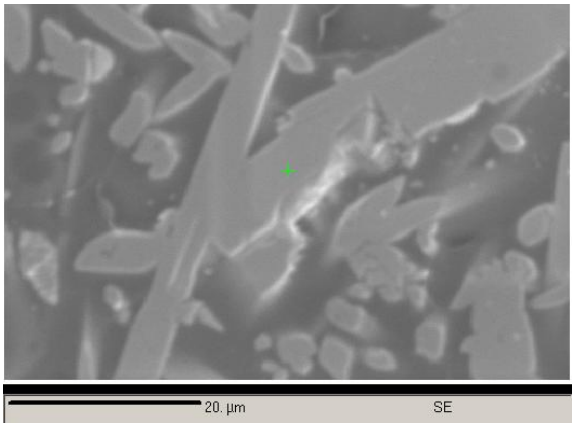

(c)

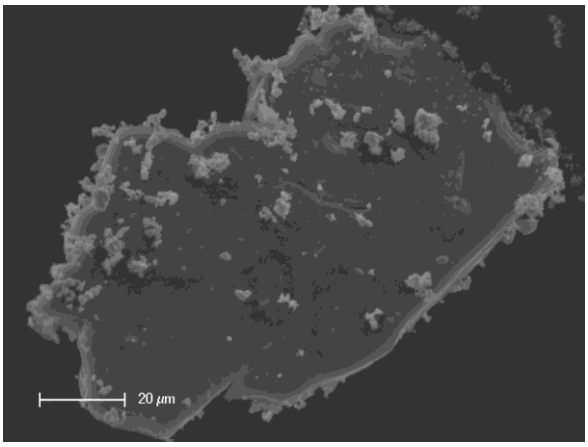

Fig.4.4.1: The SEM image of selected sample grains of (a) $CaIrO_3$ post-perovskite synthesized at ambient pressure (scale bar = 20 μm), (b) $CaIrO_3$ post-perovskite synthesized at a high pressure/temperature condition (scale bar = 20 μm) and (c) $CaIrO_3$ perovskite which were used for Wavelength Dispersive X-ray analysis (scale bar = 20 μm)

Table 4.4.2 Atomic percentage of elements and Ir/Pt ratio within $CaIr_{1-x}Pt_xO_3$ series (x = 0.3, 0.5, 0.7) calculated from Wavelength Dispersive X-ray analysis data for 20 selected points on the crystal grains, which show that the deviation from the ideal chemical formula is smaller than the standard deviation for all compounds synthesised at 15 GPa, 1300 ℃

(Ir/Ir+Pt ratio is calculated in order to compare it with the atomic ratio of the synthesis product expected from the starting material for each solid solution)

Compounds	Ca (%)	Ir (%)	Pt (%)	O (%)	Ir/Ir+Pt
$CaIr_{0.3}Pt_{0.7}O_3$	21.0(3)	6.6(10)	12.7(16)	59.7(1)	0.34(7)
$CaIr_{0.5}Pt_{0.5}O_3$	20.2(3)	10.6(12)	9.3(15)	59.9(1)	0.53(7)
$CaIr_{0.7}Pt_{0.3}O_3$	20.2(8)	14.5(18)	5.4(13)	59.9(2)	0.73(7)

(a)

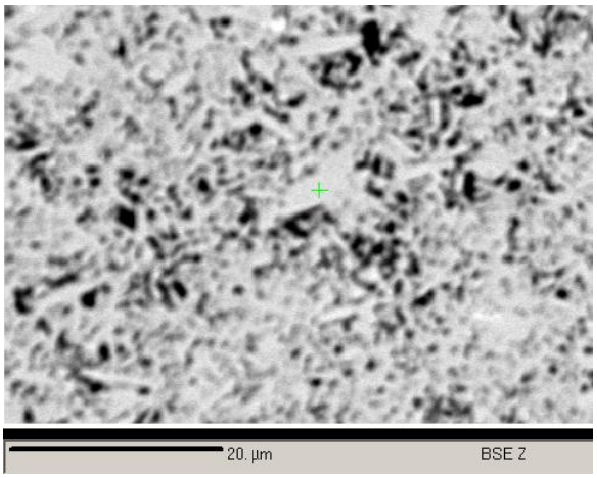

(b)

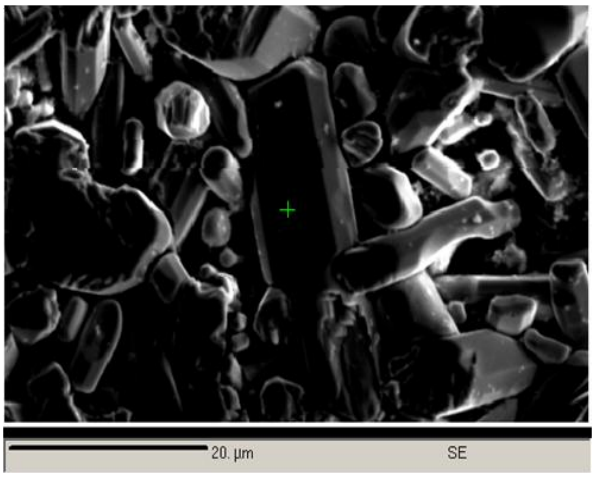

(c)

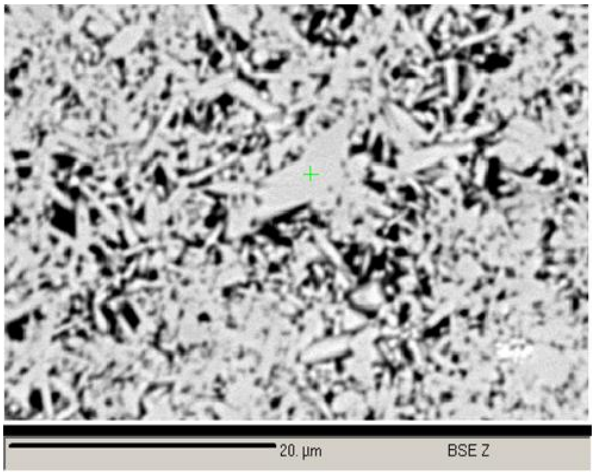

Fig.4.4.2 The SEM image of selected sample grains of $CaIr_{1-x}Pt_xO_3$ for (a) x = 0.3, (b) x = 0.5 and (c) x = 0.7 which were used for Wavelength Dispersive X-ray analysis (As x = 0.5 sample has a large crystal grain over 8 μm with elongated rod-like morphology, adequate polishing of all the crystal grains were not achieved. However, this problem was solved by conducting WDX analysis on the selected crystal grain with flat surface with green crosses)

4.5 Raman scattering of $CaIr_{1-x}Pt_xO_3$

Room-pressure Raman spectra on $CaIrO_3$ and $CaIr_{1-x}Pt_xO_3$ (x = 0.3, 0.5, 0.7) were obtained using a Jobin Yvon LabRAM analytical Raman Microscope. The laser used for the experiment was a 63.0 mW helium-neon laser, which produces monochromatic light at a wavelength of 632.8nm (the laser was polarized on the plane perpendicular to the direction of propagation). Raman spectroscopy studies were conducted at ambient conditions in order to identify single crystalline $CaIrO_3$ and powdered $CaIrO_3$. Raman spectra of single crystal $CaIrO_3$ and powdered $CaIrO_3$ samples (Fig.4.5.1) were similar to those obtained by Hirose et al. (2005)[32] and Hustoft et al.(2008)[38], demonstrating that they are of the post-perovskite phase of $CaIrO_3$.

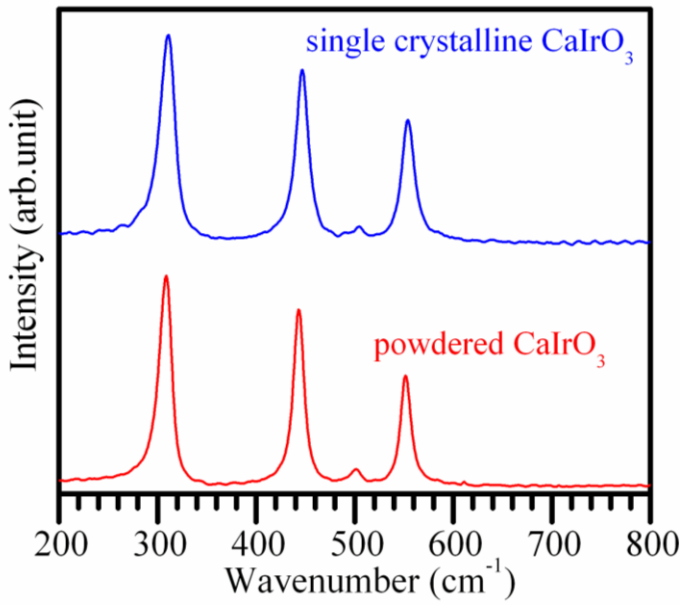

Fig.4.5.1 Raman spectra of single crystalline and powdered $CaIrO_3$ post-perovskite with laser power of 25% (15.8 mW)

First, the accidental attempt of changing the HeNe laser power resulted in an interesting observation. Laser power-dependent Raman spectra were observed when the crystallographic *a*-axis was in plane with the polarization of the HeNe laser (Fig.4.5.2).

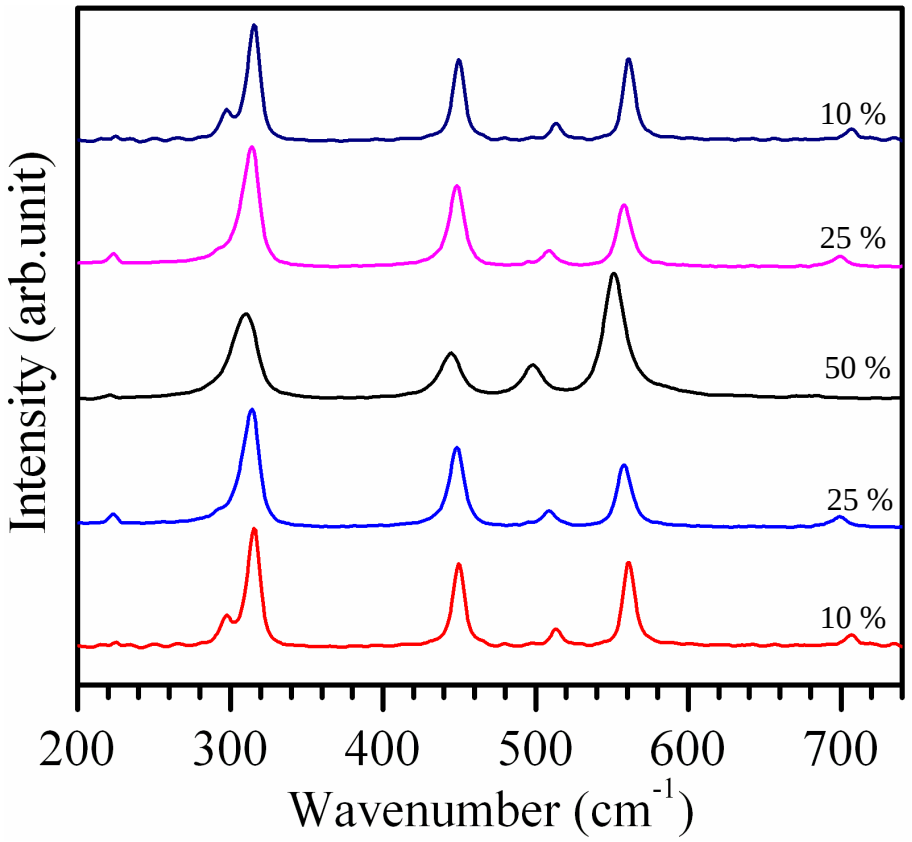

Fig.4.5.2 Laser power-dependent Raman spectra of single crystalline $CaIrO_3$ with the crystallographic *a*-axis parallel to the polarization of the HeNe laser (spectra are offset vertically as a function of time; laser power was first increased and then decreased to determine whether changes in spectra were recoverable).

The Raman peak around 310 cm^{-1} split into two at a laser power of 10 % (6.30 mW), while only a single peak around 310 cm^{-1} was detected for the laser power of 25 % (15.8 mW) and 50 % (31.5 mW). Also, a Raman peak around 700 cm^{-1} was detectable at a laser power of 10 % and 25 %, while it disappeared at the laser power of 50 %. The spectra at 10 % and 25 % were recoverable after the sample was radiated by the laser with 50 % power, implying that changes in spectra were not due to some laser heating effect. Changes in spectra can be attributed to peak broadening resulting from photo-induced conductivity effect of $CaIrO_3$ by the HeNe laser. The disappearance of the Raman peak around 300 cm^{-1} and 700 cm^{-1} (Fig.4.5.2) implies that this process starts at a laser power of 25 %, and goes further at the laser power of 50 %.

Second, the orientation of the single crystal was varied during the measurement in order to obtain information about how structural anisotropy affects Raman active modes with different symmetries. Fig.4.5.3 shows the comparison of the Raman spectra of single crystal $CaIrO_3$ in 2 different orientations with respect to the direction of polarization of the laser. The observed number of modes in Raman spectra varied with the crystallographic *a*-axis direction of the crystal with respect to the polarization of the laser beam (Fig.4.5.3). The laser power was set to 25 % when these orientation-dependent Raman spectra were collected. The orientation-dependent Raman spectra of the single crystal (Fig.4.5.3) imply that 2 Raman-active modes disappear by switching the orientation from parallel to vertical. Powdered samples of $CaIrO_3$ show Raman spectra similar to the latter one. This can be explained in terms of grain texture. As will be mentioned in Chapter 5, the grains of $CaIrO_3$ tend to sit with the (0 0 1) plane on the sample holder. However, there are some grains

which sit with the (0 1 0) plane on the holder. There are 2 obvious crystal faces for the single crystal shown in Fig.4.5.3: these are likely to be (0 0 1) and (0 1 0).

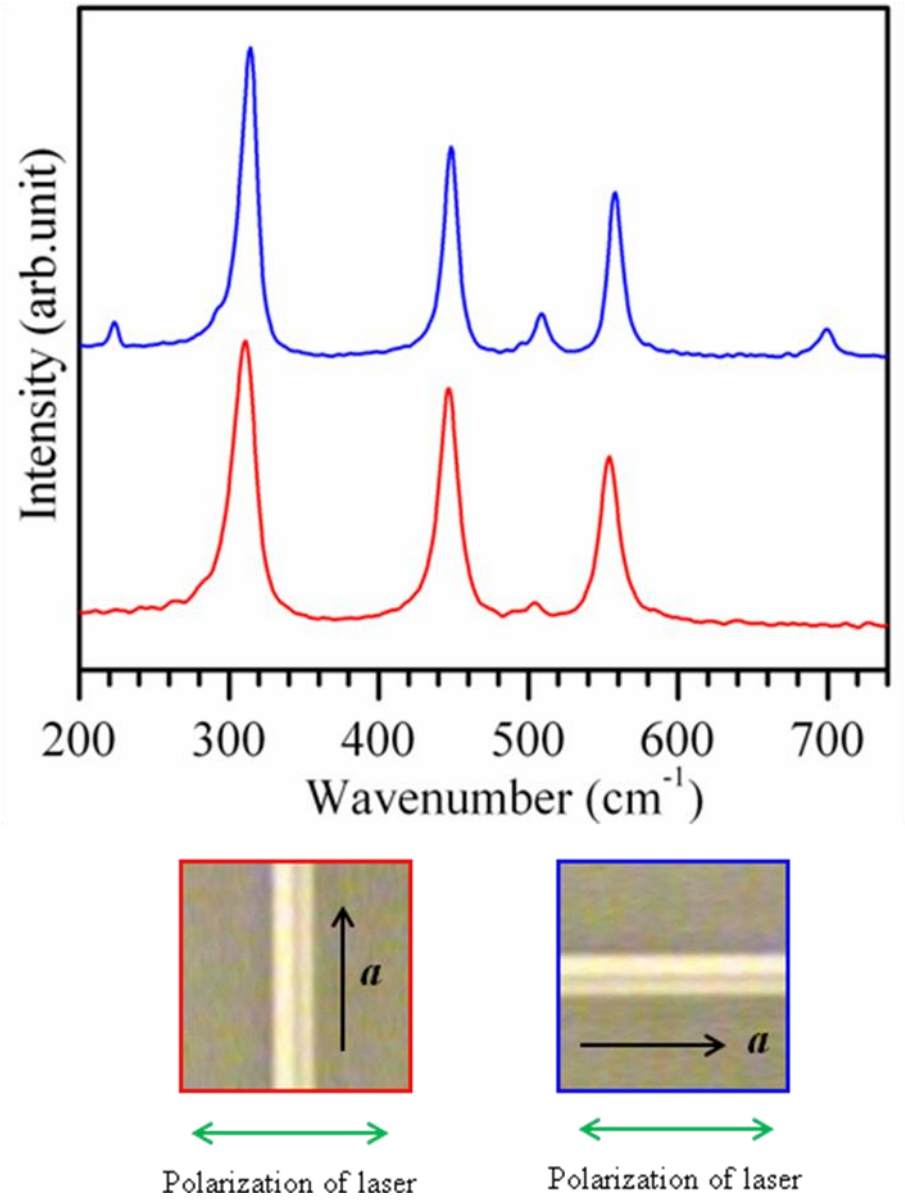

Fig.4.5.3 Orientation-dependent Raman spectra of single crystalline $CaIrO_3$ with HeNe laser power of 25% (15.8 mW). Crystal orientation image for each Raman spectrum (red / blue) is shown at the bottom of the figure, along with the laser polarization and the *a*-axis.

When the crystallographic *a*-axis is parallel to the polarization of the beam, the phonon modes related to displacement of *y* and *z* will be observed together since both (0 0 1) and (0 1 0) plane are parallel with respect to the polarized plane. On the other hand, when the crystallographic *a*-axis is vertical to the polarization of the beam, the phonon mode related to displacement of *y* and *z* will be observed separately since either (0 0 1) or (0 1 0) plane is vertical with respect to the polarized (1 0 0) plane of the laser. Thus, the information regarding the displacement of *z* is likely to be lost by changing the crystal orientation due to the favouring of [0 1 0] growth for $CaIrO_3$ (see Chapter 5, p.124 for detail). Among the 12 Raman-active modes ($4A_g + 3B_{1g} + B_{2g} + 4B_{3g}$) of $CaIrO_3$, 9 Raman-active modes ($3A_g + 3B_{1g} + 3B_{3g}$) correspond to the displacement of *y*, while 3 Raman-active modes ($A_g + B_{2g} + B_{3g}$) correspond to the displacement of *z* (B_{3g} includes the displacement of both *y* and *z*). According to group theory, the expected number of Raman modes corresponding to the displacement of *z* is 3, while 4 Raman bands were observed in reality (Fig.4.5.3). In conclusion, such crystal orientation-dependent Raman spectra suggest that one has to be aware that the information of displacement *z* for O2 can be lost depending on the orientation of $CaIrO_3$ crystal grain.

In order to investigate the evolution of Raman-active modes with Pt content, Raman spectra of $CaIr_{1-x}Pt_xO_3$ (x = 0, 0.3, 0.5, 0.7) were obtained at room T. Fig.4.5.4(a)-Fig.4.5.4(c) show the Raman spectra of $CaIr_{1-x}Pt_xO_3$ series (x = 0.3, 0.5,0.7) at ambient conditions, which were collected by placing the grain target in an appropriate orientation, so that maximum number of Raman shifts could be observed. Also the laser power was set to 10 % and 25 % for $CaIrO_3$ and 25 % for solid solutions, in order to avoid total

metallization of the sample by the laser. Table 4.5.1 shows the Raman shifts of $CaIr_{1-x}Pt_xO_3$ series identified by analyzing those Raman spectra.

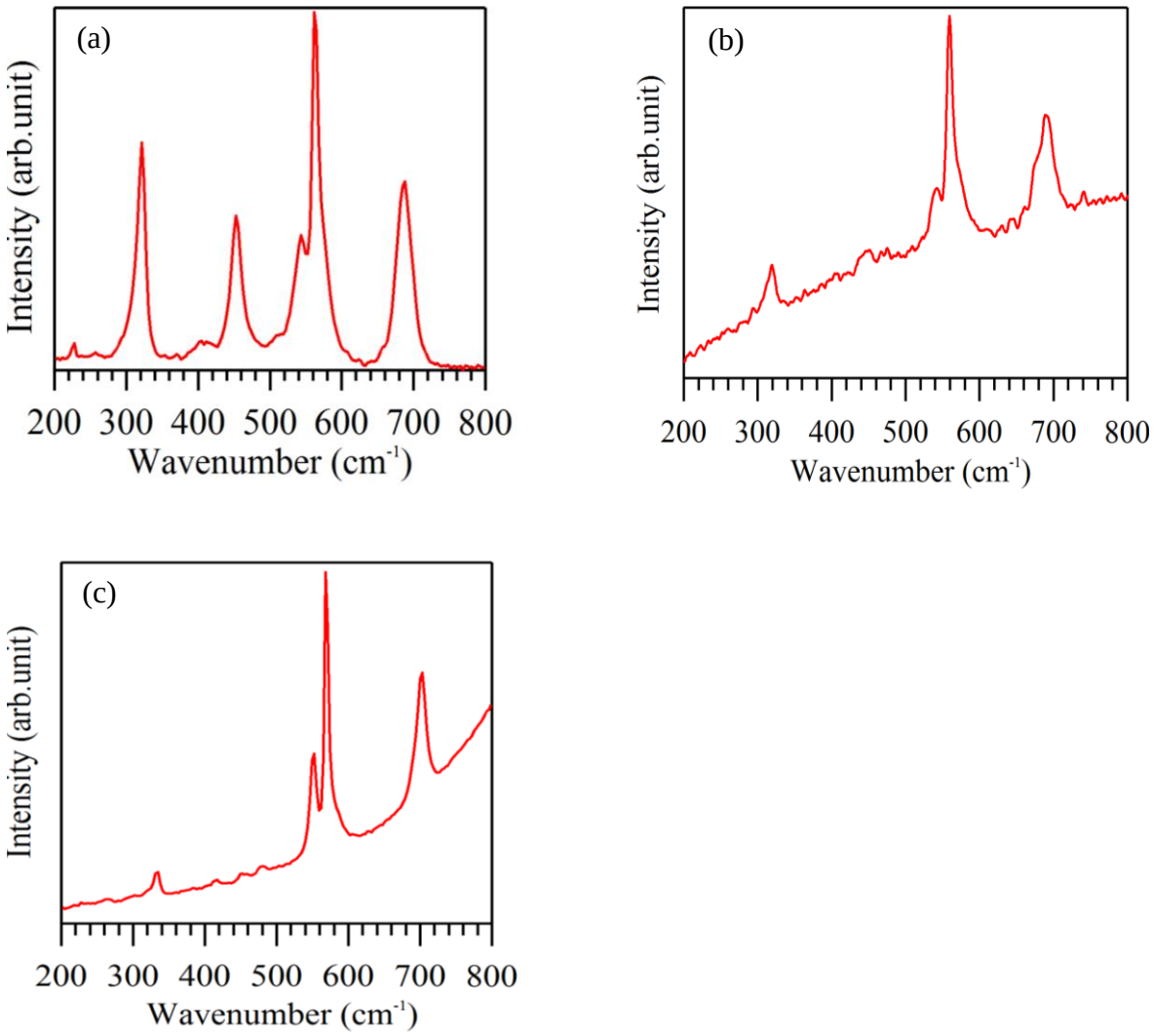

Fig.4.5.4 Raman spectra of $CaIr_{1-x}Pt_xO_3$ for (a) x = 0.3, (b) x = 0.5 and (c) x = 0.7 with laser power of 25 % (15.8 mW)

Table 4.5.1: Raman shifts (290K, 1bar) which characterize the Raman–active modes of $CaIr_{1-x}Pt_xO_3$ (maximum number of observed Raman shifts are listed in order to compare with one another among the solid solutions)

Wavenumber (cm^{-1})	$CaIrO_3$	$CaIr_{0.7}Pt_{0.3}O_3$	$CaIr_{0.5}Pt_{0.5}O_3$	$CaIr_{0.3}Pt_{0.7}O_3$
ν_1	223	226	-----	-----
ν_2	298	294	297	318
ν_3	311	322	320	334
ν_4	445	452	451	452
ν_5	500	-----	-----	-----
ν_6	552	543	544	553
ν_7	-----	562	559	568
ν_8	700	688	692	703

According to the group theory, there are 12 Raman-active modes ($4A_g + 3B_{1g} + B_{2g} + 4B_{3g}$) out of 30 phonon modes ($4A_g + 2A_u + 3B_{1g} + 6B_{1u} + B_{2g} + 6B_{2u} + 4B_{3g} + 4B_{3u}$) for *Cmcm* symmetry in post-perovskite regime. Table 4.5.1 shows that 8 out of 12 Raman-active modes were observed for the $CaIr_{1-x}Pt_xO_3$ series, which is considerably more than the previous study on $CaIrO_3$ by Hustoft et al.(2008)[38]. The Ir and Pt atoms do not participate in the Raman-active phonon modes due to their atomic site symmetry (: 4a), while post-perovskite structure has 4 structural degree of freedom (Ca: 1, O1: 1, O2: 2) out of 12 atomic coordinates. The symmetry and the broadening of Raman mode peaks were

observed for $CaIr_{1-x}Pt_xO_3$ series (x = 0, 0.3, 0.5, 0.7) (Fig.4.5.4). This feature implies that photo-induced metallization process is starting in these compounds since they only have a small band gap and it can be easily lifted by sufficient power of HeNe laser. The Raman-active mode near 310 cm^{-1} splits into two (ν_2 and ν_3) over the $CaIr_{1-x}Pt_xO_3$ series. This peak splitting happened at a wide range of laser power (below 50%) for $CaIr_{1-x}Pt_xO_3$ solid solutions (x = 0.3, 0.5, 0.7), while it only happened at a narrow range of power (below 10%) for $CaIrO_3$. This can be explained in terms of the band structure of these compounds. As $CaIrO_3$ has a narrower band gap and higher conductivity than other series showing near-metallic features, photo-induced metallization can easily happen for $CaIrO_3$ and it will kill the vibration mode present in a nonmetallic phase which corresponds to the Raman shift near 300cm^{-1} (ν_2). This observation suggests that Raman spectroscopy is a useful tool to compare the physical properties of compounds with each other when they are semiconducting, especially for 5d transition metal oxides. The Raman mode near 563 cm^{-1} is present for $CaIr_{1-x}Pt_xO_3$ (x = 0.3, 0.5, 0.7), while it is not present for the post-perovskite phase of $CaIrO_3$. The Raman mode near 563 cm^{-1}, which is present for $CaIr_{1-x}Pt_xO_3$ (x = 0.3, 0.5, 0.7) and not visible for $CaIrO_3$, indicates that the strong attraction of O atoms toward the Pt atoms plays an important role in the vibration modes related to PtO_6 octahedra. In other words, the strengthening of the vibration modes that are responsible for O atoms due to the slightly stronger attraction of O atoms toward the Pt atoms gives rise to the Raman mode near 563 cm^{-1}. The Raman mode of $CaIrO_3$ observed near 500 cm^{-1} (ν_5) is not visible for $CaIr_{1-x}Pt_xO_3$ solid solutions, which indicates that vibrations involving O atoms are possibly affected by a weak Jahn-Teller distortion of the IrO_6 octahedron for $CaIrO_3$. The

Raman-active mode near 220 cm^{-1}(ν_1) is present for $CaIrO_3$ and $CaIr_{0.7}Pt_{0.3}O_3$, while it is not present for $CaIr_{0.5}Pt_{0.5}O_3$ and $CaIr_{0.3}Pt_{0.7}O_3$. This is likely to come from the crystal morphology. As will be explained in detail in Chapter 5, (0 0 1) planes tend to face the laser for $CaIrO_3$, while (0 1 0) plane tend to face the laser for $CaIr_{1-x}Pt_xO_3$ (x = 0.3, 0.5, 0.7). Since increased tendency of the favouring of (0 1 0) over (0 0 1) planes happens with the increase of Pt content (see Chapter 5 for detail), the Raman scattering from the (0 0 1) plane is likely to result in the Raman-active mode near 220 cm^{-1}(ν_1). In other words, the Raman-active mode near 220 cm^{-1} is likely to be coming from the vibration mode regarding the O2 atom. This observed dependence of Raman scattering on external morphology suggests the importance of synthesizing solid solutions in order to fully cover the Raman-active modes for further interpretation of phonon modes, especially for those which have strong preferred orientation, such as post-perovskite compounds with needle-like morphology.

Raman shift is not the only indicator of phonon behaviour in the lattice, and Raman intensity can be a valuable information source when it is related to the number of phonons in the phonon bands responsible for lattice vibration. As the phonon bands in Raman scattering follow the Bose-Einstein statistics, the probability of finding a phonon (or a phonon band) with a wavenumber: ν in Stokes scattering is given as follows:

$$N(\nu) = 1/\{\exp(h\nu / 2k_BT)-1\}$$

As the Raman intensity *I* measured in the experiment is a photon count rate, it is proportional to $N(\nu)$ and $(\nu_0 - \nu)^3$, where $\nu_0 - \nu$ is the wavenumber of the photon. $N(\nu)$ and $(\nu_0 - \nu)^3$ can be calculated for each Raman-active mode (T = 290 K), and the number of

phonons in the phonon band regarding each Raman–active mode will be proportional to $I/\{N(\nu)*(\nu_0 - \nu)^3\}$. In order to compare phonon population in different experiments, $I/\{N(\nu)*(\nu_0 - \nu)^3\}$ has to be weighted by an appropriate value each time. Table 4.5.2 shows the phonon population $\rho(\nu)$ in the phonon bands corresponding with each Raman-active mode calculated for $CaIrO_3$ and $CaIr_{0.7}Pt_{0.3}O_3$ in this way. $CaIr_{0.7}Pt_{0.3}O_3$ was chosen as a representative of $CaIr_{1-x}Pt_xO_3$ solid solutions since they share similar features in the Raman spectra.

Table 4.5.2: Phonon population $\rho(\nu)$ in the phonon bands corresponding to each Raman-active mode for $CaIrO_3$ and $CaIr_{0.7}Pt_{0.3}O_3$ (the phonon population in the first Raman-active mode(ν_1) was used as an unit in order to compare $CaIrO_3$ with $CaIr_{0.7}Pt_{0.3}O_3$ in the same basis)

phonon population	$CaIrO_3$	$CaIr_{0.7}Pt_{0.3}O_3$
$\rho(\nu_1)$	1	1
$\rho(\nu_2)$	1	1
$\rho(\nu_3)$	9	11
$\rho(\nu_4)$	5	5
$\rho(\nu_5)$	0.8	-----
$\rho(\nu_6)$	3	4
$\rho(\nu_7)$	-----	13
$\rho(\nu_8)$	0.6	7

Apart from the 8th Raman band (ν_8), $CaIrO_3$ and $CaIr_{0.7}Pt_{0.3}O_3$ have similar phonon populations in each corresponding band. This implies that the phonon band structure of $CaIrO_3$ is similar to that of $CaIr_{0.7}Pt_{0.3}O_3$. As these two compounds have the same crystal structure with similar lattice constants and similar values of electronegativity (Ir/Pt), such similarity of phonon bands are reasonable. However, the phonon populations in the 8th Raman band differ greatly between $CaIrO_3$ and $CaIr_{0.7}Pt_{0.3}O_3$. $CaIr_{0.7}Pt_{0.3}O_3$ has much larger phonon population than $CaIrO_3$ for the 8th Raman band. $CaIrO_3$ is either a metal or a narrow bandgap (E_g: 0.13eV) semiconductor with high mobility of electrons, so the photo-induced excitation can take place and the 8th Raman band will disappear at a high laser power. However, $CaIr_{1-x}Pt_xO_3$ solid solutions have higher resistivity and larger band gaps, so photo-induced excitation is unlikely to happen. Indeed, the 8th Raman band of $CaIr_{1-x}Pt_xO_3$ solid solutions did not disappear at high laser powers (25% and 50%). This observation implies that the valence band is rigid in the case of $CaIr_{1-x}Pt_xO_3$ solid solutions, while a large portion of the valence band has already converged to the conduction band in the case of $CaIrO_3$.

4.6 High pressure Raman studies of $CaIr_{1-x}Pt_xO_3$

High pressure Raman spectroscopy studies on $CaIr_{0.5}Pt_{0.5}O_3$ were conducted using a laser-heated four-pin type diamond anvil cell (bevelled culet face diameter: 250 μm) with NaCl pressure medium and Renishaw RS-SYS 1000 (Ar laser: λ = 514.5 nm) (Fig.4.6.1) at GRC, Ehime University, Japan. The sample chamber (hole diameter: ϕ = 70 μm) for the sample and NaCl was drilled in a pre-indented Re gasket (thickness: 25 μm).

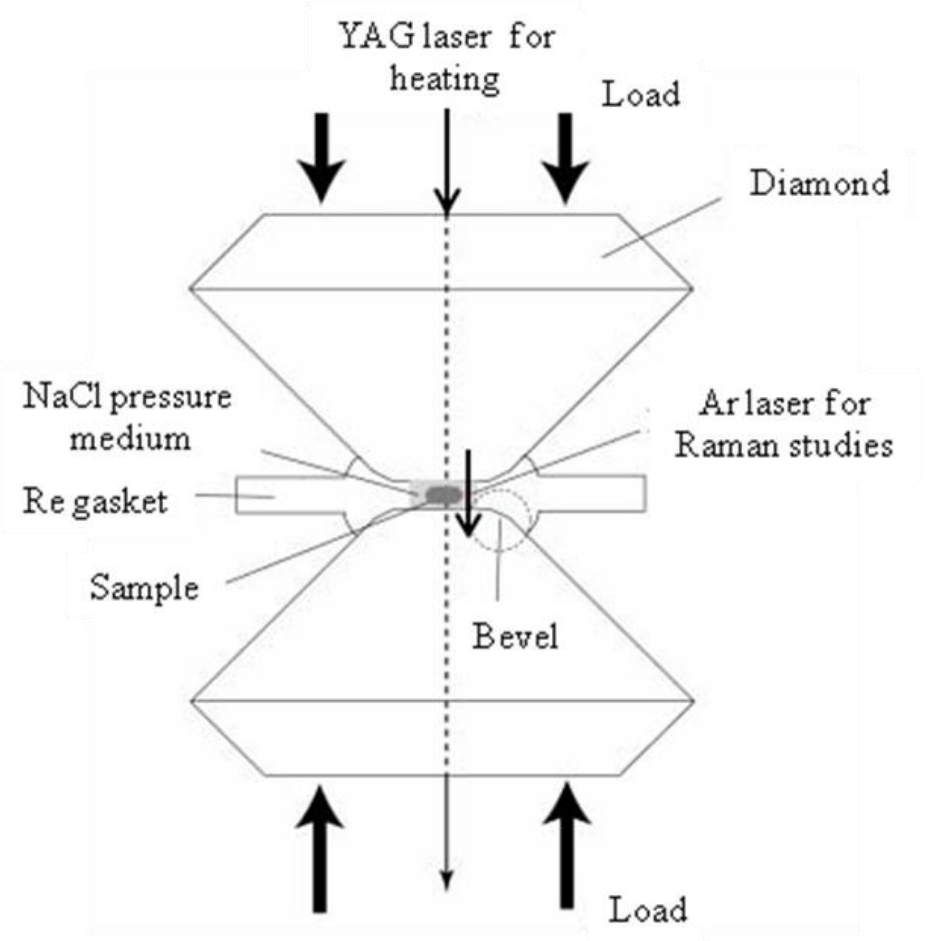

Fig.4.6.1 Schematic diagram of the bevelled diamond anvil cell used for the laser heating up to ~1900 K at 60 GPa, followed by high pressure Raman studies of the sample

High-pressure Raman spectra was obtained during pressurisation up to 60 GPa, after step heating to several high temperatures and then during decompression down to ambient pressure. The sample was step heated to ~1500 K, ~1700 K and ~1900 K for 10 minutes at each step by using double-sided laser heating system (Nd YAG laser: λ = 1072 nm) installed at GRC. Since these temperatures were estimated from the Planck-fit using the black body emission from the sample, they possess uncertainties up to 100K, but the double sided heating system minimizes such uncertainties to below 50K. Pressures were determined from diamond Raman shift (Akahama et al., 2004)[50], and temperatures were determined by spectroradiometric measurements of the light emitted from the sample under heating.

The post-perovskite to perovskite structural transformation at the mid-point of the $CaIrO_3$-$CaPtO_3$ solid solution was explored through a high pressure Raman spectroscopy study. $CaIr_{0.5}Pt_{0.5}O_3$ retains the post-perovskite structure on compression to 60 GPa; pressure-induced changes in Raman frequencies are shown in Table 4.6.1. Fig. 4.6.2 shows the room temperature Raman spectra from the sample at various steps during compression to 60 GPa, at 60 GPa before laser heating and after laser heating at ~1900 K, and then at various steps during subsequent decompression to ambient pressure. During compression to 60 GPa and prior to heating, no changes in the Raman spectra were observed other than gradual shift in frequency of Raman modes. Before heating the sample up to ~1900 K, step-wise heating at ~1500 K and ~1700 K was performed for 10 minutes, although again, no change in spectra consistent with a phase transition were noted (Fig.4.6.3). However, heating at 60 GPa, 1900K was sufficient to result in notable changes in the Raman spectra,

consistent with a phase transition to perovskite. Comparison of Fig.4.6.2 with the spectra in Fig.4.6.4(a), and that of $CaHfO_3$ perovskite (Park et al., 1976)[63], show that $CaIr_{0.5}Pt_{0.5}O_3$ transforms from post-perovskite ($CaIrO_3$) type to perovskite type on heating at 60 GPa. The perovskite phase persists on decompression (at room temperature) to 20 GPa, but reverts to the post-perovskite structure between 20 and 9 GPa (Fig.4.6.2). The Raman modes of the perovskite phase of $CaIr_{0.5}Pt_{0.5}O_3$ are shown in Table 4.6.2 and are plotted against pressure in Fig. 4.6.4. As the perovskite phase of $CaIr_{0.5}Pt_{0.5}O_3$ transformed back into post-perovskite at ~9GPa (Fig.4.6.2), it can be concluded that Pt-doped $CaIrO_3$ favours the post-perovskite structure over the perovskite structure at moderate pressures.

Table 4.6.1: The five primary Raman modes of post-perovskite phase of $CaIr_{0.5}Pt_{0.5}O_3$ at high pressures along with the mode Grüneisen parameters ($\gamma_{i,0}$) and its logarithmic volume derivative q

P (GPa)	ν_1 (cm^{-1})	ν_2 (cm^{-1})	ν_3 (cm^{-1})	ν_4(cm^{-1})	ν_5(cm^{-1})
0	322	448	545	565	692
9	337	467	586	599	733
30	378	534	651	681	840
50	403	569	693	748	917
60	416	582	714	766	943
$\gamma_{i,0}$	0.869	0.913	0.894	1.08	1.10
q	2.86	3.84	3.93	2.93	3.11

Simple average of $\gamma_{i,0}$, $<\gamma_{i,0}>$: 0.971

Weighted average of $\gamma_{i,0}$, $[\gamma_{i,0}]$: 0.952

Table 4.6.2: The seven primary Raman modes of perovskite phase of $CaIr_{0.5}Pt_{0.5}O_3$ at high pressures along with the mode Grüneisen parameters ($\gamma_{i,0}$); Raman modes of $CaMnO_3$ at ambient pressure (Abrashev et al., 2002) are shown for the purpose of mode assignment (P_0 denotes the data extrapolated to P = 0 using the linear pressure dependence)

P (GPa)	ν_1 (cm^{-1})	ν_2 (cm^{-1})	ν_3 (cm^{-1})	ν_4 (cm^{-1})	ν_5 (cm^{-1})	ν_6 (cm^{-1})	ν_7 (cm^{-1})
20	164	181	208	263	295	314	377
28	178	193	233	268	282	340	389
38	190	203	258	282	306	364	408
60	206	223	292	312	349	426	445
P_0	148	163	173	235	232	260	342
$CaMnO_3$	148	160	179	243	243	258	345
(P = 0)	$B_{2g}(4)$	$A_g(2)$	$B_{1g}(3)$	$A_g(7)$	$A_g(7)$	$B_{2g}(7)$	$A_g(6)$
$\gamma_{i,0}$	1.23	1.13	1.96	0.966	1.05	1.76	0.912

Simple average of $\gamma_{i,0}$, $\langle\gamma_{i,0}\rangle$: 1.29

Weighted average of $\gamma_{i,0}$, $[\gamma_{i,0}]$: 1.27

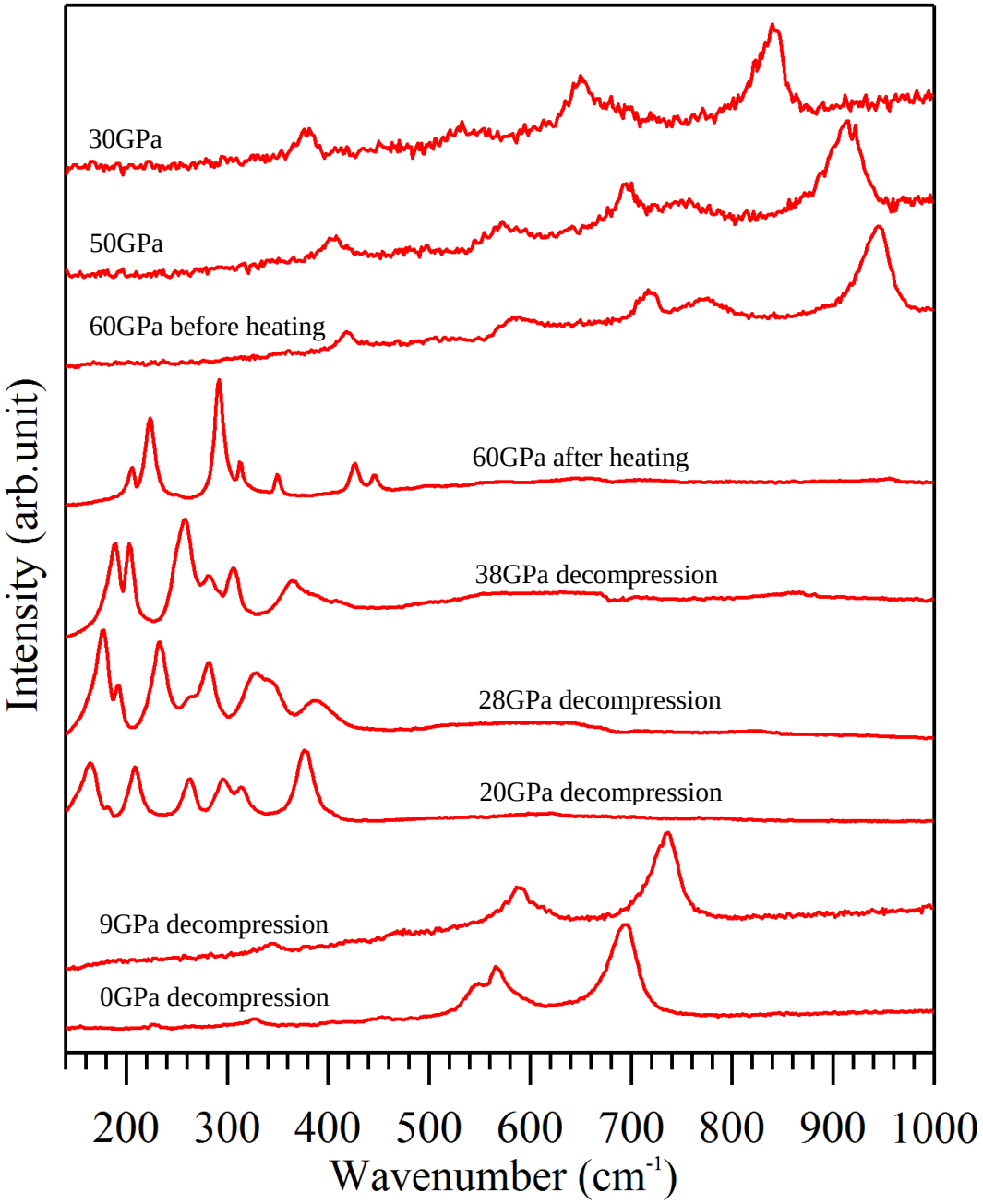

Fig.4.6.2 High-pressure Raman spectra of $CaIr_{0.5}Pt_{0.5}O_3$ for 30GPa, 50GPa and 60GPa before heating the sample by laser; for 60GPa after heating the sample at 1900K for 10 minutes by laser and then quenched; for 38GPa, 28GPa, 20GPa, 9GPa and 0GPa after decompression

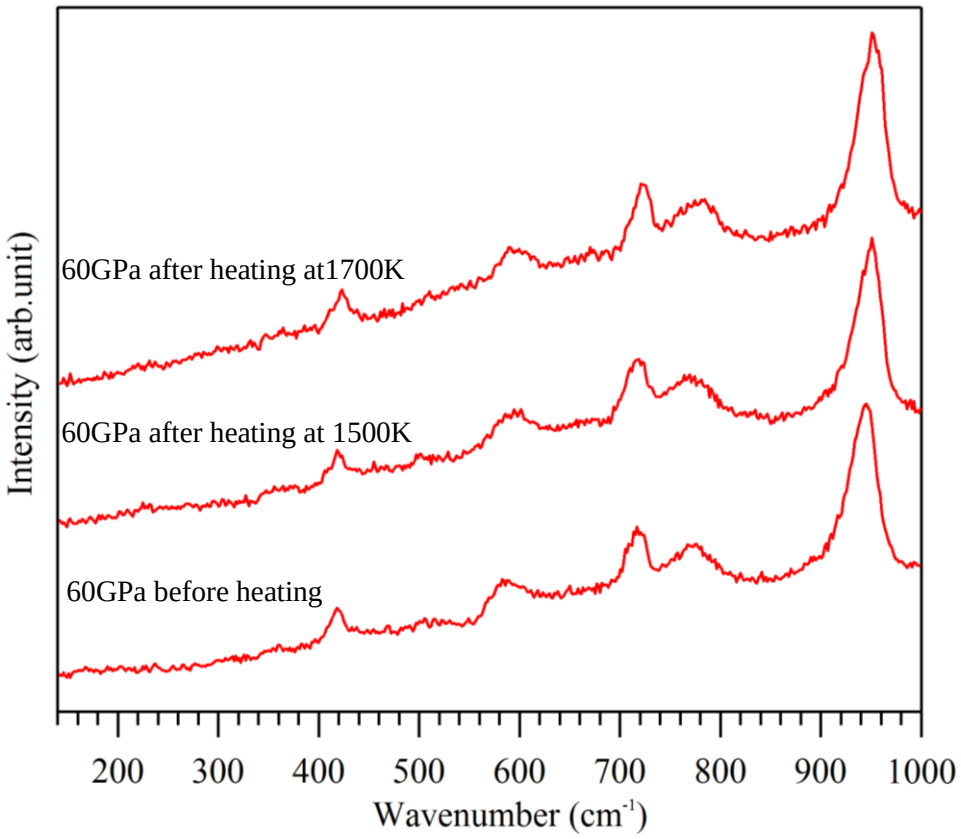

Fig.4.6.3 High-pressure Raman spectra of $CaIr_{0.5}Pt_{0.5}O_3$ at 60GPa before heating the sample by laser and after heating the sample at 1500 K and 1700 K for 10 minutes by laser, and then quenched; Post-perovskite phase of $CaIr_{0.5}Pt_{0.5}O_3$ at 60GPa does not show any transition by laser heating up to 1700 K

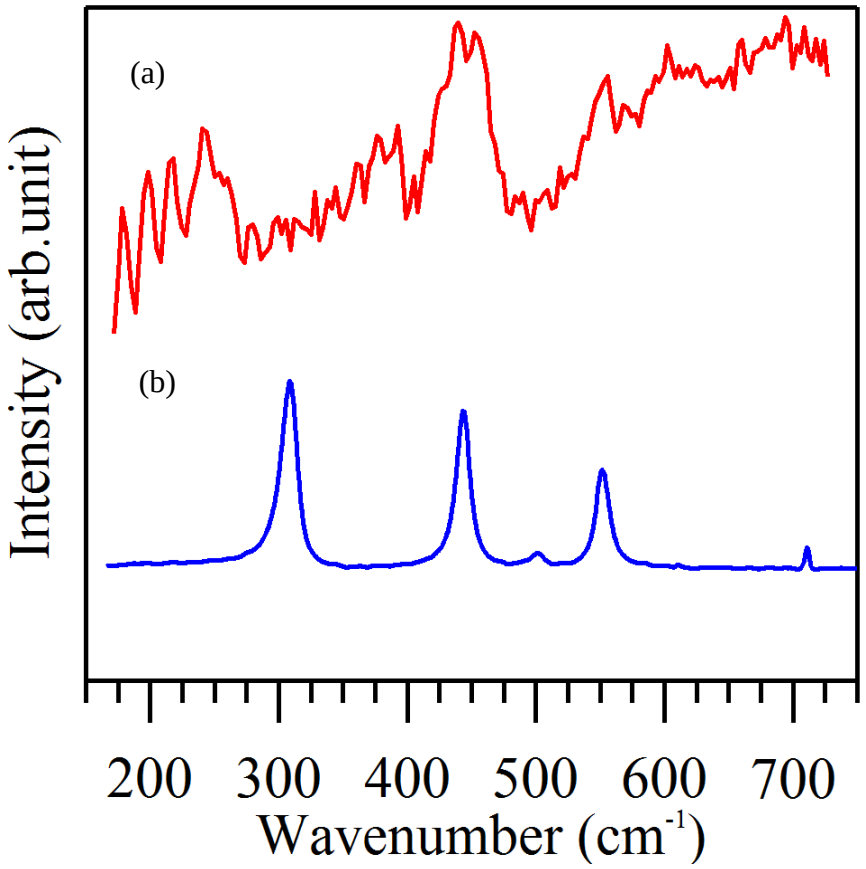

Fig.4.6.4 Raman spectra of (a) $CaIrO_3$ perovskite and (b) $CaIrO_3$ post-perovskite

Raman spectra reveal that the five prominent Raman modes for $CaIr_{0.5}Pt_{0.5}O_3$ post-perovskite phase show positive pressure dependence: 1.6 to 4.3 (cm^{-1}/GPa) (Fig.4.6.5, Table 4.6.1). According to group theory, there are 12 Raman-active modes out of 30 phonon modes. Thus, 5 out of 12 Raman-active modes were observed for each of the pressures in our study. The number of modes and their frequency are similar to the previously reported $CaIrO_3$ high-pressure Raman spectra by Hustoft et al.(2008)[38], apart from the newly observed Raman mode near 700cm^{-1}, which was in fact detectable in our study for $CaIr_{1-x}Pt_xO_3$ series (x =0, 0.3, 0.5, 0.7) by adopting the appropriate orientation of grains.

The Ir and Pt atoms do not participate in the Raman-active phonon modes due to atomic site symmetry (: 4a), while post-perovskite structure has 4 structural degree of freedom out of 12 atomic coordinates.

High pressure Raman spectroscopy studies on $CaIr_{0.5}Pt_{0.5}O_3$ reveal that the seven prominent Raman modes for the perovskite phase show positive pressure dependence: 1.0 to 2.8 (cm^{-1}/GPa) (Fig.4.6.6, Table 4.6.2). However, the fifth Raman mode (ν_5) of the perovskite phase does not follow this trend. The anomalous pressure dependence of this Raman mode around 28 GPa implies a possible second-order phase transition. It is worthwhile to note that when the Raman modes of the perovskite phase of $CaIr_{0.5}Pt_{0.5}O_3$ are extrapolated to ambient pressure, they show similarity to those of orthorhombic $GdFeO_3$-type perovskites such as $CaMnO_3$ perovskite (Abrashev et al.,2002)[64] in *Pbnm* space group. This is consistent with the known *Pbnm* symmetry of the $CaIrO_3$ perovskite[13]. As detailed mode assignment has been reported on $CaMnO_3$[64], I can assign the Raman modes of the new perovskite phase of $CaIr_{0.5}Pt_{0.5}O_3$ (Table 4.6.2). The perovskite phase of $CaIr_{0.5}Pt_{0.5}O_3$ is likely to be in the orthorhombic regime with a $GdFeO_3$-type structure (space group: *Pbnm*) having its octahedra less distorted and tilted compared to that of $CaIrO_3$ perovskite, presumably since the presence of Pt^{4+} suppresses the Jahn-Teller effect of Ir^{4+} in orthorhombic perovskite.

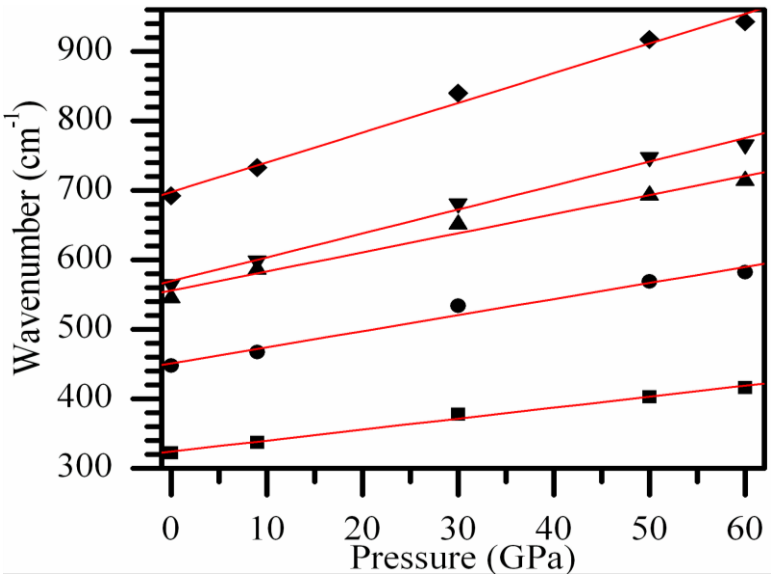

Fig.4.6.5 Pressure dependence of the five primary Raman modes of $CaIr_{0.5}Pt_{0.5}O_3$ post-perovskite (ν_1: ■ , ν_2: ● , ν_3: ▲ , ν_4: ▼ , ν_5: ◆)

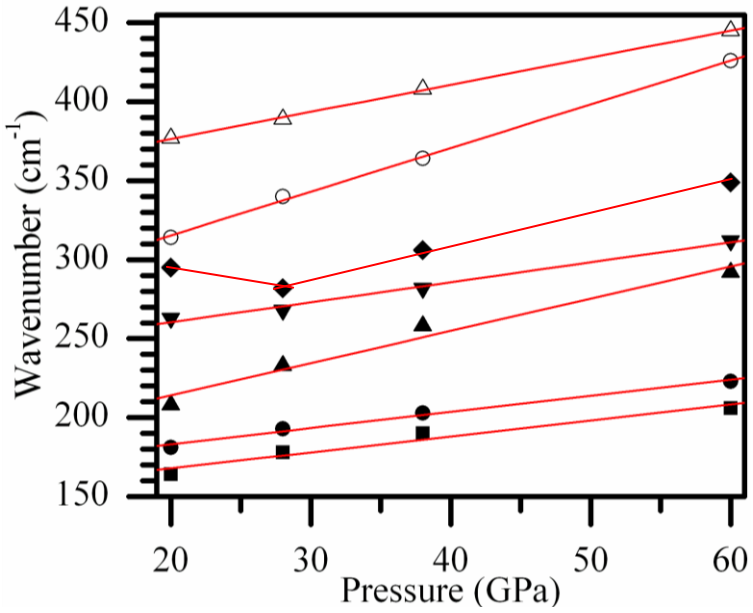

Fig.4.6.6 Pressure dependence of the seven primary Raman modes of $CaIr_{0.5}Pt_{0.5}O_3$ perovskite (ν_1: ■ , ν_2: ● , ν_3: ▲ , ν_4: ▼ , ν_5: ◆ , ν_6: ○ , ν_7: △)

It is useful to consider changes in Raman modes in both structures in terms of the Grüneisen parameter: γ. The Grüneisen parameter describes the effect that changing volume of a lattice has on vibrational properties, and can be used to tell us how thermodynamic properties affect the lattice dynamics and volume. This parameter is of considerable importance to Earth Scientists because it sets limitations on the thermoelastic properties of the Earth's deep interior. The mode Grüneisen parameter ($\gamma_{i,0}$) of each Raman mode is defined by the equation:

$$\gamma_{i,0} = K_{T0}/\nu_{i,0} * (d\nu_i / dP)$$

where $\gamma_{i,0}$ is the mode Grüneisen parameter, K_{T0} is the bulk modulus at ambient temperature and $\nu_{i,0}$ is the wavenumber of the ν_i Raman mode at ambient pressure. As the values of bulk modulus at ambient pressure for the post-perovskite phase of $CaIrO_3$[33](K_0: 180.2(28) GPa) and $CaPtO_3$[39] (K_0: 174.0(5) GPa) calculated by in-situ X-ray diffraction studies are very close to each other, it is reasonable to assume that the bulk modulus of the post-perovskite phase of $CaIr_{0.5}Pt_{0.5}O_3$ is an average of these two values, i.e. K_0: 177.1 GPa. Table 4.6.1 shows the mode Grüneisen parameters ($\gamma_{i,0}$) of the post-perovskite phase of $CaIr_{0.5}Pt_{0.5}O_3$, which can be calculated from estimated bulk modulus at ambient conditions. Calculated mode Grüneisen parameters ($\gamma_{i,0}$) vary from 0.869 to 1.10, and $<\gamma_{i,0}>$ is 0.971 (Table 4.6.1), showing similar values and distribution with those of $MgGeO_3$ (Shim et al., 2007)[65], where ($\gamma_{i,0}$) vary from 0.76 to 1.35. $CaIr_{0.5}Pt_{0.5}O_3$ has much smaller value and less variation of mode Grüneisen parameters compared with those of $CaIrO_3$[38]. Here I introduce the weighted average of mode Grüneisen parameters: $[\gamma_{i,0}]$ by the Einstein

heat capacity: $C_{i,0}$, since it is well known (Chopelas et al., 1994)[66] that the weighted average of mode Grüneisen parameters by the Einstein heat capacity is in good match with the thermodynamic Grüneisen parameter γ_{th}.

$$[\gamma_{i,0}] = \Sigma C_{i,0}\,\gamma_{i,0} / \Sigma C_{i,0}\ ; \quad C_{i,0} = y_{i,0}^2 \exp(y_{i,0}) / \{1-\exp(y_{i,0})\}^2\ ; \quad y_{i,0} = h\nu_{i,0}/k_B T_{i,0}$$

where h is Planck's constant, k_B is Boltzmann's constant and $T_{i,0}$ = 300 K.

The weighted average of mode Grüneisen parameters $[\gamma_{i,\ 0}]$ for $CaIr_{0.5}Pt_{0.5}O_3$ post-perovskite is 0.952 (Table 4.6.1), which is much smaller than the case of $CaIrO_3$ post-perovskite ($[\gamma_{i,\ 0}]$: 1.66), while it has a similar value to the case of $MgGeO_3$ post-perovskite ($[\gamma_{i,\ 0}]$: 1.15). Thus, the weighted average of mode Grüneisen parameters implies that γ_{th} ~0.952 for $CaIr_{0.5}Pt_{0.5}O_3$ post-perovskite. Such results suggest that $CaIr_{0.5}Pt_{0.5}O_3$ is a better analogue of the post-perovskite phase of $MgSiO_3$ than $CaIrO_3$ as the triply degenerate ground state of low spin $5d^5$ Ir^{4+} is replaced by non-degenerate $5d^6$ Pt^{4+}. In addition, its estimated bulk modulus K_0: 177.1 GPa has a similar value to that of $MgSiO_3$[67] (K_0: 231 GPa) and $MgGeO_3$ [68] (K_0: 205 GPa).

The experimentally derived bulk modulus at ambient pressure for perovskite phase of $CaIrO_3$ is K_0: 198(3) GPa. As a first order approximation, it can be assumed that the extrapolated ambient pressure bulk modulus of the perovskite phase of $CaIr_{0.5}Pt_{0.5}O_3$ is ~200 GPa. Then, the mode Grüneisen parameters $\gamma_{i,0}$ of the perovskite phase of $CaIr_{0.5}Pt_{0.5}O_3$ can be calculated as shown in Table 4.6.2. The mode Grüneisen parameters $\gamma_{i,0}$ vary from 0.912 to 1.96 and the simple average $<\gamma_{i,\ 0}>$ is 1.29, showing similar values

and distribution to those of $MgGeO_3$[65] perovskite, where $\gamma_{i,0}$ varies from 1.04 to 2.10. As the weighted average of mode Grüneisen parameters is $[\gamma_{i,0}]$: 1.27, it can be estimated that γ_{th} ~1.27 for $CaIr_{0.5}Pt_{0.5}O_3$ perovskite. Therefore, the thermodynamic Grüneisen parameter increases by 34 % across the post-perovskite to perovskite phase transition in $CaIr_{0.5}Pt_{0.5}O_3$. A similar magnitude of increase in γ_{th} is reported for $(Mg,Fe)SiO_3$[69] (27 %) and $MgGeO_3$[65] (33 %), showing that the proportional change in γ_{th} is insensitive to the very different masses of the cations in $CaIr_{0.5}Pt_{0.5}O_3$ compared to $(Mg,Fe)SiO_3$. In addition, the perovskite phase of $CaIr_{0.5}Pt_{0.5}O_3$ has the same number of prominent Raman modes as $MgGeO_3$[65] perovskite. As such, $CaIr_{0.5}Pt_{0.5}O_3$ is a promising analogue for the system $MgSiO_3$ in the lowermost mantle. The parameter q was not calculated since the pressure dependence of Raman modes of the perovskite phase of $CaIr_{0.5}Pt_{0.5}O_3$ were close to linear, having similar features with the $MgGeO_3$[65] perovskite. It would be useful to conduct $CaIrO_3$ perovskite high-pressure Raman studies for comparison, but this is extremely difficult since the Raman peaks are very noisy due to its metallic[13] feature.

The second mode Grüneisen parameters ($q_{i,0}$) are the logarithmic volume derivatives of the mode Grüneisen parameters ($\gamma_{i,0}$), as defined by the equation:

$$q_{i,0} = \gamma_{i,0} - K^2_{T0}/\nu_{i,0}\gamma_{i,0}*(d^2\nu_i/dP^2)$$

The second mode Grüneisen parameters ($q_{i,0}$) were calculated for $CaIr_{0.5}Pt_{0.5}O_3$ post-perovskite in order to compare it with that of $MgGeO_3$ [61]. The parameter $q_{i,0}$ varied from 2.86 to 3.93, showing similar values to those of $MgGeO_3$[61] perovskite, where $q_{i,0}$ varies from 1.18 to 4.58. The second mode Grüneisen parameters ($q_{i,0}$) of $CaIr_{0.5}Pt_{0.5}O_3$

perovskite was not calculated since its Raman-active modes showed near-perfect linearity of pressure dependence.

The newly synthesized phase at 60GPa, ~1900K for $CaIr_{0.5}Pt_{0.5}O_3$ has Raman modes which resemble those of $CaIrO_3$ perovskite and $CaHfO_3$ perovskite, suggesting this phase has a perovskite structure. However, this perovskite phase transformed back into a post-perovskite phase when the pressure was released down to ~9GPa. According to previous studies on phase transition from post-perovskite to perovskite in $CaIrO_3$ (Kojitani et al., 2007)[37], the phase equilibrium boundary is calculated to be P (GPa) = 0.040 T(K) – 67.1. Thus, the phase equilibrium boundary condition for $CaIrO_3$ at T = 1900K is predicted to be P = 8.9 GPa from the strongly positive P/T slope. Therefore, assuming the gradient of the P/T slope is uniform over the $CaIr_{1-x}Pt_xO_3$ series, the phase diagram of $CaIr_{0.5}Pt_{0.5}O_3$ can be drawn as Fig.4.6.7 (P.102). The theoretical phase boundary between post-perovskite and perovskite phase for $CaPtO_3$ is estimated to be ~111GPa for ~1900K and ~87GPa for ~1300K, by extrapolating the P/T phase boundary for $CaIrO_3$ (8.9GPa, 1900K) and $CaIr_{0.5}Pt_{0.5}O_3$ (60GPa, 1900K) as in Fig.4.6.7. Taking such estimations into consideration, the observation that $CaPtO_3$ did not transform into perovskite phase at 7GPa and ~1300K (Inaguma et al., 2007)[70] suggests the lack of sufficient pressure to stabilise the perovskite structure. Even though the phase transition from post-perovskite to perovskite may take place at extremely high pressures (above 80GPa), it is likely that the perovskite phase reverts back to post-perovskite structure at lower pressures during decompression. In other words, the instability of the perovskite phase of $CaPtO_3$ is revealed by the destabilization of newly synthesized perovskite phase of $CaIr_{0.5}Pt_{0.5}O_3$.

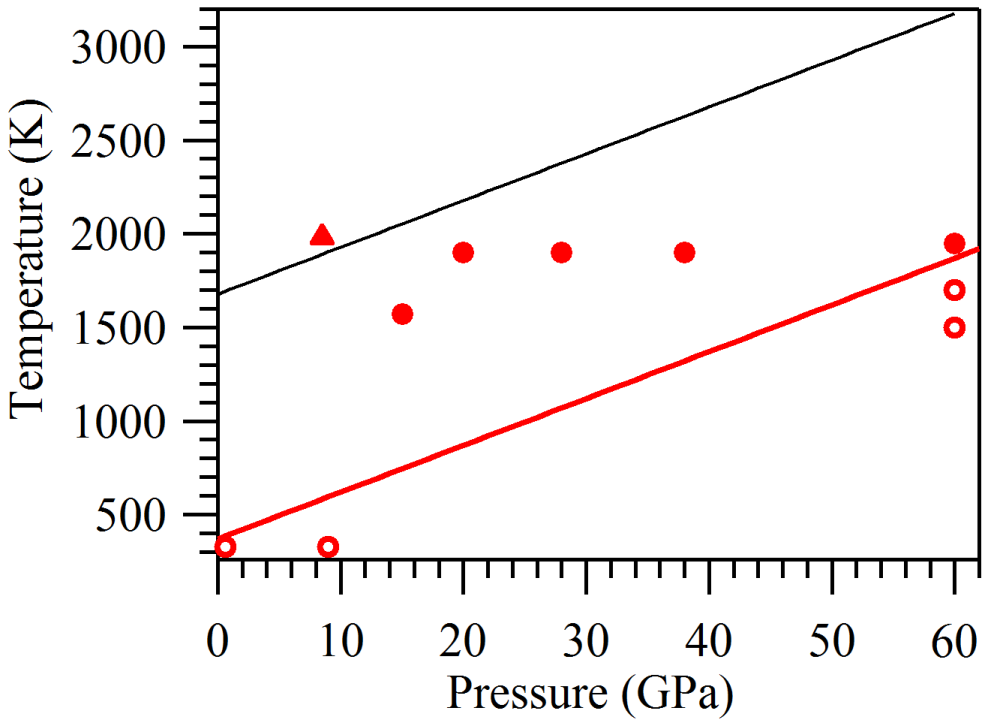

Fig.4.6.7 Phase diagram of $CaIr_{0.5}Pt_{0.5}O_3$ estimated on the basis of the sample synthesised at or quenched to various pressure/temperature conditions, along with the phase boundary of $CaIrO_3$ as a guide ($CaIr_{0.5}Pt_{0.5}O_3$ post-perovskite: ○, $CaIr_{0.5}Pt_{0.5}O_3$ perovskite: ●, $CaIrO_3$ perovskite: ▲). The phase boundary and the data point of $CaIrO_3$ were taken from Kojitani et al.(2007)[37]. The phases in the diagram were detected by high pressure/ambient pressure Raman spectroscopy for $CaIr_{0.5}Pt_{0.5}O_3$. The red line shows the phase boundary between the post-perovskite and perovskite phase for $CaIr_{0.5}Pt_{0.5}O_3$, and the black line shows the phase boundary between the post-perovskite and perovskite phase for $CaIrO_3$.

The instability of $CaIr_{0.5}Pt_{0.5}O_3$ perovskite at pressures below 9 GPa can be explained in terms of the activation energy barrier between the perovskite phase and the post-perovskite phase. As $CaIrO_3$ perovskite is a metastable phase (Sarkozy et al., 1974) [13] at ambient pressure, the activation energy for adopting the post-perovskite phase is high for $CaIrO_3$. Thus, $CaIrO_3$ perovskite synthesised at high pressures can be quenched to ambient pressure. On the other hand, if the activation energy barrier of $CaIr_{0.5}Pt_{0.5}O_3$ is much lower compared to $CaIrO_3$, the metastable perovskite phase can easily transform to the stable post-perovskite phase. Therefore, $CaIr_{0.5}Pt_{0.5}O_3$ perovskite at pressures below 9 GPa cannot play the role of a metastable phase anymore due to the low energy barrier, which suggest that further studies for determining the energy minima of both perovskite and post-perovskite phase, such as the first principles calculation, is of great importance.

The conflict between strong Pt-O covalent bonding which favours large octahedral tilting, and the Jahn-Teller inactive Pt^{4+} in the perovskite structure which favours cubic perovskite is one possible reason for destabilization of the perovskite-structure in the Pt-Ir solid solution series. A similar destabilization mechanism of perovskite- vs ilmenite-structure has been previously reported in the case of $NaSbO_3$-type oxides (Mizoguchi et al, 2004)[71]. Although conflict between strong Pt-O covalent bonding and the Jahn-Teller inactive Pt^{4+} destabilise the perovskite-structure, pressure and the replacement of Pt-O by Ir-O bonding can play a role in stabilising the perovskite structure. In the case of $CaIrO_3$, $CaRhO_3$ and $CaRuO_3$, this conflict does not exist since the B-site cation (Ir^{4+}: $5d^5$, Rh^{4+}: $4d^5$, Ru^{4+}: $4d^4$) in each compound is Jahn-Teller active. This is the reason why the post-perovskite to peovskite phase transition has not been observed for

$CaPtO_3$ unlike the case for $CaIrO_3$, $CaRhO_3$ and $CaRuO_3$. The stability condition of post-perovskite/perovskite regime is very sensitive since Ir^{4+} and Pt^{4+} in $CaMO_3$ (M = Ir/Pt) have similar ionic radii (Ir^{4+}: 0.625, Pt^{4+}: 0.625) and similar electronegativity (χ_{Ir}: 2.2, χ_{Pt}: 2.28). The strong Pt-O covalent bonding that stabilizes the post-perovskite regime comes from the high electronegativity of Pt. The post-perovskite phase of $CaIrO_3$, $CaPtO_3$, $CaRhO_3$ and $CaRuO_3$ can be quenched to ambient pressure since the electronegativities of Ir, Pt, Rh and Ru are 2.20, 2.28, 2.28 and 2.20, while those of Si, Ge, Al, Fe and Mn are 1.90, 2.01, 1.61, 1.83 and 1.55, respectively. Therefore, $MgSiO_3$[1], $MgGeO_3$[61], Al_2O_3[44], Fe_2O_3 [7] and Mn_2O_3 [8] can adopt post-perovskite structure at high pressures, but when the compression of bonds due to high confining pressure is removed, the strong M-O covalent bonding (M = Si/Ge/Al/Fe/Mn) disappears and they can no longer sustain the post-perovskite structure.

4.7 Conclusions

The grains in $CaIrO_3$ and $CaIr_{1-x}Pt_xO_3$ (x = 0.3, 0.5, 0.7) show needle-like to elongate morphology. Mean grain size of $CaIrO_3$ and $CaIr_{1-x}Pt_xO_3$ (x = 0.3, 0.5, 0.7) varies between samples from 1 μm to 8 μm. Grain size of the needles varies with maxima at the end-member and at 0.5 compositions suggesting that the minimum melting point in the $CaIr_{1-x}Pt_xO_3$ series is near x = 0.5.

The new phase synthesized at 60GPa, 1900K for $CaIr_{0.5}Pt_{0.5}O_3$ has Raman modes which resemble those of $CaIrO_3$ perovskite, suggesting this phase adopts a perovskite structure. The instability of the perovskite phase of $CaIr_{0.5}Pt_{0.5}O_3$ reveals why the post-perovskite to perovskite phase transition has not been observed for $CaPtO_3$ unlike the case for $CaIrO_3$, $CaRhO_3$ and $CaRuO_3$. High pressure Raman spectroscopy studies on $CaIr_{0.5}Pt_{0.5}O_3$ reveal that the five primary Raman modes for post-perovskite phase and seven primary Raman modes for perovskite phase show positive pressure dependence. The anomalous pressure dependence of fifth Raman mode (ν_5) around 28 GPa implies a possible second-order phase transition. The increase in γ_{th} across the post-perovskite to perovskite transition was estimated as 34 %, which is in similar magnitude with $(Mg,Fe)SiO_3$ and $MgGeO_3$, suggesting that $CaIr_{0.5}Pt_{0.5}O_3$ is a promising analogue for investigating $MgSiO_3$ system in the lowermost mantle.

5. Structural properties of $CaIr_{1-x}Pt_xO_3$

5.1 Rietveld refinement of the structure of $CaIr_{1-x}Pt_xO_3$

Powder X-ray diffraction was used to determine the atomic structure of Ir-Pt post-perovskite solid solutions. Measurements were performed using a Bruker D8 advanced diffractometer with incident CuKα radiation (λ = 1.5406Å). X-ray profiles were collected in the range of $16^o < 2\theta < 120^o$ with the step size of 0.013755^o and scanning time of 10s. Each powdered sample was placed on a glass plate surface which minimizes background diffraction. Each sample with texture was sieved onto a surface of a greased glass plate. The whole refinement process was done by the refinement software, *GSAS* (Larson et al., 2000)[72] using the least squares method, by minimizing the peak intensity misfit, $\sum w(Io - Ic)^2$ (*w*: statistical weight of I_c, which is $1/\sigma(I_c)^2$, I_o: observed diffraction intensity, I_c: calculated diffraction intensity). In order to fit a series of observed diffraction intensities from the X-ray profile, theoretical diffraction intensities were calculated in the following form, taking all possible contributors into account:

$I_c = s \sum L \mid F_c \mid^2 \varphi(\theta) P A + I_{bg}$ (s: scale factor, L: Lorentz and polarization factors, F_c: calculated structure factor, φ(θ): Gaussian function for fitting the peak shape, P: orientation density function describing the sample texture, A: absorption correction due to the sample surface roughness, I_{bg}: background diffraction intensity from the glass plate and the grease). Previously known cell parameters and crystal data of the $CaIrO_3$ single crystal (Hirai et al., 2009) [16] were used as a starting structure for X-ray refinements, and contributors of the

calculated diffraction intensities were refined in the following order. First, the atomic positions and isotropic thermal parameters of Ca, Ir, O1 and O2 were fixed, and the lattice constants were refined with the instrumental zero position until they converged. Secondly, the lattice constants and the instrumental zero position was fixed and the atomic positions and the 2^{nd} order absorption coefficient were refined until they converged. 2^{nd} order absorption coefficient was refined since the surface roughness effect on the intensity reduction for $CaIrO_3$ cannot be ignored due to its nature as a big absorber. Thirdly, the lattice constants and the atomic positions were fixed and the isotropic thermal parameters (U_{iso}) and absorption coefficient were refined until they converged. Then, the atomic positions, the isotropic thermal parameters and the absorption coefficient were refined. Finally, the lattice constants, the atomic positions, the isotropic thermal parameters, the absorption coefficient and the Gaussian constants which describe the X-ray diffraction peak shape were refined together. In this way, refinement with small R_p-factor and R_{wp}-factor was accomplished, where $R_p = \sum |Io - Ic| / \sum Io$, $R_{wp}^2 = \sum w(Io - Ic)^2 / \sum wIo^2$. As proof of a good refinement, χ^2 values ($\chi^2 = \sum w(Io - Ic)^2 /$ N; N: the number of diffraction data points) close to 1 were obtained for $CaIr_{1-x}Pt_xO_3$ series.

5.2 Refined lattice parameters of $CaIr_{1-x}Pt_xO_3$ and their evolution

Rietveld fitted X-ray diffraction patterns (Fig. 5.2.1) demonstrate that the recovered $CaIr_{1-x}Pt_xO_3$ (x = 0, 0.3, 0.5, 0.7) samples contain post-perovskites with traces of secondary phases in some cases. All of the major X-ray diffraction peaks were indexed by the $CaIrO_3$-type cell with orthorhombic space group *Cmcm*.

Initial Rietveld fits to the X-ray diffraction profiles showed that strong textures were present in the loosely packed powders and so another pattern was collected from each sample sieved onto a greased surface to minimise this effect. Large differences between the two patterns for each sample are evident in Fig. 5.2.1. Fits to the greased samples were used to refine the crystal structure parameters, giving the results shown in Table 5.2.1.

Fig.5.2.1: Fitted powder X-ray diffraction profiles of $CaIr_{1-x}Pt_xO_3$ for (a) x = 0, (b) x = 0.3, (c) x = 0.5 and (d) x = 0.7, showing considerable texture effects.

(upper/lower panels are from greased/ungreased holders with powdered samples, respectively. The green curve denotes the calculated X-ray diffraction intensity of each sample, the red curve denotes the experimental X-ray diffraction intensity of each sample, the pink curve denotes the mismatch between experimental and calculated X-ray diffraction intensity, and the black sign denotes the calculated Bragg peak positions of each sample)

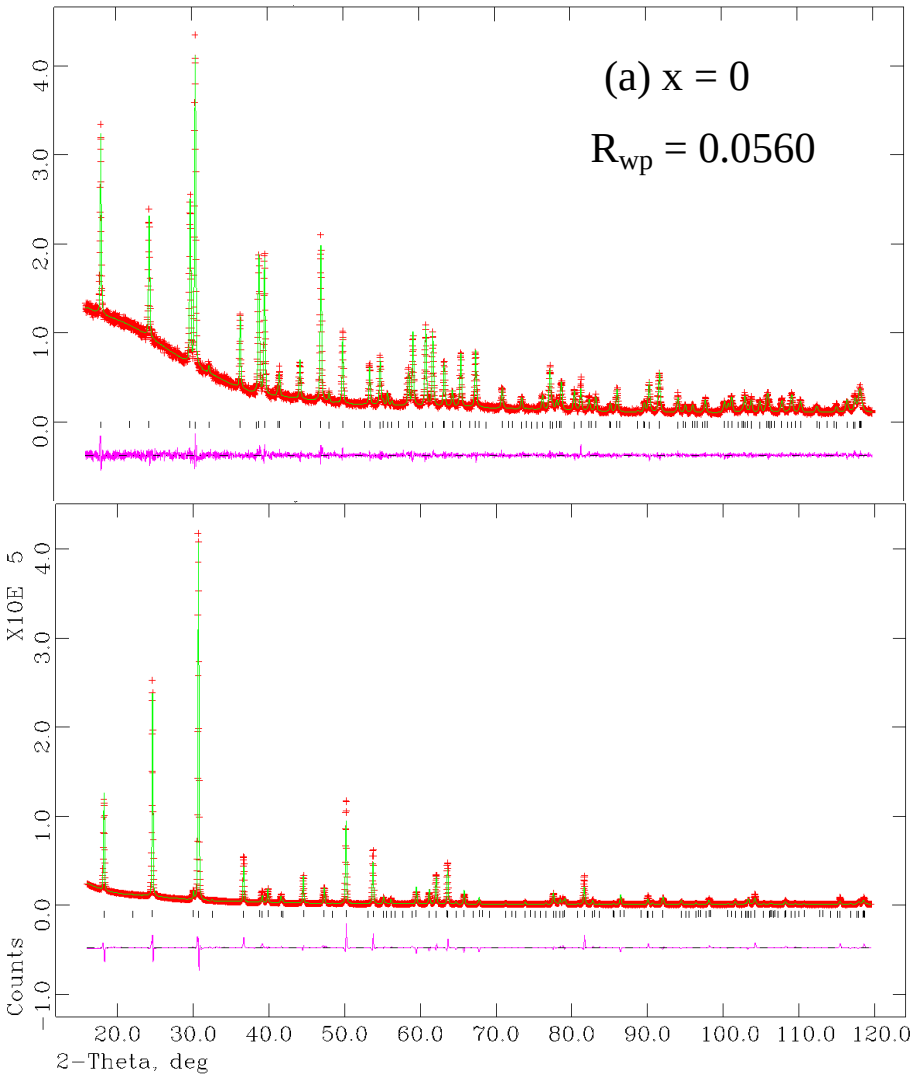
(a) x = 0
R_{wp} = 0.0560
X10E 5
Counts
2−Theta, deg

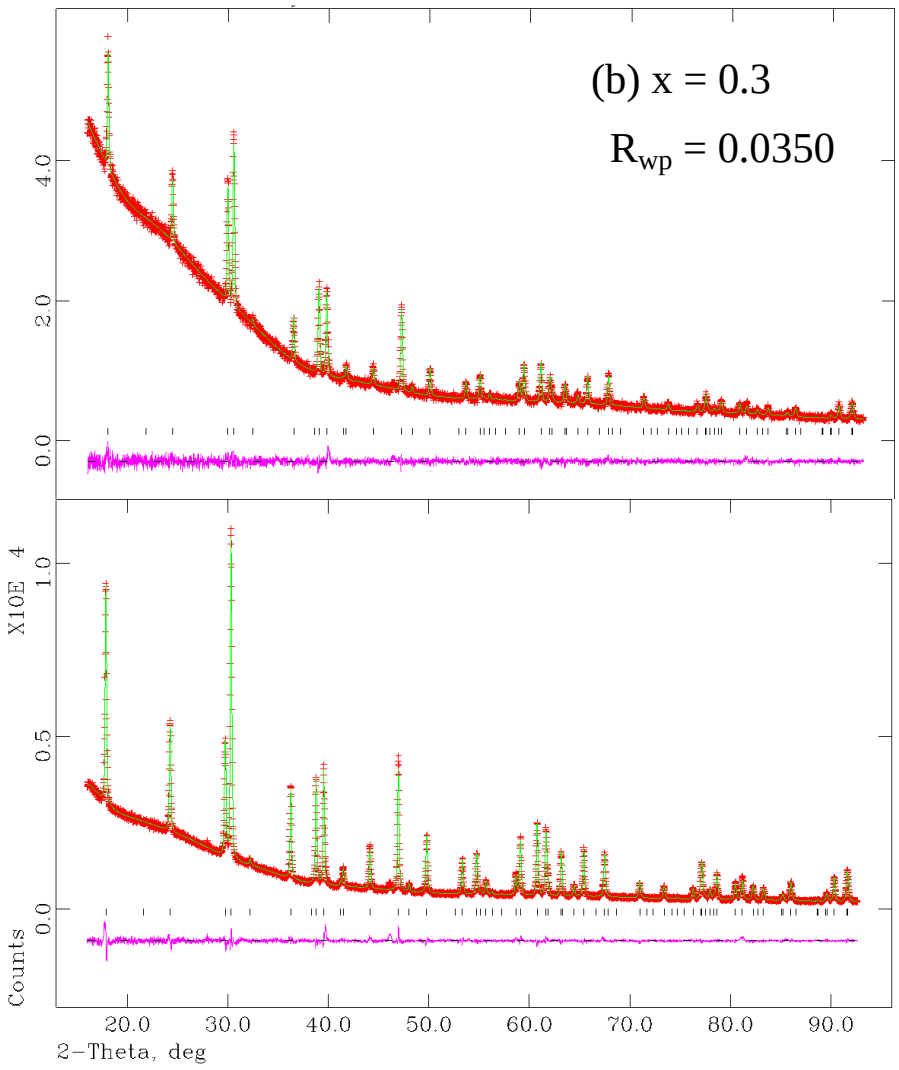
(b) x = 0.3
R_{wp} = 0.0350
4.0
2.0
0.0
X10E 4
1.0
0.5
0.0
Counts
20.0
30.0
40.0
50.0
60.0
70.0
80.0
90.0
2−Theta, deg

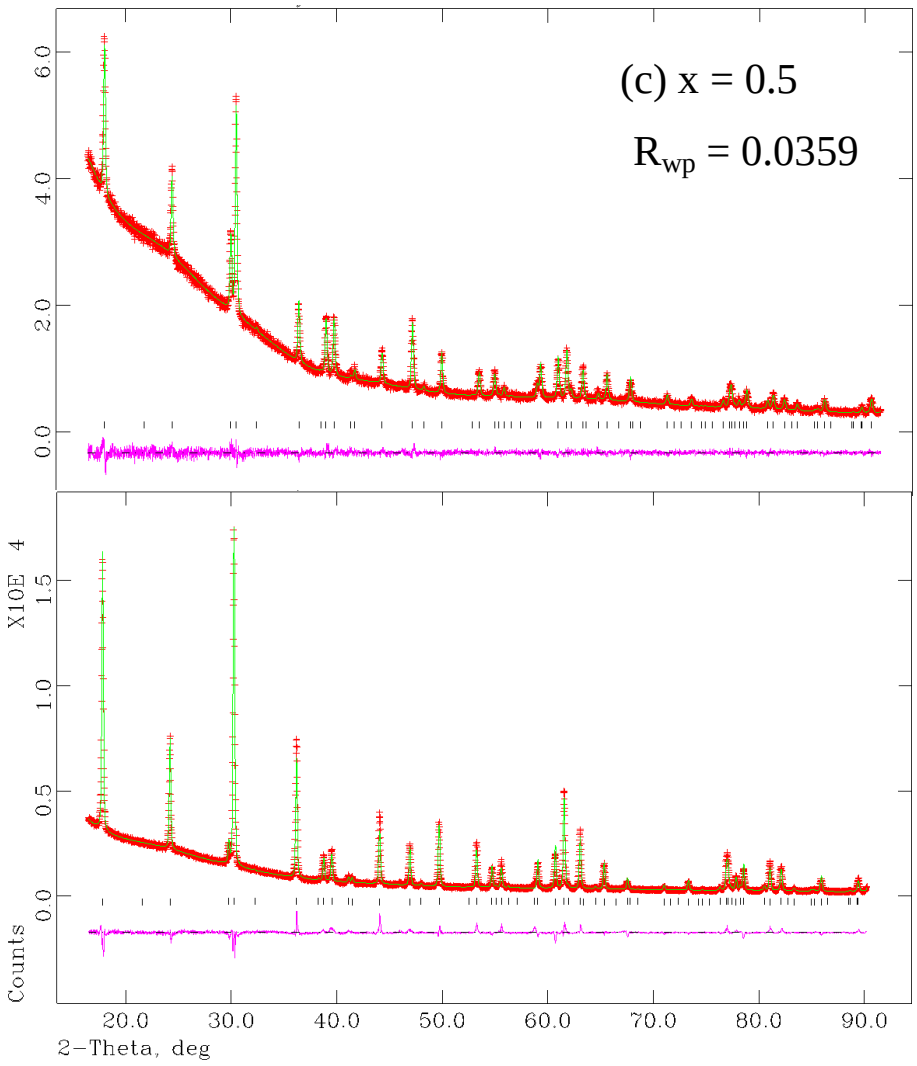
(c) x = 0.5
R_{wp} = 0.0359
X10E 4
Counts
2-Theta, deg

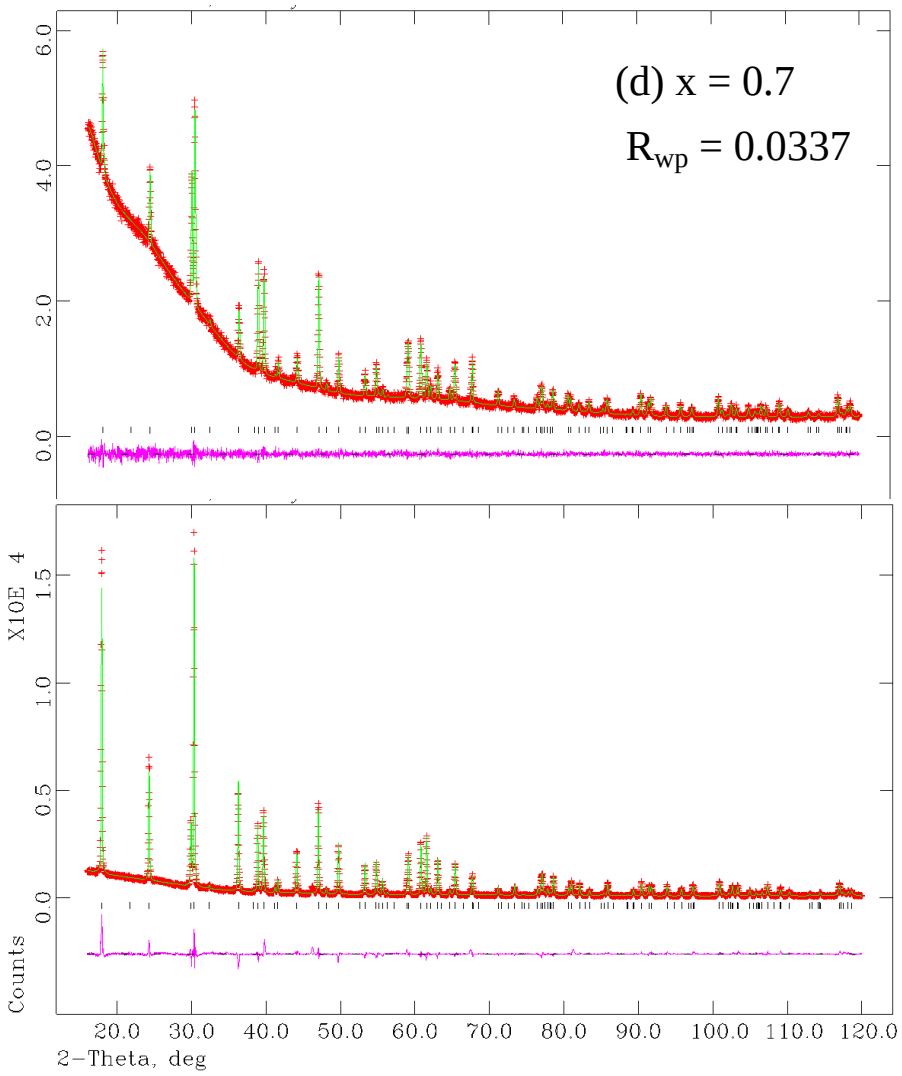
(d) x = 0.7
R_{wp} = 0.0337
6.0
4.0
2.0
0.0
X10E 4
1.5
1.0
0.5
0.0
Counts
20.0
30.0
40.0
50.0
60.0
70.0
80.0
90.0
100.0
110.0
120.0
2−Theta, deg

Table 5.2.1: Crystallographic results* for $CaIr_{1-x}Pt_xO_3$

Compounds	$CaIrO_3$	$CaIr_{0.7}Pt_{0.3}O_3$	$CaIr_{0.5}Pt_{0.5}O_3$	$CaIr_{0.3}Pt_{0.7}O_3$
a (Å)	3.14592(4)	3.14114(7)	3.13575(7)	3.13216(4)
b (Å)	9.8635(1)	9.8795(2)	9.8924(1)	9.9051(1)
c (Å)	7.29903(9)	7.3081(1)	7.3169(1)	7.3303(1)
V ($Å^3$)	226.489(6)	226.795(12)	226.973(9)	227.420(7)
R_{wp}	0.0560	0.0350	0.0359	0.0337
χ^2	1.17	1.17	1.20	1.08
Ca: y	0.2503(3)	0.2474(6)	0.2510(5)	0.2500(4)
O1: y	0.425(1)	0.439(2)	0.429(2)	0.421(1)
O2: y	0.1320(8)	0.127(1)	0.128(1)	0.1291(8)
O2: z	0.4455(9)	0.451(2)	0.449(1)	0.450(1)
U_{iso} of Ir ($Å^2$)	0.0024(5)	0.0131(6)	0.0009(5)	0.0037(6)
M-O1 (Å)	1.967(5) x2	1.923(5) x2	1.957(7) x2	1.993(5) x2
M-O2 (Å)	2.081(5) x4	2.041(7) x4	2.053(7) x4	2.055(6) x4
<M-O> (Å)	2.041(5)	1.999(6)	2.019(7)	2.032(6)
M-O1 valence	0.77(1)	0.87(1)	0.80(2)	0.73(1)
M-O2 valence	0.56(1)	0.63(1)	0.62(1)	0.62(1)
BVS(Ir)	3.78(6)	4.26(6)	4.08(8)	3.94(6)
M-O1-M (°)	136.1(7)	143.7(9)	138(1)	133.7(7)
M-O2-M (°)	98.2(3)	100.6(5)	99.6(4)	99.3(4)
O1-M-O2(°)	93.3(3)	91.3(4)	92.8(5)	94.5(3)
O2-M-O2(°)	98.2(3)	100.6(5)	99.6(4)	99.3(4)

*Atomic positions; Ca: 4c (0, y, 1/4), M = Ir/Pt: 4a (0, 0, 0), O1: 4c (0,y,1/4), O2: 8f (0, y, z); bond valences of M-O bonds were calculated as $\exp((R_i-R_0)/B)$ with R_0 values of 1.870 (Ir^{4+}-O^{2-}), 1.879 (Pt^{4+}-O^{2-})

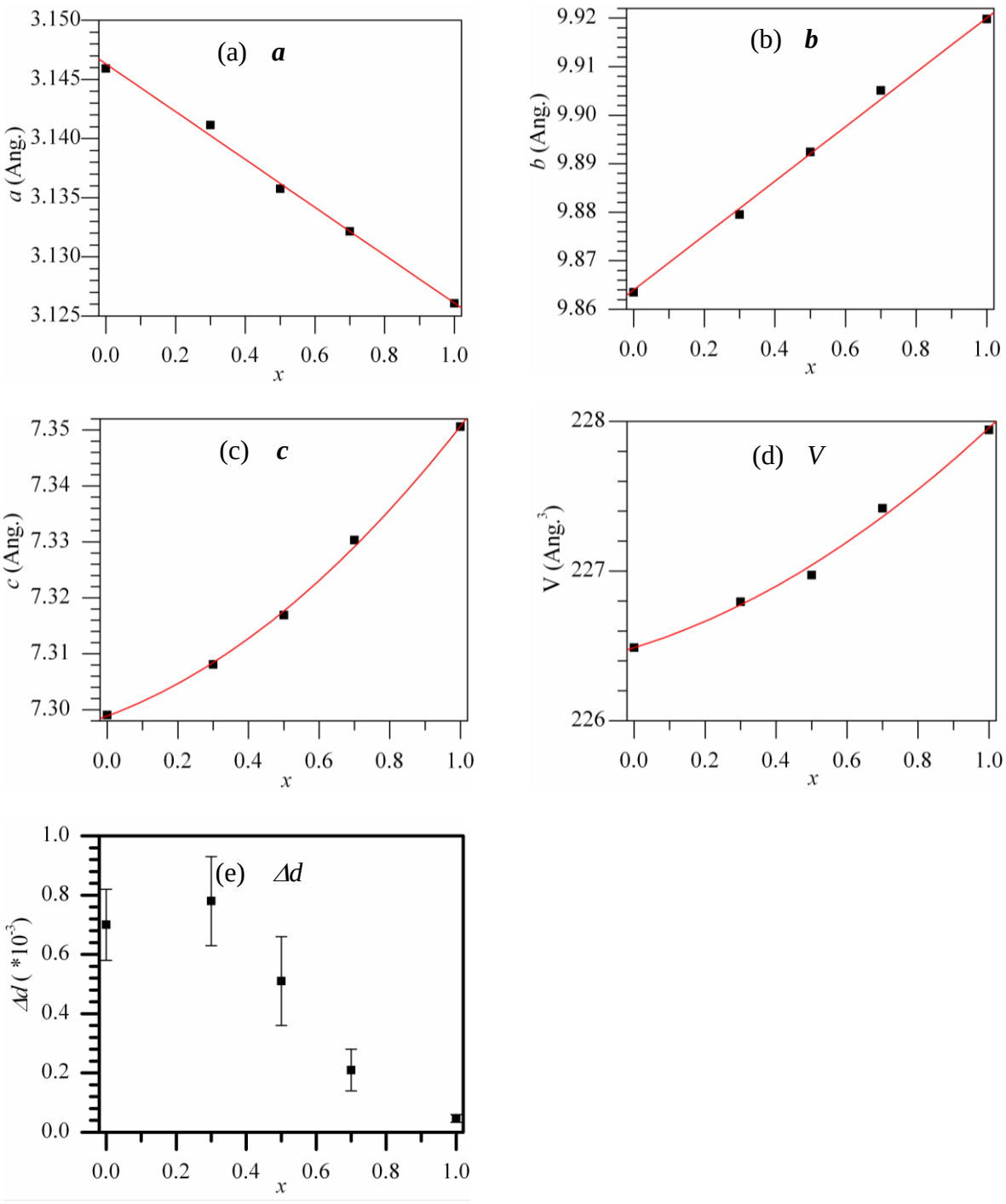

Fig. 5.2.2: Evolution of the orthorhombic lattice parameters (a) *a*, (b) *b*, (c) *c*, and (d) unit cell volume (*V*) and octahedral distortion parameter: delta *d*, as defined on P.121 for $CaIr_{1-x}Pt_xO_3$ solid solutions. The fitted curves are guides to the eye.

The variation of lattice parameters with composition in the $CaIr_{1-x}Pt_xO_3$ series is shown in Fig. 5.2.2, taking results for $CaPtO_3$ [17] from a previously reported paper. It is notable that the *a*- and *b*-axis lengths change linearly with composition, whereas variation in the *c*-axis is non-linear and lies below the values expected by linear interpolation between the end-members for $0 < x < 1$. This leads to the same trend in the cell volume. This suggests local ordering of Ir/Pt in the *c*-direction, most likely due to the strong covalent nature of the post-perovskite structure along *a*-axis (Fig.5.2.3) which disfavours the disruption of Ir^{4+}-Ir^{4+} metal-metal bonding and as a consequence, Ir/Pt is enforced to order along *c*-axis (Ir^{4+}- Pt^{4+} - Ir^{4+}-…..).

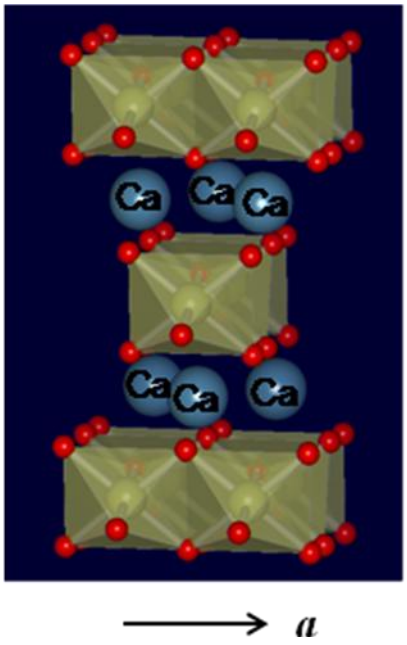

Fig.5.2.3 Edge shared octahedra along *a*-axis possess Ir^{4+}-Ir^{4+} metal-metal bonding for $CaIr_{1-x}Pt_xO_3$

A recent DFT study of $CaRhO_3$ (Matar et al., 2010)[73] suggested that metal-metal bonding in the chains of edge-shared octahedra along the *a*-axis, as found in the rutile types RuO_2[74], IrO_2[75] and ReO_2[76] also plays a role in stabilizing the post-perovskite regime. This may account for the ambient pressure stability of $CaIrO_3$, which has a formal Ir^{4+}-Ir^{4+} bond order of one, in comparison to $CaPtO_3$ for which the Pt^{4+}-Pt^{4+} bond order is zero. Therefore, the Ir/Pt ordering along with the increase of Pt composition is likely to come from the need to sustain metal –metal bonding for Ir^{4+}-Ir^{4+}. This is the cause of parabolic increase instead of linear increase for the *c*-axis lattice constant.

The refined bond distances can be evaluated using bond valence theory (Brown et al., 2002)[77], which states that the sum of the valence of all the bonds formed around a cation or an anion should be equal to the formal valence of the cation or anion. In the refined crystal structure of $CaIrO_3$, Ir^{4+} is surrounded by six O^{2-} ions and Ca^{2+} is surrounded by eight O^{2-} ions. Therefore the sum of the valence of six Ir-O bonds should be close to 4, and the sum of the valence of eight Ca-O bonds should be close to 2. Bond valence theory [77] states that the valence of a bond can be calculated by the following equation:

$$S_{ij} = \exp\{(R_0 - R_{ij})/B\} \qquad (5.2.1)$$

(R_0: constant for a particular atom pair, R_{ij}: bond distance between cation i and anion j, B: universal constant equal to 0.37 Å)

The bond valence of Ir-O and Ca-O bonds calculated from the refined bond distances are shown in Table.5.2.2.

Table.5.2.2 Bond valence of Ca-O and M-O (M = Ir/Pt) bonds for $CaIr_{1-x}Pt_xO_3$ series (x = 0, 0.3, 0.5, 0.7), bond valences were calculated from $\exp((R_i - R_0)/B)$ with R_0 values of 1.967 (Ca^{2+}-O^{2-}), 1.870 (Ir^{4+}-O^{2-}) and1.879 (Pt^{4+}-O^{2-})[77]

(Ca-O2'denotes the longer Ca-O2 bond and BVS denotes Bond Valence Sum)

Compounds	$CaIrO_3$	$CaIr_{0.7}Pt_{0.3}O_3$	$CaIr_{0.5}Pt_{0.5}O_3$	$CaIr_{0.3}Pt_{0.7}O_3$
Ca-O1 (Å)	2.341(11) x2	2.424(14) x2	2.378(16) x2	2.306(11) x2
Ca-O2 (Å)	2.420(6) x4	2.482(10) x4	2.448(8) x4	2.455(7) x4
Ca-O2' (Å)	2.510(7) x2	2.493(12) x2	2.516(11) x2	2.507(8) x2
Ca-O1 valence	0.36(1)	0.29(1)	0.33(1)	0.40(1)
Ca-O2 valence	0.29(1)	0.25(1)	0.27(1)	0.27(1)
Ca-O2' valence	0.23(1)	0.24(1)	0.23(1)	0.23(1)
BVS of Ca	2.34(8)	2.06(8)	2.20(8)	2.34(8)
M-O1 (Å)	1.967(5) x2	1.923(5) x2	1.957(7) x2	1.993(5) x2
M-O2 (Å)	2.081(5) x4	2.041(7) x4	2.053(7) x4	2.055(6) x4
M-O1 valence	0.77(1)	0.87(1)	0.80(2)	0.73(1)
M-O2 valence	0.56(1)	0.63(1)	0.62(1)	0.62(1)
BVS of Ir/Pt	3.78(6)	4.26(6)	4.08(8)	3.94(6)

The bond valence sum of Ir-O bonds makes 3.72-4.32vu (Table 5.2.2.), which is in good agreement with the formal valence of Ir^{4+}. The bond valence sum of Ca-O bonds makes 1.98-2.42vu (Table 5.2.2.), which is close enough to the formal valence of Ca^{2+}, suggesting the Rietveld refinement was successful. However, the difference is more than 10 % of the formal valence, so a considerable strain exists in the $Ca\text{-}O_8$ polyhedra (F.ig.5.2.4). In other words, Ca-O bonds are over bonded. Such over bonding of Ca-O is likely to come from the anisotropic octahedral network of post-perovskite structure. Thus, in order to avoid structural instability coming from excessive over bonding of Ca-O, the M-site cation in $CaMO_3$ post-perovskite is restricted to be rigid. In fact, the quenchable post-perovskite oxides ($CaIrO_3$, $CaPtO_3$, $CaRhO_3$, $CaRuO_3$) share this feature having M-cation with heavy mass and small U_{iso}. Ca (χ = 1.00) has higher electronegativity compared with Sr (χ = 0.95) and Ba (χ = 0.89). Thus, Ca will allow over bonding with oxygen in a broader range than Sr and Ba. This may well be the reason why no post-perovskite oxide with Sr/Ba is reported to exist.

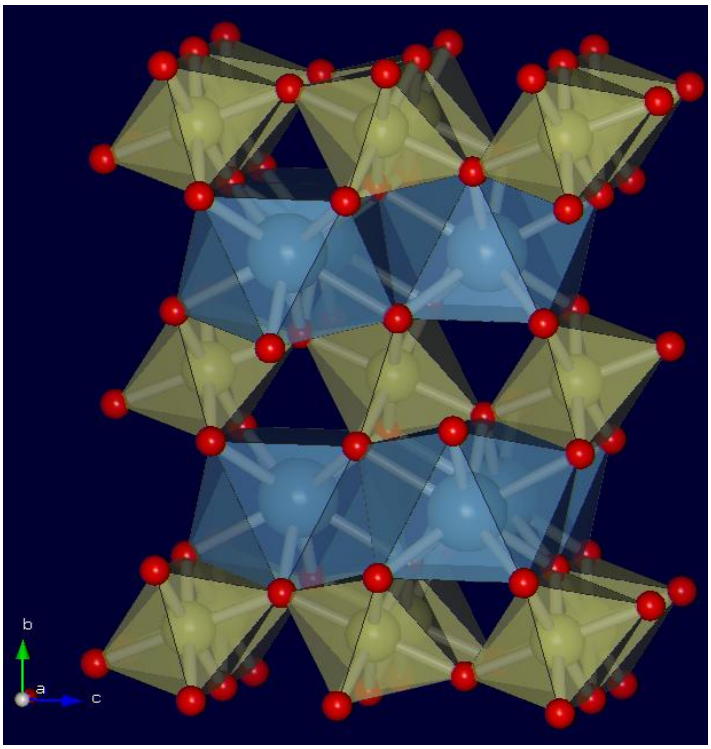

Fig.5.2.4 CaO_8 polyhedra (in blue) and MO_6 octahedra (M = Ir/Pt) (in gold) of $CaIr_{1-x}Pt_xO_3$ series with post-perovskite structure, illustrating the polyhedra where Bond Valence Sum (BVS) and structural strain were calculated

Secondly, the U_{iso} of M-cation in AMO_3 post-perovskite can be evaluated. This evaluation is important because the U_{iso} values have never been compared as a function of composition along a post-perovskite solid solution. Table 5.2.1 shows that the U_{iso} of Ir is less than $0.01(Å^2)$ over the $CaIr_{1-x}Pt_xO_3$ series. This may well come from the heavy atomic weight of Ir, which restricts the atomic displacement. Also, the bonding within $CaIr_{1-x}Pt_xO_3$ series is rigid due to the high electronegativity of Ir, permitting the U_{iso} of Ir/Pt to remain small. Therefore, such small U_{iso} values are reasonable.

The theoretical bond valence values can be determined from the BVT[77](Brown et al., 2002), which states that the sum of the valence of all the bonds formed around a cation or anion should be equal to the formal valence of the cation or anion, and the sum of the closed loop will become 0[77]. Therefore, the empirical network equations can be derived as follows, where A, B, C and D are Ir-O1, Ir-O2, Ca-O1 and Ca-O2 bond valences, respectively.

O1: $2A+2C=2$ (5.2.2)

O2: $2B+3D=2$ (5.2.3)

Ir: $2A+4B=4$ (5.2.4)

Ca: $2C+6D=2$ (5.2.5)

Loop equation: $A-C+D-B=0$ (5.2.6)

The bond valences derived by solving the equations above are A = 0.71, B = 0.65, C = 0.29, D = 0.24. The theoretical bond valences agree to a good extent with those experimentally obtained from the refined data (Table.5.2.2). In spite of the Ca-O2 bond distances being divided into two different groups due to the deviation of M-O2-M angle from 90 degrees, the gap is much smaller than that between Ca-O1 and Ca-O2. Therefore, the bond distance differences experimentally found are satisfactorily reproduced within this model. The MO_6 octahedra have two short M-O1 bonds and four long M-O2 bonds. The Jahn-Teller effect of Ir^{4+} cannot explain this octahedral distortion since MO_6 should have two long bonds and 4 short bonds in that case. Instead, the observed MO_6 distortion is in good agreement with the

crystallographic requirements of post-perovskite structure. Bond valences for M-O1 and M-O2 are calculated to be 0.71 and 0.65, respectively, suggesting strong covalent bonding of M-O. In other words, M-O1 is predicted to be shorter than M-O2, and undistorted MO_6 octahedra cannot be realized in post-perovskite structure, as opposed to the perovskite structure. For example, the theoretical M-O1 and M-O2 bond distances calculated from the theoretical bond valence for $CaIr_{0.3}Pt_{0.7}O_3$ are 2.003 Å and 2.036 Å, which is in reasonable agreement with the experimental bond distances, 1.993(5) Å and 2.055(6) Å. Therefore, the octahedral distortion in $CaIr_{1-x}Pt_xO_3$ series simply arises from strong covalent bonding of M-O1. The main reason that post-perovskite oxides stable at ambient conditions are only found when M (: transition metal) of MO_6 octahedra is 4d or 5d transition metals is because of the strong covalent bonding along crystallographic *c*-axis (when M = M^{4+} and M^{3+}, the theoretical bond valence of M-O1 is 0.71 and 0.56, respectively) required in terms of crystal structure, which requires high electronegativity of M. The electronegativity of Ir, Pt, Rh and Ru are 2.20, 2.28, 2.28 and 2.20, respectively, while that of Mn is 1.55. Therefore, Mn_2O_3 [8] can take the post-perovskite structure at high pressure, but when compression of bonds due to high confining pressures is removed, the strong M-O covalent bonding disappears and it can no longer sustain the post-perovskite structure. As the average of O-M-O angle remains constant over the $CaIr_{1-x}Pt_xO_3$ series (Table.5.2.1), M-O1 and M-O2 bond distances are the only indicators for the evolution of MO_6 octahedral distortion. I will parameterize the MO_6 (M = Ir/Pt) octahedral distortion in post-perovskite structure using $\Delta d = 1/6\{2(R_1 - \langle R\rangle)^2 + 4(R_2 - \langle R\rangle)^2\}/\langle R\rangle^2$ (R_1: M-O1 bond distance, R_2: M-O2 bond distance, <R>: average of M-O bond distances), which has

been introduced for perovskite oxides in previous studies (Alonso et al., 2000)[78]. Fig.5.2.2(e) shows that the MO_6 octahedral distortion is weakened by the increasing Pt substitution. This can be explained in terms of crystal field theory. Pt^{4+} ($5d^6$) has a larger crystal field than Ir^{4+} ($5d^5$), so Pt^{4+} opposes octahedral distortion to a larger extent than Ir^{4+}, which drives MO_6 (M = Ir/Pt) octahedra to become more regular with increasing Pt content. On the other hand, there is no correlation between composition in the $CaIr_{1-x}Pt_xO_3$ series and M-O1-M angle, which lies in the range of 134-144˚ and shows no systematic trend with composition. Non-correlation between octahedral distortion and M-O1-M appears to be mainly a consequence of crystallographic requirement of post-perovskite structure which does not allow undistorted MO_6 octahedra. It is worthwhile considering the difference between the calculated bond valence sum and the formal valence which arises from the distortion of the polyhedra from the ideal structure. This distortion can be explained in terms of bond valence theory, which states that if the average bond distance of the polyhedra is too long, the polyhedra will distort in such a way as to increase some bond distances and decrease other bond distances in order to increase the bond valence sum (Brown et al., 1992)[79]. As the coordination number of polyhedra increases, the bond valence of each bond will decrease, resulting in an increase in average bond distance. The bond valence sum around Ca^{2+} is large enough to cause a strong strain in the CaO_8 polyhedra, while the bond valence sum around M^{4+} (M = Ir/Pt) is not large enough to causing a strong strain in the MO_6 octahedra. Nevertheless, an interesting relationship between Ca-O and M-O bonds can be obtained for this structure by the cancellation of C from equations (5.2.2) and (5.2.5), which leads to A = 3D. This equation establishes the

Ca-O2/M-O1 valence ratio must be close to 3 for the ideal unstrained structure. The bond valence of the averaged Ca-O2 bond distances satisfies this equation very well over the $CaIr_{1-x}Pt_xO_3$ series (Table 5.2.3), where the discrepancy is 0.03 - 0.13 v.u. being within the range of statistical error.

Table 5.2.3 Comparison of the average of Ca-O2 bond valence (:D) with M-O1 (M = Ir/Pt) bond valence (:A) for $CaIr_{1-x}Pt_xO_3$ series (x = 0, 0.3, 0.5, 0.7) in order to examine the relationship: A =3D derived from Bond Valence Sums

Compounds	$CaIrO_3$	$CaIr_{0.7}Pt_{0.3}O_3$	$CaIr_{0.5}Pt_{0.5}O_3$	$CaIr_{0.3}Pt_{0.7}O_3$
<Ca-O2 valence> x3 (v.u.)	0.82(3)	0.74(6)	0.77(3)	0.77(3)
M-O1 valence (v.u.)	0.77(1)	0.87(1)	0.80(2)	0.73(1)

In order to describe structural strain, two different parameters are introduced : the *Bond Strain Index* (BSI) (Preiser et al., 1999)[80] and the *Global Instability Index* (GII) (Salinas-Sanchez et al., 1992)[81]. The former is calculated as the difference between the observed and the theoretical bond valences from the network equations:

$$BSI = \sqrt{\langle (S-s)^2 \rangle} \qquad (5.2.7)$$

where S and s are the experimental and theoretical bond valences, respectively. The average is taken over all bonds in the formula unit. If the value of BSI is larger than 0.1 in a certain compound, its structure is electronically strained [77]. On the other hand, this measure of the strain can be complemented with the factor GII, which represents the average difference between the formal valence and the BVS, through:

$$GII = \sqrt{\left\langle \left(\sum_j S_{ij} - V_i \right)^2 \right\rangle} \qquad (5.2.8)$$

In this case the average is over all the atoms in the formula unit. The standard values of GII vary from 0.05 v.u. to 0.20 v.u.[78], for compounds in the stability limit. The BSI is typically smaller than GII for compounds with lattice-induced strains, while the opposite holds for electronic induced strains (especially for those induced by Jahn-Teller effect).

Table 5.2.4 GII[77] and BSI[78] describing the structural strain in the post-perovskite structure for $CaIr_{1-x}Pt_xO_3$ series (x = 0, 0.3, 0.5, 0.7, 1), where the values of $CaPtO_3$[17] are derived from Ohgushi et al.(2008)

Compounds	$CaIrO_3$	$CaIr_{0.7}Pt_{0.3}O_3$	$CaIr_{0.5}Pt_{0.5}O_3$	$CaIr_{0.3}Pt_{0.7}O_3$	$CaPtO_3$ [17]
GII (v.u.)	0.248	0.219	0.178	0.215	0.220
BSI (v.u.)	0.065	0.064	0.046	0.047	0.045

Unusually large differences between GII and BSI are observed for the $CaIr_{1-x}Pt_xO_3$ series (Table 5.2.4). The values of BSI vary from 0.05 to 0.07 systematically over the series indicating weak electronic strain in Ir-rich compounds, while the values of GII vary from 0.18 to 0.25 over the series clearly suggesting lattice-induced instability associated with the post-perovskite regime. Therefore, structural strain in $CaIr_{1-x}Pt_xO_3$ series comes from lattice-induced strains instead of electronic induced strains. In other words, the comparison of GII with BSI demonstrates that anisotropic connectivity of the post-perovskite structure is dominant against the weak Jahn-Teller effect for $CaIr_{1-x}Pt_xO_3$ series. Moreover, the large values of GII for the $CaIr_{1-x}Pt_xO_3$ series indicate lattice-induced strain in the structure is only partially relaxed by varying the bond length of Ca-O2. The outstanding lattice-induced strain in $CaIrO_3$ among $CaIr_{1-x}Pt_xO_3$ series could explain the sensitive polymorphism found at room conditions in powder samples between the perovskite and post-perovskite phases.

5.3 Texture analysis of $CaIr_{1-x}Pt_xO_3$ and their evolution

To obtain morphological information from the XRD patterns of ungreased loosely packed powders of the $CaIr_{1-x}Pt_xO_3$ series, the crystal structure parameters were fixed at the values obtained from the greased samples, and the intensities were Rietveld-fitted by varying the nine ODF (Orientation Density Function) coefficients that describe a cylindrical symmetry sample texture up to 6^{th} order (Von Dreele et al., 1997)[82]. A cylindrical symmetry was chosen since $CaIr_{1-x}Pt_xO_3$ series generally adopt and elongated to needle-like morphology (Chapter 4). Refinements with other orders of ODF were tried before choosing

the 6^{th} order ODF as the most favourable ODF for the post-perovskite system. Along with the increase of the order of ODF starting from 2^{nd} order (increase of the number of refined parameters), refinements kept on converging with better X-ray profile fitting up to 6^{th} order, while the refinement over 6^{th} order gave stable goodness of fit with no additional information of orientation density for the crystallites. Such observation justifies that the refinement using 6^{th} order ODF is sufficient for texture analysis and that it gives the best available fit for the peak intensities as shown in Fig. 5.2.1. The orientation densities derived from the refined ODF parameters are shown in Fig. 5.3, which show the density of crystallites with plane (hkl) at an angle ψ to the sample plane, relative to the average (untextured) value of 1.0. In all samples the maximum density for (100) is at ψ = 90°, confirming that the crystallographic *a*-axis is parallel to the long dimension of the needle-like crystals. Maximum (010) and (001) densities are, consequently, both at ψ= 0 but a systematic change from (001) to (010) density is observed as x increases from x = 0 to 0.7. This shows that Pt substitution favours (001) over (010) growth. The magnitudes of the orientation density maxima in the $CaIr_{1-x}Pt_xO_3$ series correlate well with the grain sizes observed by SEM. The large grain $CaIrO_3$ and $CaIr_{0.5}Pt_{0.5}O_3$ show maximum densities of near 3, whereas the smaller-grained $CaIr_{0.7}Pt_{0.3}O_3$ and $CaIr_{0.3}Pt_{0.7}O_3$ have density maxima of 1.4 and 2.1 respectively.

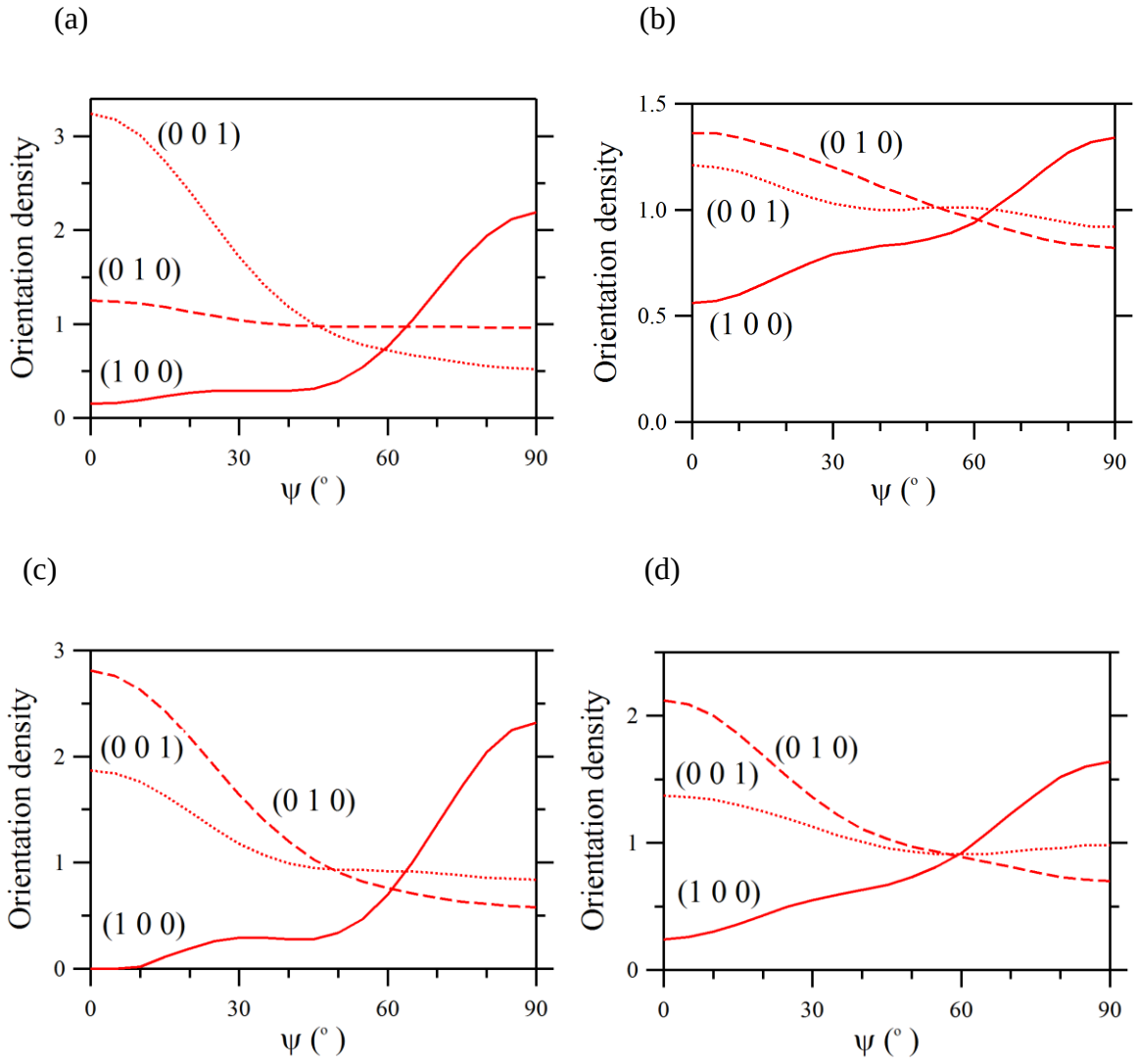

Fig. 5.3: Angular dependence of crystallite orientation density of $CaIr_{1-x}Pt_xO_3$ for (a) x = 0, (b) x = 0.3, (c) x = 0.5 and (d) x = 0.7

5.4 Conclusions

Powder X-ray diffraction based structure refinement for each of the $CaIr_{1-x}Pt_xO_3$ (x = 0, 0.3, 0.5, 0.7) series was performed successfully by using the software program *GSAS* [63]. The crystal structures of $CaIr_{1-x}Pt_xO_3$ (x = 0, 0.3, 0.5, 0.7) series were determined as orthorhombic layered structures in the space group of *Cmcm*. Both the lattice constants and the bond distances are in good agreement with the post-perovskite structure. The MO_6 octahedra (M = Ir/Pt) share their edges in the *a*-axis direction, and share their corners in the *c*-axis direction, and Ca exists in the interlayer region between the layers of octahedral networks. Bond distances were checked by bond valence theory, which represents the crystallographic requirement of post-perovskite regime.

Structural properties of polycrystalline samples of $CaIr_{1-x}Pt_xO_3$ (x = 0.3, 0.5, 0.7) were revealed for the first time. The *a*- and *b*-axis lengths change linearly with composition, whereas the *c*-axis shows curvature and lies below the values expected between the end-members, implying local ordering of Ir/Pt in the *c*-direction. This Ir/Pt local ordering is likely to arise from the need to sustain metal –metal boning for Ir^{4+}-Ir^{4+}. By introducing ODF texture analysis, solid solutions of $CaIrO_3$ and $CaPtO_3$ were found to exhibit similar grain growth feature with the mother compound, apart from the fact that Pt substitution favours (001) over (010) growth.

6. Physical properties of $CaIr_{1-x}Pt_xO_3$

6.1 Magnetic properties of $CaIr_{1-x}Pt_xO_3$

Magnetic properties of Pt-Ir solid solution post-perovskites were measured using a Quantum Design MPMS SQUID magnetometer. Samples were packed in a gelatine capsule (filled with nonmagnetic cotton) and placed in the middle of a plastic straw before inserting into the SQUID. Zero field- and field-cooled (ZFC and FC) measurements were made with a field of 100 Oe after cooling the sample down to 5 K.

Fig.6.1.1 shows the temperature dependence of molar magnetic susceptibility for the four samples of $CaIr_{1-x}Pt_xO_3$ series. The molar magnetic susceptibility was derived from the directly measured magnetic susceptibility using the following relationship:

$$\chi_d = \chi_m W_s / W_m$$

(χ_d (emu): directly measured magnetic susceptibility, χ_m (emu/mol): molar magnetic susceptibility, W_s (g): the sample weight, W_m (g): molecular weight of the sample)

Table 6.1: Magnetic parameters of $CaIr_{1-x}Pt_xO_3$ and $CaIr_{0.5}Rh_{0.5}O_3$

Compounds	$CaIrO_3$	$CaIr_{0.7}Pt_{0.3}O_3$	$CaIr_{0.5}Pt_{0.5}O_3$	$CaIr_{0.3}Pt_{0.7}O_3$
α (emu.mol^{-1})	0.00748(1)	0.00024(2)	0.00126(1)	0.00043(1)
θ (K)	-	37(11)	87(7)	39(8)
C (emu.K.mol^{-1})	-	0.053(9)	0.02(1)	0.031(7)
μ_{eff} (μ_B/f.u.)	-	0.7(3)	0.4(3)	0.5(2)
T_c (K)	108	20	< 5	-

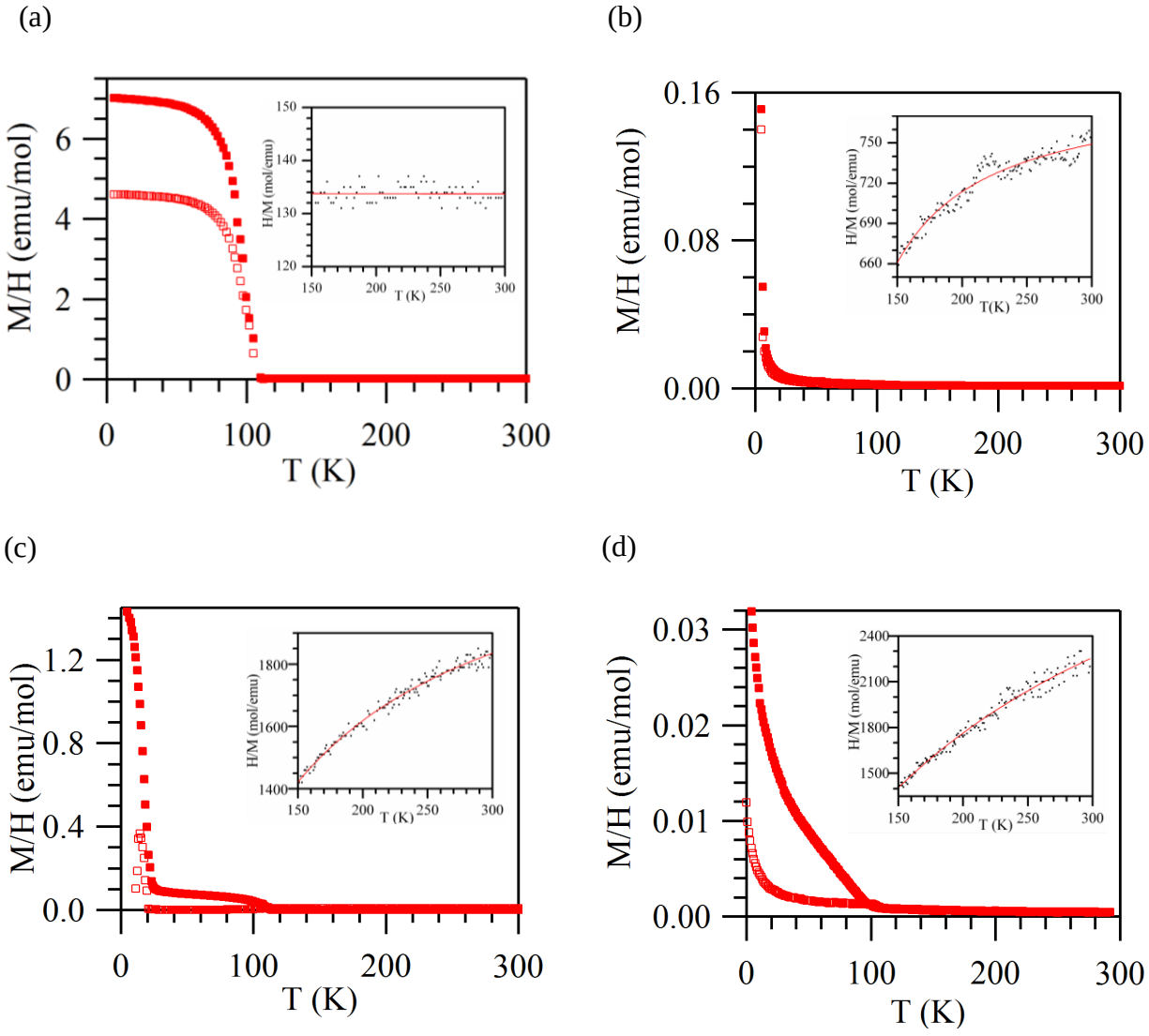

Fig.6.1.1 ZFC and FC (open and closed symbols in order) molar magnetic susceptibilities (M/H) of $CaIr_{1-x}Pt_xO_3$ for (a) x = 0, (b) x = 0.3, (c) x = 0.5 and (d) x = 0.7. Insets show fits to inverse susceptibilities between 150 and 300 K.

The transition marked by an upturn in magnetisation and divergence of zero-field and field cooled susceptibilities is observed at 108 K for $CaIrO_3$, which has a comparable value with previous studies (Ohgushi et al., 2006) [31]. This is suppressed to 20 K for x = 0.3

and to below 5 K for x = 0.5. The x = 0.7 sample shows an anomalous ~105 K transition, but this most probably arises a trace amount of $CaIrO_3$ resulting from some sample inhomogeneity, in view of the suppressed transition in $CaIr_{0.5}Pt_{0.5}O_3$ and the diamagnetic nature of $CaPtO_3$.

The inverse susceptibilities of the samples at 150-300 K are shown in the insets to Fig. 6.1.1. $CaIrO_3$ shows temperature-independent Pauli paramagnetism over this range but the other samples have non-linear susceptibilities. This Pauli-paramagnetic feature observed for $CaIrO_3$ above 150K (Fig.6.1.1(a)) implies that $CaIrO_3$ is a magnetic metal. The itinerancy of unpaired electron spin in Ir^{4+} and the weak on-site Coulomb interaction due to the extended 5d orbital are likely to be responsible for this metallic nature. The inverse susceptibilities of the samples at 150-300 K were fitted using the equation $1/\chi = [\alpha + C/T-\theta]^{-1}$ which includes Pauli and Curie-Weiss terms. The fitted curves are shown on Fig. 6.1.1 and the derived parameters are listed in Table 6.1. Although no clear trends in the parameters with x are evident, Pt doping clearly introduces local moments that follow Curie-Weiss behaviour with an effective paramagnetic moment of ~0.5 μ_B/formula unit and the positive Weiss constants imply ferromagnetic exchange interactions between spins. Ferromagnetic interactions for $CaIr_{1-x}Pt_xO_3$ (x = 0.3, 0.5, 0.7) is in good agreement with Kanamori-Goodenough's rule (Goodenough et al., 1960)[83] described in terms of cation-cation ordering, indicating that the direct ferromagnetic interaction of Ir^{4+}-Ir^{4+} in the crystallographic *a*-axis direction is dominant over the indirect antiferromagnetic interaction of Ir^{4+}-O^{2-}-Ir^{4+} in the crystallographic *c*-axis direction.

Magnetisation-field data for $CaIrO_3$ and $CaIr_{0.7}Pt_{0.3}O_3$ are shown in Fig.6.1.2.

Ferromagnetic hysteresis loops are observed for these materials. $CaIrO_3$ shows saturated magnetisation of 0.040 μ_B/formula unit. Such a small magnetic moment is a further indication that $CaIrO_3$ is a metal. In a nonmagnetic metal, equal numbers of spin-up and spin-down electrons exist in a spin fluctuated state in the d-band. In order to stabilise a metal in a ferromagnetic state, those spin-down electrons have to be shifted to spin-up state. If the electron density-of-states are not uniform in the d-band, this shift will stop in an intermediate state exhibiting weak itinerant ferromagnetism (Shimizu et al., 1981)[84] with small saturated magnetic moment (Moriya et al., 1979)[85]. Thus, saturated magnetisation of 0.040 μ_B/formula unit implies that $CaIrO_3$ is a weak itinerant ferromagnetic metal. The ferromagnetic hysteresis loop of Fig.6.1.2(a) shows that $CaIrO_3$ is an unusually hard magnetic oxide, with a large magnetic anisotropy and a coercive field of H_{ct} = 3.4T at 5K. The thermal evolution of the hysteresis loop of $CaIrO_3$ is shown in Fig. 6.1.3. The variation of the coercive field with temperature (Fig.6.1.4) was fitted with the equation: $H_c = 2\alpha K/M_s[1-(T/T_C)^{1/2}]$ (Nunes et al., 2004)[86] where α = 0.48, and the fitted uniaxial anisotropy constant is K = 1.77 x 10^6 J/m^3. This is comparable to the value of 5 x 10^6 J/m^3 for $Nd_2Fe_{14}B$ which is a widely used permanent magnetic material[87], [88]. The large crystal field and the strong spin-orbital coupling of Ir^{4+} ($5d^5$), as found in a recent study on Sr_2IrO_4 [40], and the anisotropic crystal structure of $CaIrO_3$ are all likely contributors to this exceptional high coercive field for a magnetic oxide. Substitution of 30% Pt for Ir dilutes the magnetic interactions and decreases the saturated magnetisation from 0.040 μ_B/formula unit for $CaIrO_3$ to 0.024 μ_B/formula unit, while the 5K coercive field drops from 3.4T for $CaIrO_3$ to 0.46T for $CaIr_{0.7}Pt_{0.3}O_3$.

(a)

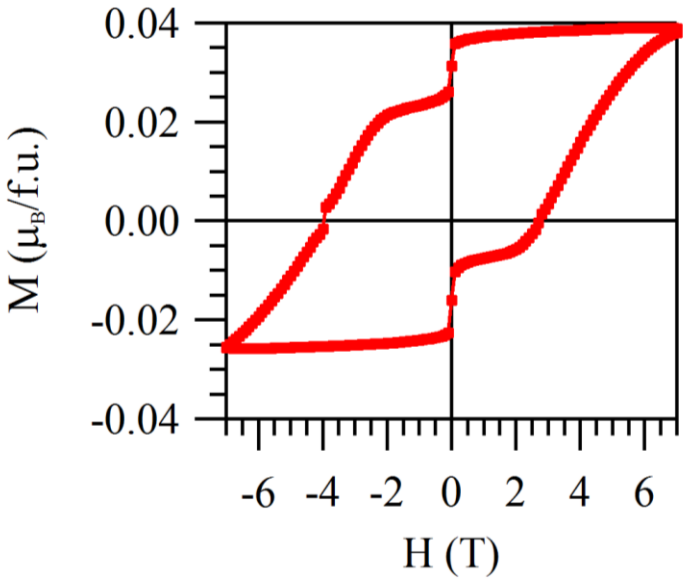

(b)

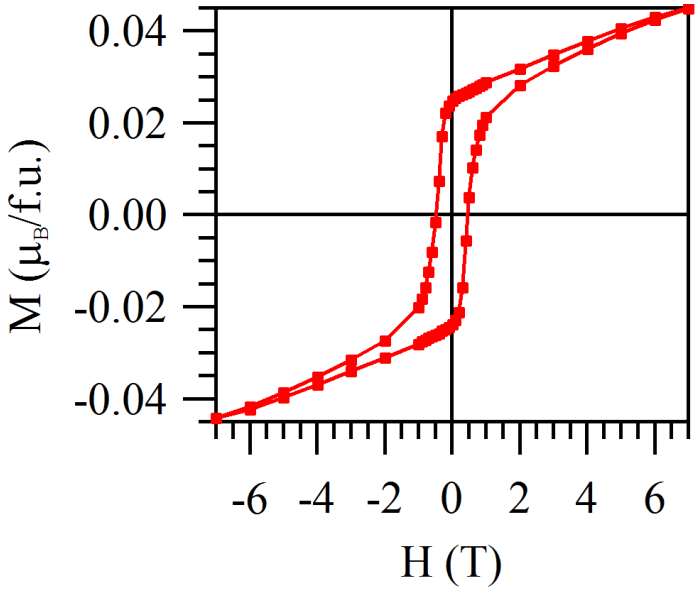

Fig.6.1.2 Magnetisation-field hysteresis loops at 5K for $CaIr_{1-x}Pt_xO_3$ for (a) x=0 and (b) x=0.3

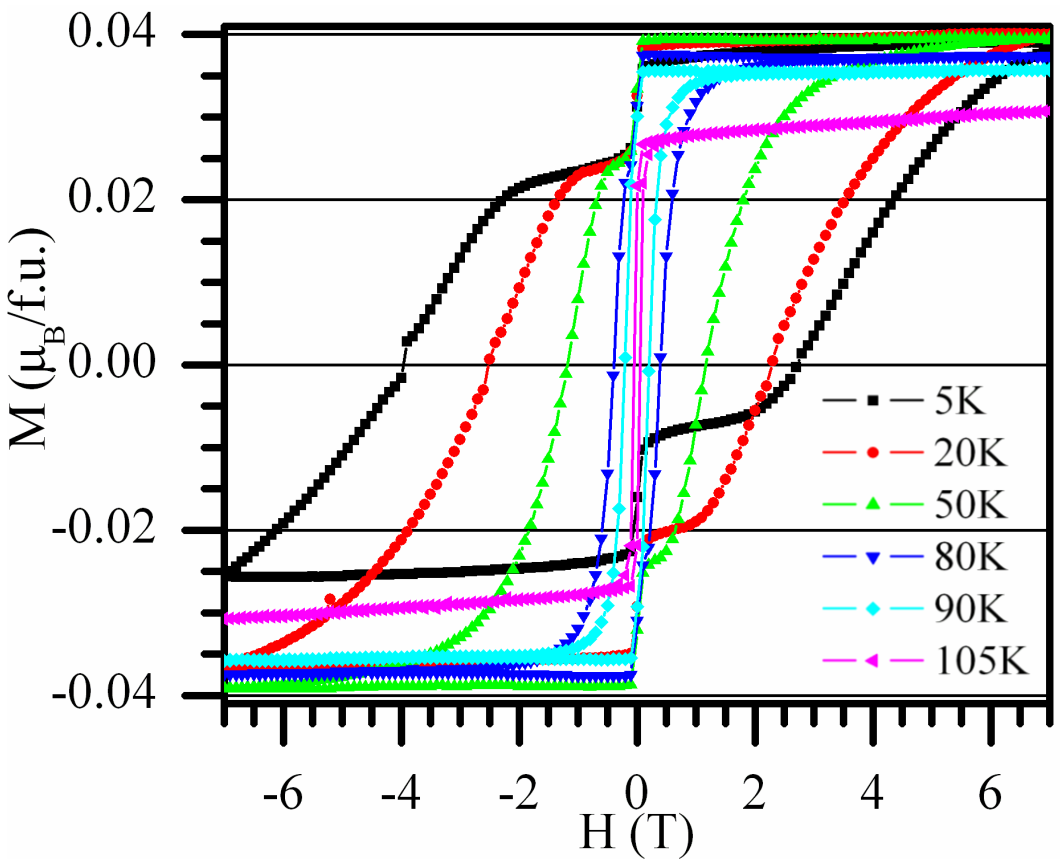

Fig.6.1.3 Thermal evolution (5-105K) of magnetisation-field hysteresis loop for $CaIrO_3$

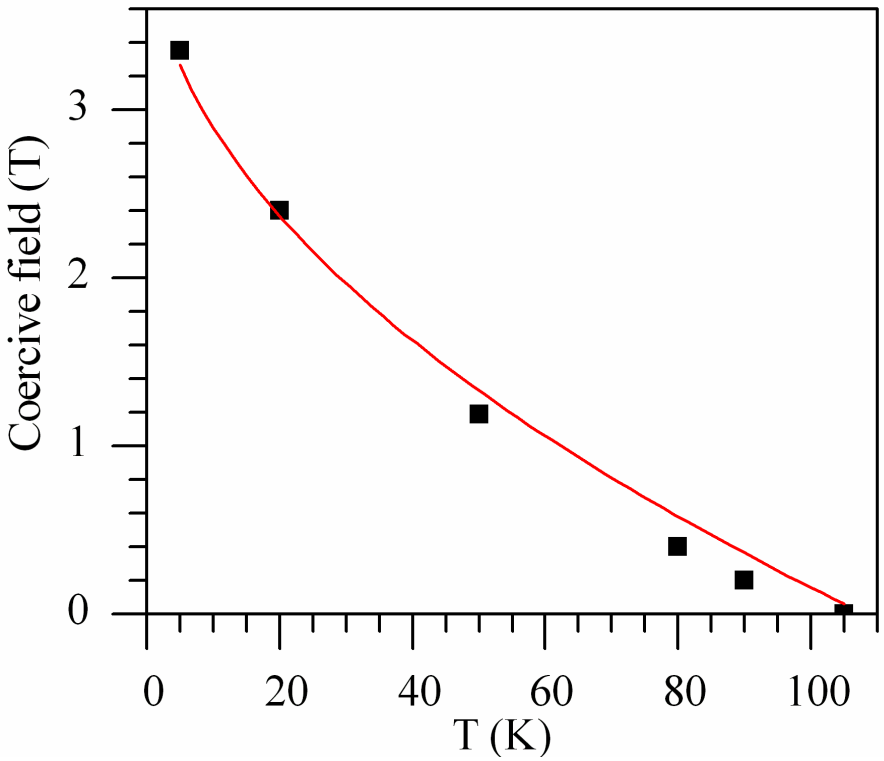

Fig.6.1.4 Temperature dependence of coercive field for $CaIrO_3$

(Fitted with: $H_c = 2\alpha K/M_s[1-(T/T_c)^{1/2}]$, $\alpha = 0.48$, $T_c = 108K$)

6.2 Charge-transport properties of $CaIr_{1-x}Pt_xO_3$

Electrical resistivity of $CaIrO_3$ and $CaIr_{0.5}Pt_{0.5}O_3$ were measured at 80K- 290K using a CCR (closed cryocooling refrigerator) at CSEC. The sample was first cooled down to 80K, and then the electrical resistivity was measured while heating the sample up to room temperature (290K). This was done to prevent any delay in the response of the sample during cooling, something which is frequently noted above 200K. Electrical resistivity of the pellet was studied by a four-point probe method with a gauge current of 0.99 mA, and the electrical contacts on the four locations along the sample (pellets were cut into cuboids) were prepared from Cu wires and silver paste. The electrical resistivity: ρ of the sample was calculated by the following equation using the respective parameters described in Fig.6.2.1:

$$\rho = (\Delta V / I)(A/L) \qquad (I = 0.99 \text{ mA})$$

The measured A (cm^2)/L (cm) values of the $CaIrO_3$ sample were 3.1 $x10^{-2}$ /0.52, while those of the $CaIr_{0.5}Pt_{0.5}O_3$ sample were 1.6 $x10^{-2}$ /0.19, respectively.

The temperature-dependent electrical resistivity of other $CaIr_{1-x}Pt_xO_3$ series was not measurable due to their extremely high resistivity. Such high resistivity may well be caused by the grain boundary effect. This is reasonable since $CaIrO_3$ and $CaIr_{0.5}Pt_{0.5}O_3$ have large grain size, while $CaIr_{0.7}Pt_{0.3}O_3$ and $CaIr_{0.3}Pt_{0.7}O_3$ have small grain size as pointed out in Chapter 4. Since $CaIr_{0.7}Pt_{0.3}O_3$ has less closed-shell Pt^{4+} (: $5d^6$) than $CaIr_{0.5}Pt_{0.5}O_3$, a lower resistivity is expected for $CaIr_{0.7}Pt_{0.3}O_3$. This observation demonstrates the

importance of grain boundary effects and the requirement of samples with large grain size for further charge-transport property measurements. Attempts to grow large grains of $CaIr_{0.7}Pt_{0.3}O_3$ and $CaIr_{0.3}Pt_{0.7}O_3$ using high P/T polycrystalline synthesis or flux methods for single crystal growth were, unfortunately, not successful.

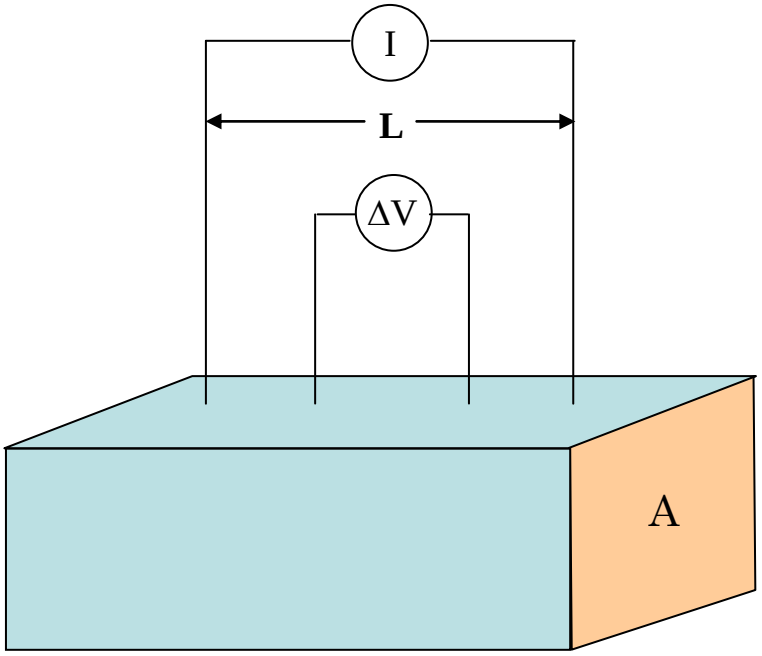

Fig.6.2.1 Demonstration of the four-point probe method applied for the electrical resistivity measurement of the cuboid samples of $CaIrO_3$ and $CaIr_{0.5}Pt_{0.5}O_3$, where I (A): gauge current applied to the sample, ΔV (V): voltage drop by the electrical resistance of the sample, L(cm): distance between the current source probe, A(cm^2): the cross section of the sample

The temperature dependences of electrical resistivity for $CaIrO_3$ and $CaIr_{0.5}Pt_{0.5}O_3$ are shown in Fig. 6.2.2. Both samples are narrow bandgap semiconductors

with bandgap energies of 140-150 meV (Table 6.2) estimated from the gradient of Arrhenius plots (Fig.6.2.3(a), (b)) by fitting a linear function. Arrhenius plots were applied over the temperature range 220-270K for $CaIrO_3$ and 210-240K for $CaIr_{0.5}Pt_{0.5}O_3$. These ranges were chosen due to temperature instability at high temperatures, typically above 280K. $CaIrO_3$ post-perovskite shows a semiconducting behaviour above 110K with a negative resistivity slope and a low resistivity: 10.1 Ωcm at room temperature. Electrical resistivity below 110K was not measurable due to the saturation of the sample voltage over 20V. This non-metallic behaviour of $CaIrO_3$ in electrical resistivity is likely to arise from the extrinsic grain boundary effect. Since a Pauli-paramagnetic feature was observed for $CaIrO_3$ above 150K (Fig.6.1.1(a)), $CaIrO_3$ should be intrinsically metallic. Thus, the observed semiconducting behaviour of $CaIrO_3$ implies that its intrinsic metallic behaviour is masked by insulating grain boundaries. In that sense, resistivity measurement on single crystalline $CaIrO_3$ would be constructive, but has not been successful due to its small crystal size (width of the needle-like crystals is below 20μm). $CaIr_{0.5}Pt_{0.5}O_3$ post-perovskite shows a semiconducting behaviour above 190K with a negative resistivity slope and a high resistivity: 8.37×10^6 Ωcm at room temperature. Electrical resistivity below 190K was not measurable due to the saturation of the sample voltage. Such high resistivity at room temperature implies that $CaIr_{0.5}Pt_{0.5}O_3$ is intrinsically a narrow bandgap (E_g: 150 meV) semiconductor. The large discrepancy from the resistivity of $CaIrO_3$ suggests that charge-transport of $CaIr_{0.5}Pt_{0.5}O_3$ is dominated by the closed-shell Pt^{4+} (: $5d^6$) rather than Ir^{4+}(: $5d^5$) with an unpaired electron.

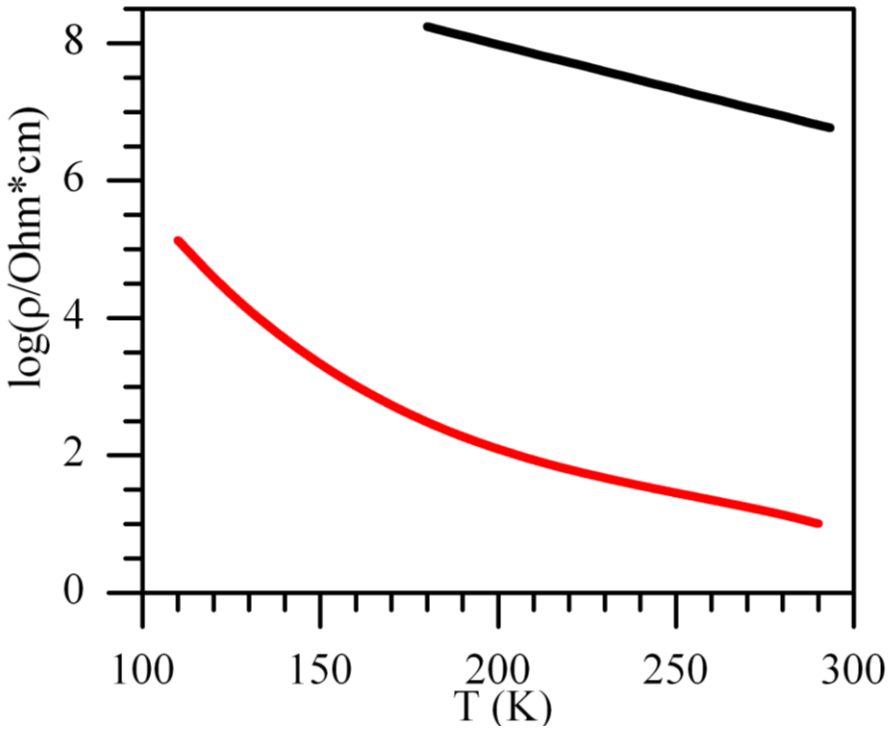

Fig.6.2.2 Temperature dependence of electrical resistivity for $CaIrO_3$ (red curve) and $CaIr_{0.5}Pt_{0.5}O_3$ (black curve)

Table 6.2: Electronic parameters of $CaIrO_3$ and $CaIr_{0.5}Pt_{0.5}O_3$

Compounds	$CaIrO_3$	$CaIr_{0.5}Pt_{0.5}O_3$
E_g (eV)	0.14	0.15
ρ_{290K} (Ωcm)	10.1	8.37×10^6

(a)

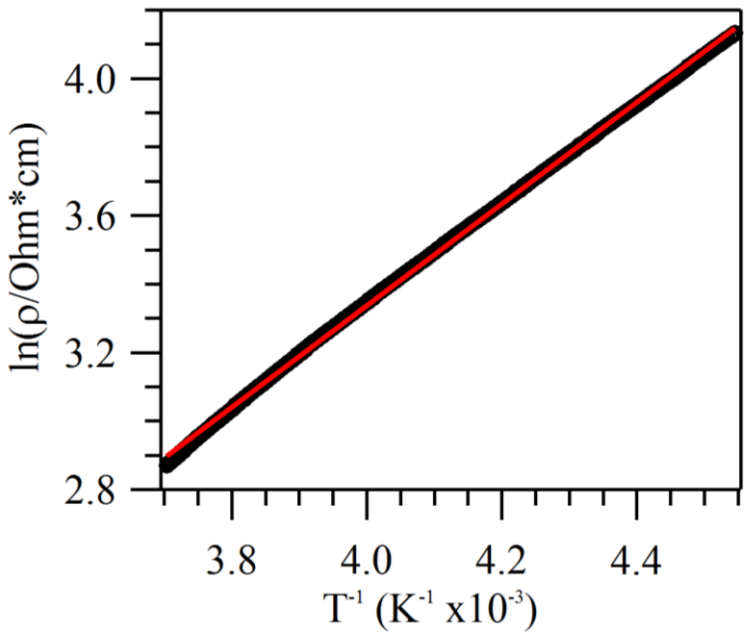

(b)

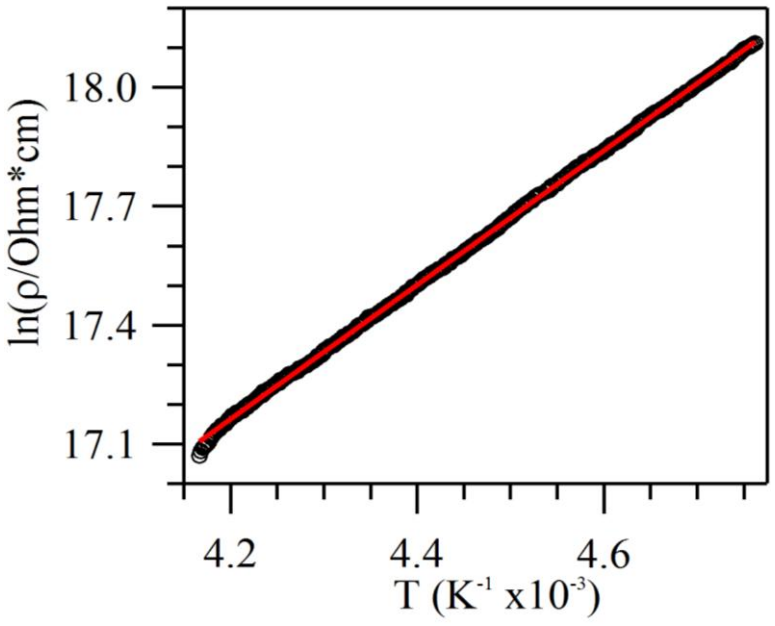

Fig.6.2.3 Arrhenius plots of (a) $CaIrO_3$ (T= 220-270K) and (b) $CaIr_{0.5}Pt_{0.5}O_3$ (T= 210-240K), the red coloured linear fit is a guide to the eye.

6.3 Specific heat of $CaIrO_3$ and $CaIr_{0.5}Pt_{0.5}O_3$ at ambient pressures

For directly calculating thermodynamic Grüneisen parameter γ_{th}, the specific heat (C_p) was measured at ambient pressure from 2K - 220K using a Quantum Design PPMS. Samples were attached to the addenda (with grease on the surface) which had been well calibrated in advance. First, the system was cooled down to 2K. Heat capacity measurements were conducted while heating the system up to 220K. The heat capacity above 220K was not measured since temperature control is unstable and heat capacity values are not reliable. Table 6.3 shows the Debye temperature and the heat capacity (C_p) at 200K for $CaIr_{0.5}Pt_{0.5}O_3$ and $CaIrO_3$. The low temperature specific heat can be written as $C_P = aT + bT^3$, with contributions from both electron and phonon terms. Plots of C_p/T against T^2 for $T < 14$ K (Fig. 6.3.2) were used to obtain the Debye temperatures T_D from the slopes b ($b = (12\pi^4/5)NR/T_D^3$; N: Number of atoms per formula unit, R: gas constant).

The thermodynamic Grüneisen parameter γ_{th} can be calculated as:

$$\gamma_{th} = \alpha K_{T0} V/(C_p + \alpha^2 K_{T0} VT)$$

(α: thermal expansion parameter, V: cell volume)

As C_p at 300K can be obtained by extrapolating the measured C_p curve (fitted with a polynomial function) to 300K, I obtain C_P = 108(1) J/mol K for $CaIr_{0.5}Pt_{0.5}O_3$. With V = 226.97(1) Å^3 (see Chapter 5 for detail) and taking α = 2.84(3) x 10^{-5} K^{-1} to be the same as for $CaIrO_3$ post-perovskite [33], a value of γ_{th} = 1.08(4) is obtained. This value is in good

agreement with the estimated γ_{th} value from mode Grüneisen parameter: 0.952. Thus, the assumption made in Chapter 4 that γ_{th} can be calculated from mode Grüneisen parameter seems to work well for the post-perovskite system as well. Thus, γ_{th} derived from mode Grüneisen parameter can be used to investigate the stability between post-perovskite and perovskite in $CaIr_{0.5}Pt_{0.5}O_3$, which gave 34 % increase across the phase transition. The thermodynamic Grüneisen parameter γ_{th} of $CaIrO_3$ directly calculated from the heat capacity (C_p) gives a value of γ_{th} = 1.25(6). Discrepancy of thermodynamic Grüneisen parameters between $CaIrO_3$ and $CaIr_{0.5}Pt_{0.5}O_3$ suggest the importance of measuring heat capacity for obtaining lattice dynamics information.

Fig.6.3.1 shows a similar temperature dependence of heat capacity of $CaIrO_3$ and $CaIr_{0.5}Pt_{0.5}O_3$. However, the heat capacity of $CaIrO_3$ is smaller than the solid solution at temperatures lower than 220K. This is likely due to long range ordering of magnetic spins of $CaIrO_3$ (T_c: 108K) at low temperatures. In fact, a peak around 108K was observed (Fig.6.3.3), similar to that noted in $CaRhO_3$[18]. The integrated entropy associated with the magnetic transition was estimated to be 0.063 J/mol K by subtracting the curve fitted in the temperature range of 2-95K, 114-220K against the polynomial function. This value is only 1.1 % of R ln2 (R: gas constant), which is expected from the configuration of Ir^{4+} ($5d^5$, S=1/2), and it is 25 % of that of $CaRhO_3$[18]. Such small magnetic entropy is another indication that $CaIrO_3$ is a metal with weak itinerant ferromagnetism[85], apart from the Pauli-paramagnetic feature and a small saturated magnetic moment observed in this study.

Next, the Sommerfeld coefficient: a of $CaIrO_3$ was calculated by the linear dependence of electron heat capacity: aT at 4-6K, where phonon components (bT^3) of heat

capacity and any possible Schottky contributions can be neglected. The intercept of C_p/T vs T^2 plot is not appropriate for deriving *b* since contribution from electrons is dominant over contributions from phonons at low temperatures in an itinerant electron system. The densities of state at the Fermi energy: $N(E_F)$ are estimated from the relationship: $a = 1/3\pi^2 k_B{}^2 N(E_F)$. Table 6.3 shows that the Sommerfeld coefficient and density of states at E_F (Fermi energy) for $CaIrO_3$ is large, which is in good agreement with the effect of spin fluctuation[89],[90] in metals enhanced by weak itinerant ferromagnetism. Table 6.3 shows that $CaIrO_3$ has a higher Debye temperature than $CaIr_{0.5}Pt_{0.5}O_3$, while their C_p at 200K is somewhat close to 80 J/mol K. The Debye temperature of $CaIrO_3$ is similar to $CaPtO_3$[17], while the Debye temperature of $CaIr_{0.5}Pt_{0.5}O_3$ is smaller than the end members. This implies that the cation disordering of Ir^{4+}/Pt^{4+} contributes significantly to the phonon-softening in the post-perovskite system.

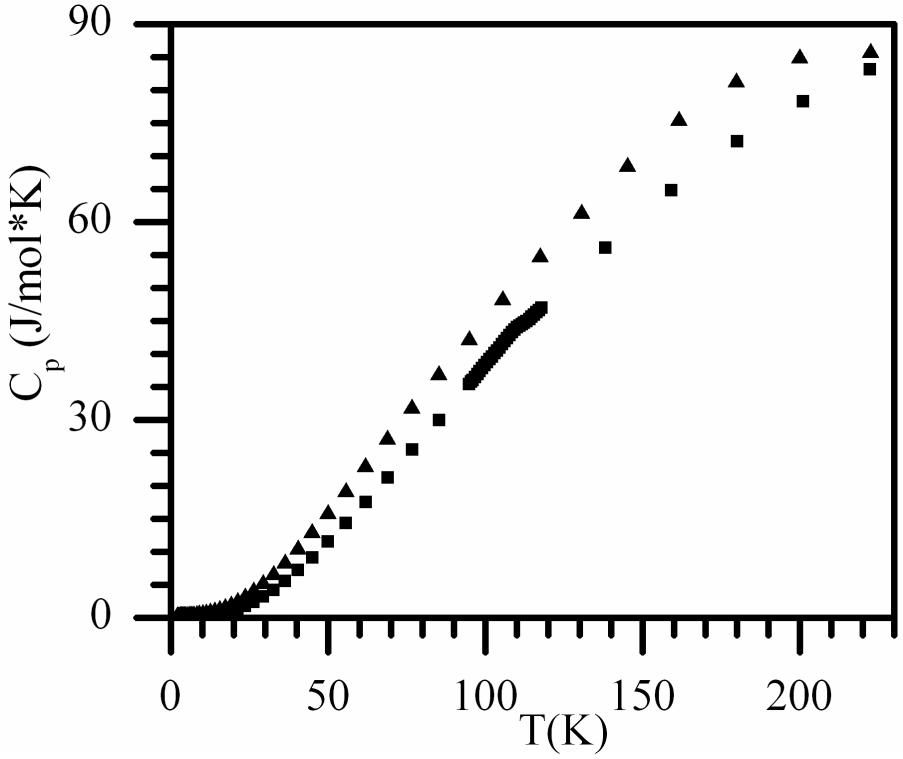

Fig.6.3.1 Temperature dependence of specific heat (C_p) of $CaIrO_3$ (denoted as black squares) and $CaIr_{0.5}Pt_{0.5}O_3$ (denoted as black triangles) measured at ambient pressure from 2K - 220K

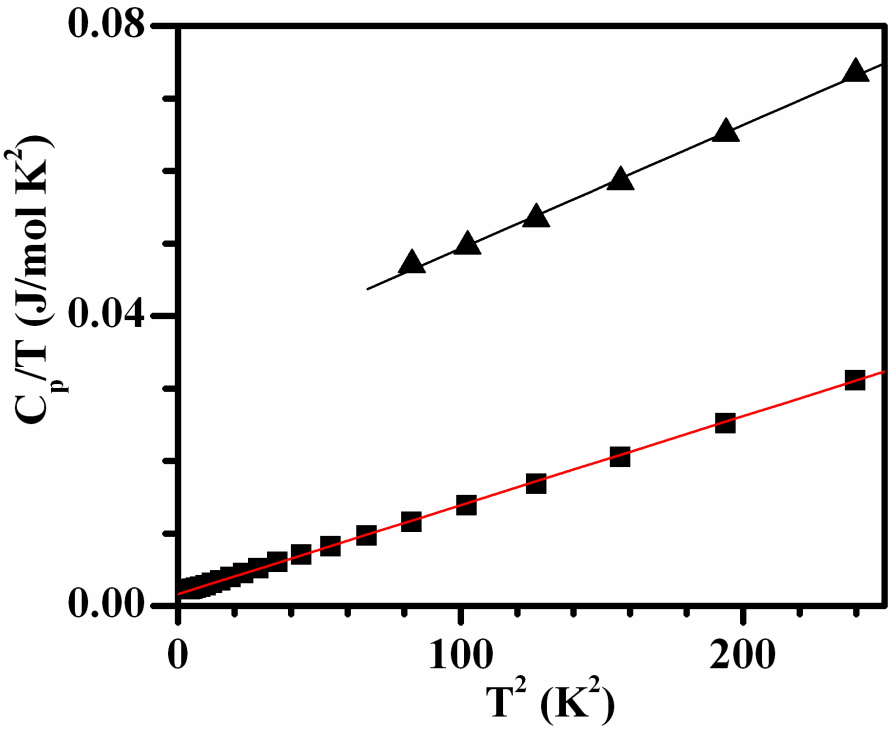

Fig.6.3.2 The linear increase of C_p/T against T^2, plotted for $CaIrO_3$ (denoted as black squares) and $CaIr_{0.5}Pt_{0.5}O_3$ (denoted as black triangles) at low temperatures below 14K

Table 6.3: Heat capacity parameters of $CaIr_{1-x}Pt_xO_3$ and $CaIr_{1-x}Rh_xO_3$ (x = 0, 0.5, 1), where electron density of states at the Fermi energy is denoted $N(E_F)$ (previously reported parameters of $CaPtO_3$ [17] ; Ohgushi et al., 2008 are shown for comparison)

Compound	$CaIrO_3$	$CaIr_{0.5}Pt_{0.5}O_3$	$CaPtO_3$ [17]
T_D (K)	433	385	410
Sommerfeld coefficient			
(mJ/mol K^2)	11.7	-----	0
$N(E_F)$ (eV^{-1} mol^{-1})	2.99 $x10^{24}$	-----	0
C_p at 200K (J/mol K)	78.3	84.8	85

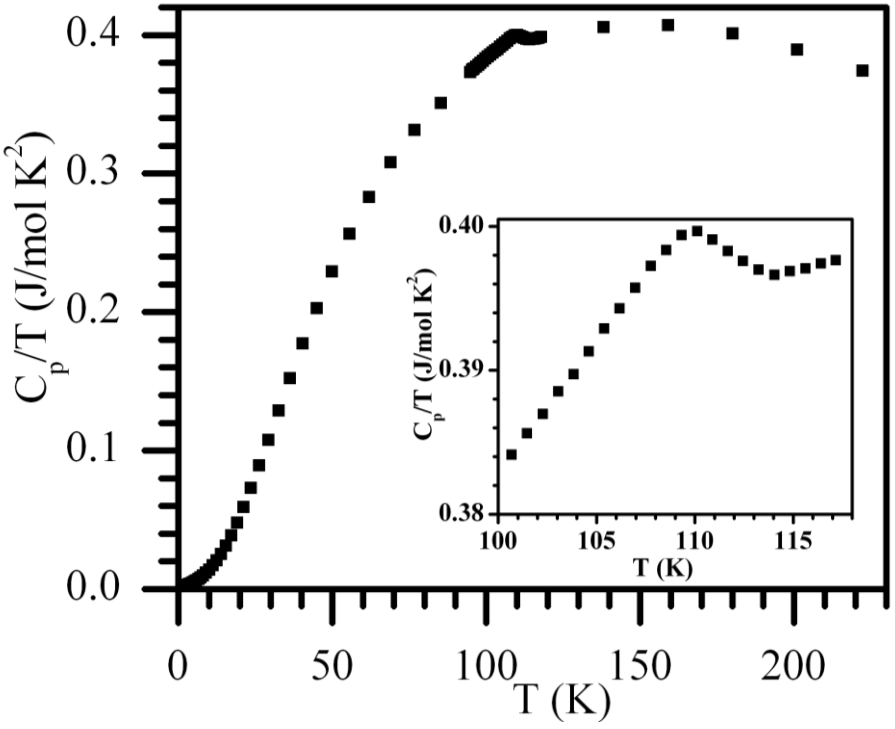

Fig.6.3.3 Temperature dependence of C_p/T of $CaIrO_3$ (C_p: specific heat, T: temperature) (the inset shows the expansion of C_p/T vs T curve, with emphasis near T_c = 108K)

6.4 Conclusions

The temperature-independent paramagnetism of $CaIrO_3$ was observed above 150 K and only 1.1 % of the expected magnetic entropy was identified by the heat capacity measurement of $CaIrO_3$, suggesting that $CaIrO_3$ is intrinsically a weak itinerant ferromagnetic metal. In contrast, the electrical resistivity measurement suggested that $CaIrO_3$ is extrinsically a narrow bandgap semiconductor with a bandgap energy of 140 meV.

The Curie temperature of $CaIrO_3$ post-perovskite is 108K. Pt substitution of $CaIrO_3$ induces Curie-Weiss paramagnetism and suppresses the Curie temperature to 20 K for $CaIr_{0.7}Pt_{0.3}O_3$ and to below 5 K for $CaIr_{0.5}Pt_{0.5}O_3$, yet maintaining the initial ferromagnetic interaction. $CaIrO_3$ possesses a small saturated magnetic moment of 0.04 μ_B, which is another implication that $CaIrO_3$ is intrinsically an itinerant ferromagnetic metal. The possession of small saturated magnetic moment was a feature for the whole $CaIr_{1-x}Pt_xO_3$ series.

The anisotropic layered structure of the *Cmcm* post-perovskite structure and the pronounced morphology of $CaIrO_3$ combined with the strong spin-orbit coupling of Ir^{4+} result in a remarkably large magnetic anisotropy constant of 1.77×10^6 Jm^{-3}. This value is comparable to the anisotropy constant of permanent magnets, such as $Nd_2Fe_{14}B$, suggesting that $CaIrO_3$ post-perovskite possesses further opportunity for industrial applications, such as magnetic recording.

7. Structural and physical properties of $CaIr_{0.5}Rh_{0.5}O_3$

7.1 High pressure synthesis of $CaIr_{0.5}Rh_{0.5}O_3$

$CaIr_{0.5}Rh_{0.5}O_3$ was synthesised at the GRC by high P/T solid-state reaction of CaO, IrO_2, and Rh_2O_3, with $KClO_4$ as an oxidizer. A well-ground mixture of the starting materials at a ratio of 1/0.5/0.5/4.07 (Ca/Ir/Rh/O) was placed into a gold capsule (diameter: ϕ =2.5 mm) sandwiched by MgO disks (diameter: ϕ =2.7 mm), which minimizes the chemical reduction within the cell. Excess amounts of O were added by use of $KClO_4$ in order to oxidize all the Rh^{3+} into Rh^{4+}. Fig.7.1 shows the cell assembly used for the synthesis of $CaIr_{0.5}Rh_{0.5}O_3$. The octahedral cell was heated in a multi-anvil apparatus, which is capable of maintaining 15 GPa during heating. Samples were annealed at 1300 ℃ for 40 min, followed by rapid quenching to ambient temperature, and finally the release of pressure. Dense and dark black pellets of the sample were obtained. $CaIr_{0.5}Rh_{0.5}O_3$ was well flushed with distilled water in order to remove excess KCl.

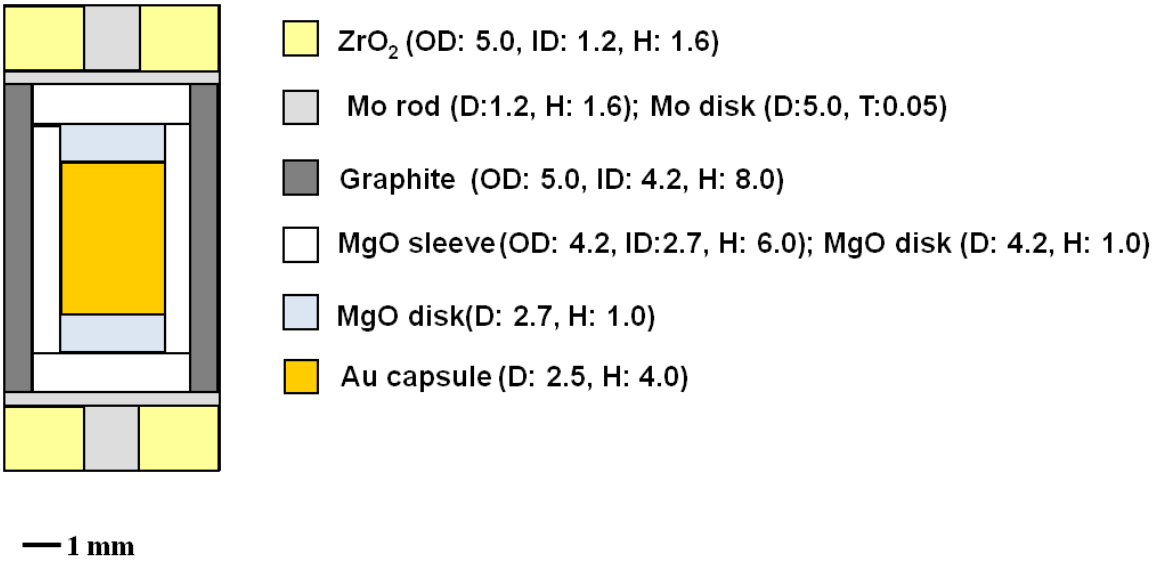

Fig.7.1 Cell assembly for high pressure/temperature synthesis of $CaIr_{0.5}Rh_{0.5}$ using multi-anvil apparatus (15GPa, 1300 ℃) (OD: outer diameter; ID: inner diameter; D: diameter; H: height; T: thickness, all units are in mm)

7.2 Structural properties and the morphology of $CaIr_{0.5}Rh_{0.5}O_3$

The X-ray diffraction (XRD) pattern (Fig. 7.2.1) demonstrates that the recovered $CaIr_{0.5}Rh_{0.5}O_3$ sample contains post-perovskite with traces of a secondary phase: KCl. All of the major XRD peaks are indexed by the $CaIrO_3$-type cell with orthorhombic space group *Cmcm*. The morphologies and stoichiometry of the $CaIr_{0.5}Rh_{0.5}O_3$ sample were examined by SEM/EDX analysis. Traces of additional elements were not detected for any of the samples in the EDX pattern (Fig.7.2.2). The mean grain size varies between grains

from 2-3 μm as shown in the micrographs in Fig. 7.2.3 and as summarised in Table 7.2.1. The crystallites show a needle-like morphology. The solid solution of $CaIrO_3$ and $CaRhO_3$ share *a*-axis elongated needle-like grain-growth features with $CaIrO_3$ and $CaPtO_3$, which has been previously reported by Hirai[16], Ohgushi[17] and Miyajima[57].

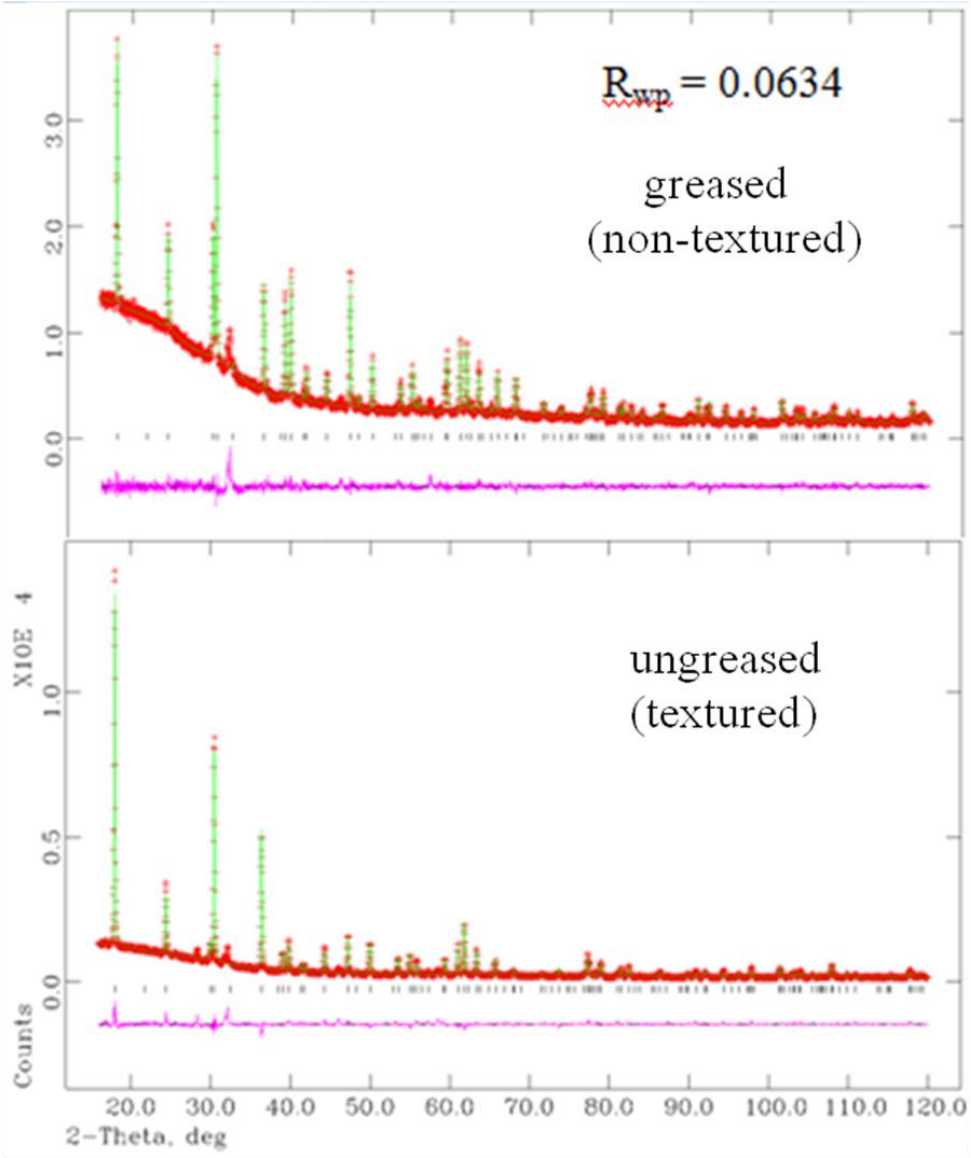

Fig.7.2.1 Fitted powder X-ray diffraction profiles of $CaIr_{0.5}Rh_{0.5}O_3$ (the additional peak around 31 degrees comes from a diffraction peak of KCl)

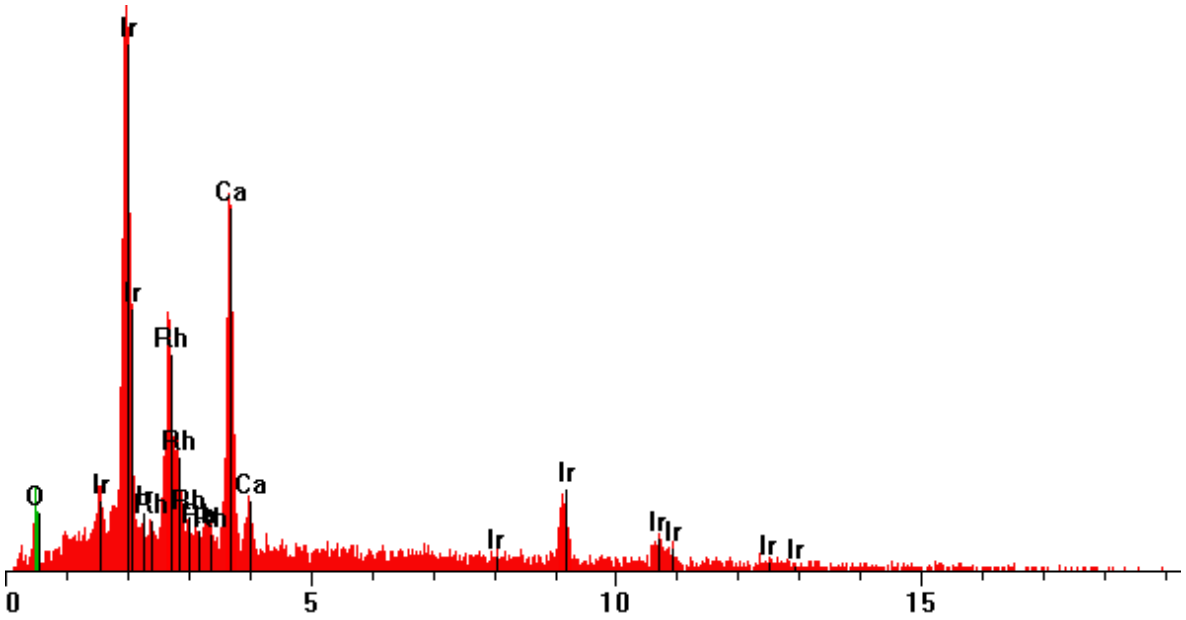

Fig.7.2.2 Energy Dispersive X-ray diffraction (EDX) pattern of $CaIr_{0.5}Rh_{0.5}O_3$ collected for 480 s showing that no additional element exists in the sample.

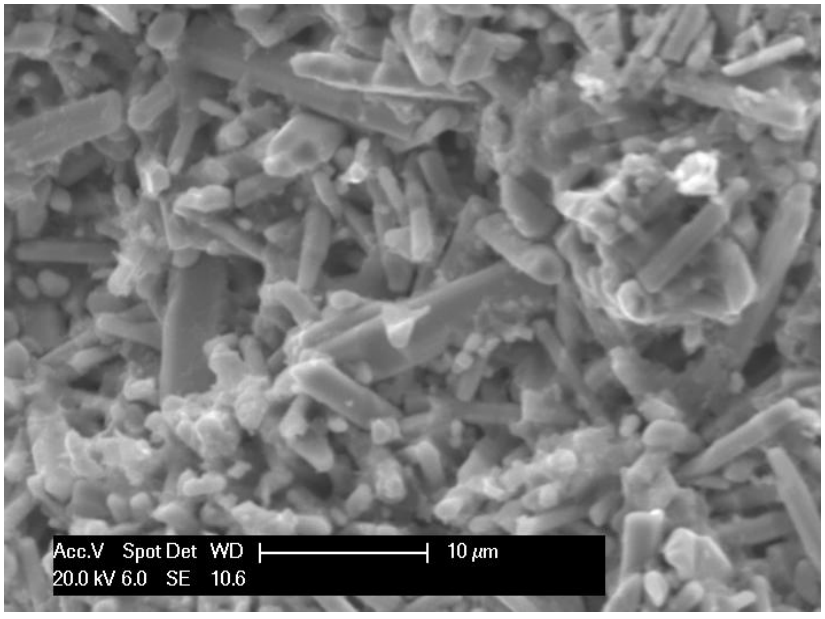

Fig.7.2.3 Typical SEM image of grains of $CaIr_{0.5}Rh_{0.5}O_3$ (scale bar = 10 μm)

Table 7.2.1: Grain sizes and crystallographic results for $CaIr_{0.5}Rh_{0.5}O_3$

Compounds	$CaIr_{0.5}Rh_{0.5}O_3$
Grain size (μm)	2.0 - 3.0
a (Å)	3.11997(6)
b (Å)	9.8652(1)
c (Å)	7.2930(1)
V ($Å^3$)	224.476(8)
R_{wp}	0.0634
χ^2	1.62
Ca: y	0.2484(4)
O1: y	0.441(2)
O2: y	0.132(1)
O2: z	0.435(1)
U_{iso} ($Å^2$)	0.0077(9)
M-O1 (Å)	1.913(5) x2
M-O2 (Å)	2.087(7) x4
<M-O> (Å)	2.026(6)
M-O1 valence	0.87(1)
M-O2 valence	0.55(1)
BVS (Ir)	3.94(6)
M-O1-M (°)	145(1)
M-O2-M (°)	96.8(4)
O1-M-O2(°)	91.6(4)
O2-M-O2(°)	96.8(4)

Bond valences of M-O bonds were calculated as $\exp((R_i-R_0)/B)$ with R_0 values of 1.870 (Ir^{4+}-O^{2-}), 1.857 (Rh^{4+}-O^{2-}).

Initial Rietveld fit to the XRD profile showed that there is a strong preferred orientation present in the loosely packed powders and so another pattern was collected from the sample sieved onto a greased surface to minimize this effect. Large differences between the two XRD patterns are evident in Fig. 7.2.1. Fits to the greased samples were used to refine the crystal structure parameters, giving the results shown in Table 7.2.1. The bond valence sum (BVS) of Ir-O bonds makes 3.94 vu (Table 7.2.1), which is almost equal to the formal valence of Ir^{4+}. Therefore, the bond distances agree well with the bond valence theory. In conclusion, the refinement results have been found to be appropriate for the $CaIrO_3$ structure.

To obtain morphological information from the XRD pattern of loosely packed powder of $CaIr_{0.5}Rh_{0.5}O_3$, the crystal structure parameters were fixed at the values obtained from the greased samples, and the intensities were Rietveld-fitted by varying the nine ODF (Orientation Density Function) coefficients that describe a cylindrical symmetry sample texture up to 6^{th} order (see Chapter 5). The refinement using this ODF gave a good fit to the peak intensities as shown in Fig. 7.2.1. The orientation densities derived from the refined ODF parameters are shown in Fig. 7.2.4, which show the density of crystallites with plane (hkl) at an angle ψ to the sample plane, relative to the average (untextured) value of 1.0. The maximum density for (100) is at $\psi = 90°$, showing that the crystallographic a-axis is parallel to the long dimension of the needle-like crystals. It is worthwhile to compare the texture of $CaIr_{0.5}Rh_{0.5}O_3$ with that of $CaIrO_3$ (Fig.5.3.1(a), Chapter 5). Maximas in both (010) and (001) densities are found at $\psi = 0$, but a systematic change from (001) to (010)

density is observed as Ir is substituted by Rh. This shows that Rh substitution favours (001) over (010) growth. The magnitudes of the orientation density maxima in $CaIr_{0.5}Rh_{0.5}O_3$ and $CaIrO_3$ do not correlate with the grain sizes observed by SEM. The large grain $CaIrO_3$ show maximum densities of near 3, whereas the smaller-grained $CaIr_{0.5}Rh_{0.5}O_3$ sample shows the extreme texture with an (0 1 0) density of 4.0 at $\psi = 0$.

Fig. 7.2.4: Angular dependence of crystallite orientation density of $CaIr_{0.5}Rh_{0.5}O_3$.

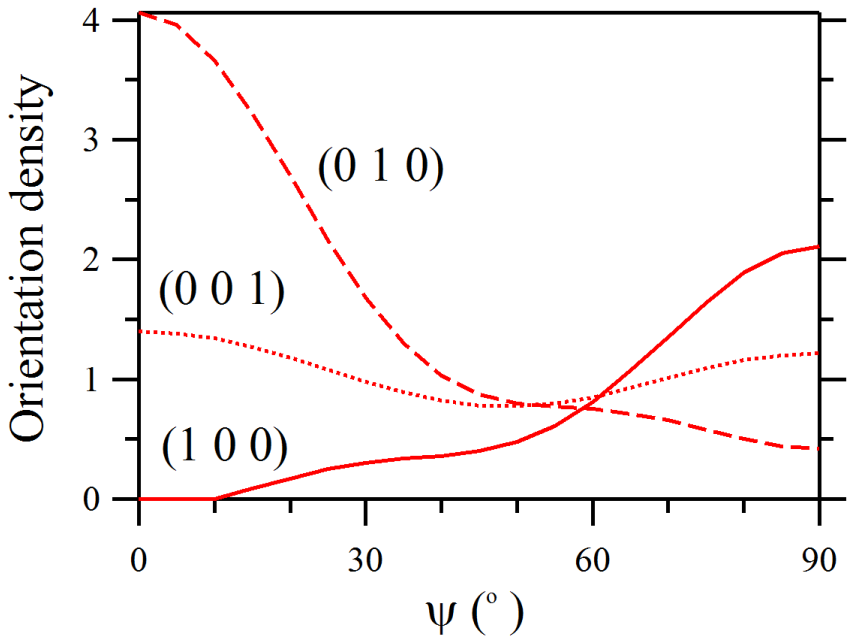

7.3 Magnetic properties of $CaIr_{0.5}Rh_{0.5}O_3$

Magnetic properties were measured using a Quantum Design MPMS SQUID magnetometer. The sample was packed in a gelatine capsule (filled with nonmagnetic cotton) and placed in the middle of a plastic straw before inserting into the SQUID. Zero field- and field-cooled (ZFC and FC) measurements were made with a field of 100 Oe after cooling the sample down to 5 K.

Fig.7.3.1 shows the temperature dependence of magnetic susceptibility (M/H) for $CaIr_{0.5}Rh_{0.5}O_3$. $CaIr_{0.5}Rh_{0.5}O_3$ shows a ferromagnetic transition at 40 K. The inverse susceptibility of $CaIr_{0.5}Rh_{0.5}O_3$ at 150-300 K is shown in the inset to Fig. 7.3.1, and the derived parameters of the fitted curve are shown in Table 7.3. The inverse susceptibilities of the samples at 150-300 K were fitted using the equation $1/\chi = [\alpha + C/T-\theta]^{-1}$ which includes Pauli and Curie-Weiss terms. $CaIr_{0.5}Rh_{0.5}O_3$ has a near-zero θ, implying ferromagnetic exchange interaction between spins. Magnetisation-field data from -7 T to 7 T are shown in Fig. 7.3.2. A magnetic hysteresis loop close to linear was observed. This suggests that only short range ferromagnetic interactions are present due to the Ir/Rh disordering in $CaIr_{0.5}Rh_{0.5}O_3$. $CaIr_{0.5}Rh_{0.5}O_3$ shows near-zero saturated magnetisation. Such a small magnetic moment implies that $CaIr_{0.5}Rh_{0.5}O_3$ is a metal with weak itinerant ferromagnetism.

Ferromagnetic interaction for $CaIr_{0.5}Rh_{0.5}O_3$ is in good agreement with Kanamori-Goodenough's rule[80] described in terms of cation-cation ordering, indicating that the direct ferromagnetic interaction of Ir^{4+}-Ir^{4+} in the crystallographic *a*-axis direction is dominant over the indirect antiferromagnetic interaction of Ir^{4+}-O^{2-}-Ir^{4+} in the

crystallographic *c*-axis direction.

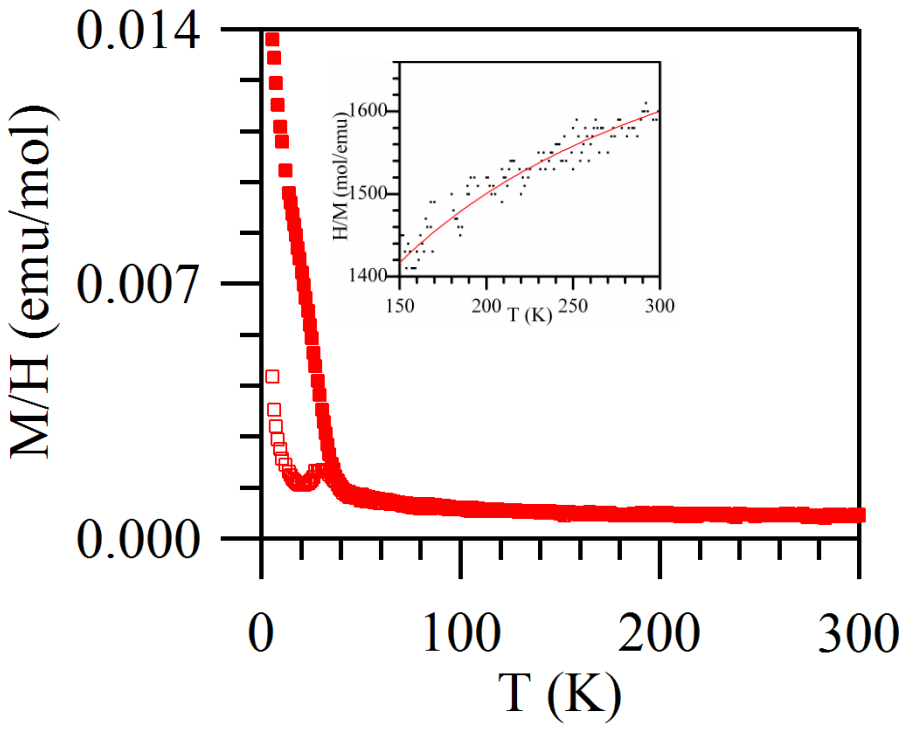

Fig.7.3.1 ZFC and FC (open and closed symbols in order) magnetic susceptibilities (M/H) of $CaIr_{0.5}Rh_{0.5}O_3$ (inset shows the Curie-Weiss fit between 150 K and 300 K)

Table 7.3: Magnetic parameters of $CaIr_{0.5}Pt_{0.5}O_3$

Compounds	$CaIr_{0.5}Rh_{0.5}O_3$
α (emu.mol^{-1})	0.00043(1)
θ (K)	-16(12)
C (emu.K.mol^{-1})	0.028(9)
μ_{eff} (μ_B/f.u.)	0.5(3)
T_c (K)	40

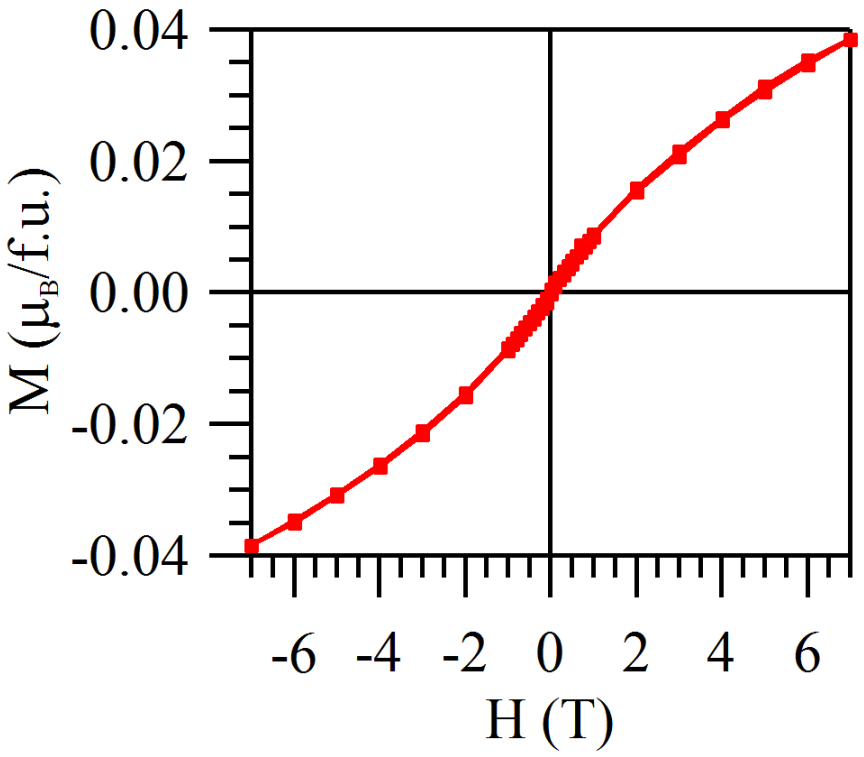

Fig.7.3.2 Magnetisation-field hysteresis loop from -7 T to 7 T for $CaIr_{0.5}Rh_{0.5}O_3$

7.4 Charge-transport properties of $CaIr_{0.5}Rh_{0.5}O_3$

Electrical resistivity of $CaIr_{0.5}Rh_{0.5}O_3$ was measured at 2K- 290K using the Quantum Design PPMS at CSEC. PPMS was chosen instead of CCR since the sample showed low resistivity at room temperature. Electrical resistivity of the pellet was studied by a four-point probe method with a gauge current of 0.99 mA, and the electrical contacts on the four locations along the sample (the pellet was cut into an orthorhombic shape) were prepared from Cu wires and silver paste. The electrical resistivity: ρ of the sample was calculated by the following equation using the respective parameters described in Fig.6.2.1:

$$\rho = (\Delta V / I)(A/L) \qquad (I = 0.99 \text{ mA})$$

The measured A (cm^2)/L (cm) value of the $CaIr_{0.5}Rh_{0.5}O_3$ sample was 1.2 $x10^{-2}$ / 0.20, respectively.

The temperature dependence of electrical resistivity of $CaIr_{0.5}Rh_{0.5}O_3$ is shown in Fig. 7.4.1. The sample turned out to be a narrow bandgap semiconductor with bandgap energies of 34 meV (Table 7.4) estimated from the gradient of the Arrhenius plot (Fig.7.4.2) by fitting with a linear function. The bandgap is even smaller compared with $CaIrO_3$ (Table 7.4). The Arrhenius plot was applied in the temperature range of 190-260K. This temperature range was chosen due to temperature instability at high temperatures, typically above 280K. $CaIr_{0.5}Rh_{0.5}O_3$ shows a semiconducting behaviour above 16K with a negative resistivity slope and a low resistivity: 6.79 Ω cm at room temperature. Such temperature dependence and room temperature resistivity is similar to $CaIrO_3$. Electrical resistivity below 16K was not measurable due to the saturation of the sample voltage over 10V. Since

the bandgap is extremely small and the resistivity at room temperature is low, the non-metallic behaviour of electrical resistivity for $CaIr_{0.5}Rh_{0.5}O_3$ is likely to come from the extrinsic grain boundary effect. As the grain size of $CaIr_{0.5}Rh_{0.5}O_3$ (: 2-3 μm) is smaller than that of $CaIrO_3$ (: 8 μm), such effect should become even more dominant in $CaIr_{0.5}Rh_{0.5}O_3$.

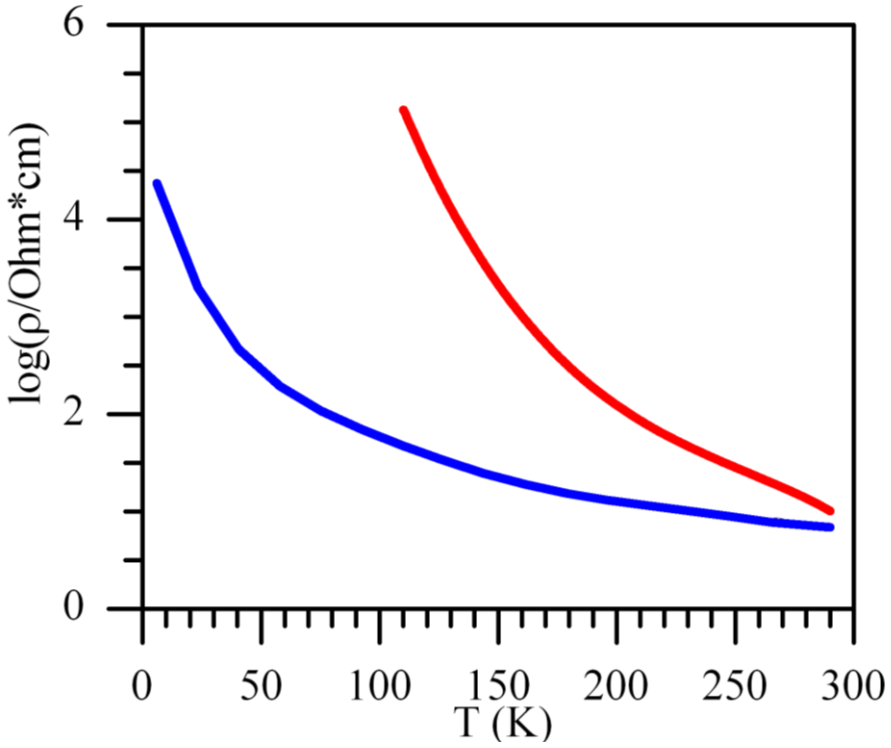

Fig.7.4.1 Temperature dependence of electrical resistivity for $CaIr_{0.5}Rh_{0.5}O_3$ (the curve in blue) and $CaIrO_3$ (the curve in red) for comparison

Table 7.4: Electronic parameters of $CaIr_{0.5}Rh_{0.5}O_3$ and $CaIrO_3$ for comparison

Compounds	$CaIrO_3$	$CaIr_{0.5}Rh_{0.5}O_3$
E_g (eV)	0.14	0.034
ρ_{290K} (Ωcm)	10.1	6.79

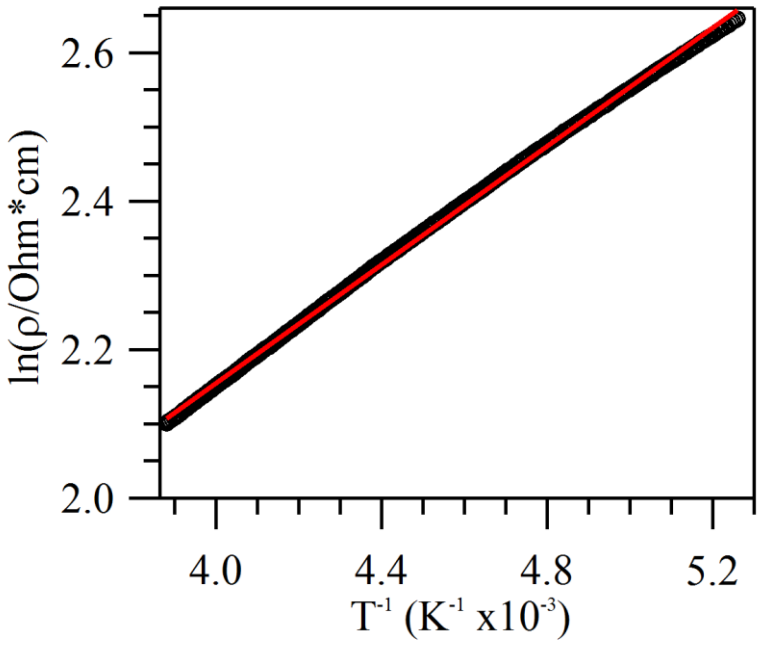

Fig.7.4.2 Arrhenius plot of $CaIr_{0.5}Rh_{0.5}O_3$ in the temperature range of 190-260K

(the fitted linear function is a guide to the eye)

7.5 Specific heat of $CaIr_{0.5}Rh_{0.5}O_3$ at ambient pressures

The specific heat (C_p) of $CaIr_{0.5}Rh_{0.5}O_3$ was measured at ambient pressure from 2K - 220K using a Quantum Design PPMS. The sample was attached to the addenda (with grease on the surface) which had been well calibrated in advance. First, the system was cooled down to 2K and the heat capacity measurement was conducted whilst heating the system up to 220K. The heat capacity above 220K was not measured since the temperature control is unstable. Fig.7.5.1 shows temperature dependence of the heat capacity of $CaIr_{0.5}Rh_{0.5}O_3$ and $CaIrO_3$ for comparison. The heat capacity of $CaIr_{0.5}Rh_{0.5}O_3$ is larger than that of $CaIrO_3$ at temperatures lower than 150K. This is likely due to short range ordering of magnetic spins of $CaIr_{0.5}Rh_{0.5}O_3$ (T_c: 40K) at low temperatures. $CaIr_{0.5}Rh_{0.5}O_3$ undergoes a magnetic transition at 40K, but no heat capacity anomaly around 40 K was observed. This implies that $CaIr_{0.5}Rh_{0.5}O_3$ is a weak itinerant ferromagnetic metal, as is the case with $CaIrO_3$. Thus, the Sommerfeld coefficient: a of $CaIr_{0.5}Rh_{0.5}O_3$ was calculated by the linear dependence of electron heat capacity: aT at 4-6K, where Schottky (C_s) and phonon components (bT^3) of heat capacity can be neglected. Table 7.5 shows that the Sommerfeld coefficient and density of states at E_F (Fermi energy) for $CaIr_{0.5}Rh_{0.5}O_3$ is large, which is in good agreement with the effect of spin fluctuation[86],[87] in metals enhanced by weak itinerant ferromagnetism. The previously reported small magnetic entropy and a large Sommerfeld coefficient of $CaRhO_3$[18] suggests that $CaRhO_3$ is in fact a weak itinerant ferromagnetic metal masked by insulating grain boundaries. Table 7.5 shows that $CaIrO_3$, $CaIr_{0.5}Rh_{0.5}O_3$ and $CaRhO_3$ have a diverse range of Debye temperature, while their C_p at 200K is uniform around 80 J/mol K. The Debye temperatures were calculated by using the

linear increase of C_p/T against T^2 (T< 14K) (Fig.7.5.2), while those of $CaIrO_3$ and $CaRhO_3$[14] are shown for comparison. The Debye temperature of $CaIr_{0.5}Rh_{0.5}O_3$ is somewhat smaller than those of end members. This is likely to be a phonon softening effect due to the cation disordering of Ir^{4+}/Rh^{4+}.

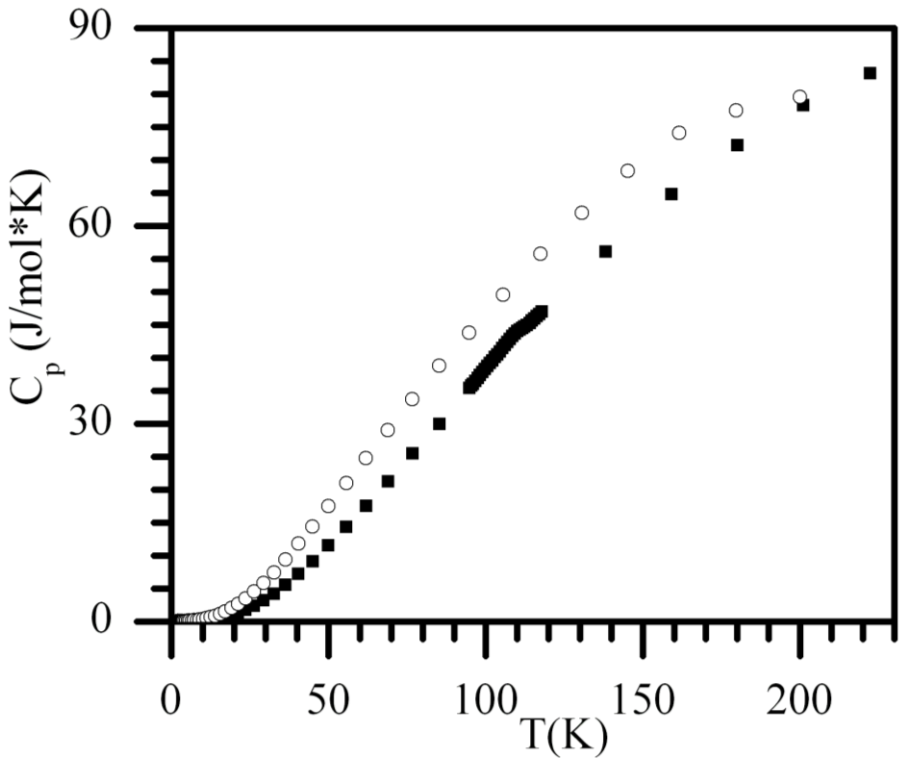

Fig.7.5.1 Temperature dependence of specific heat (C_p) of $CaIr_{0.5}Rh_{0.5}O_3$ (denoted as white circles) measured at ambient pressure from 2K - 220K The temperature dependence of specific heat (C_p) of $CaIrO_3$ (denoted as black squares) is shown for comparison

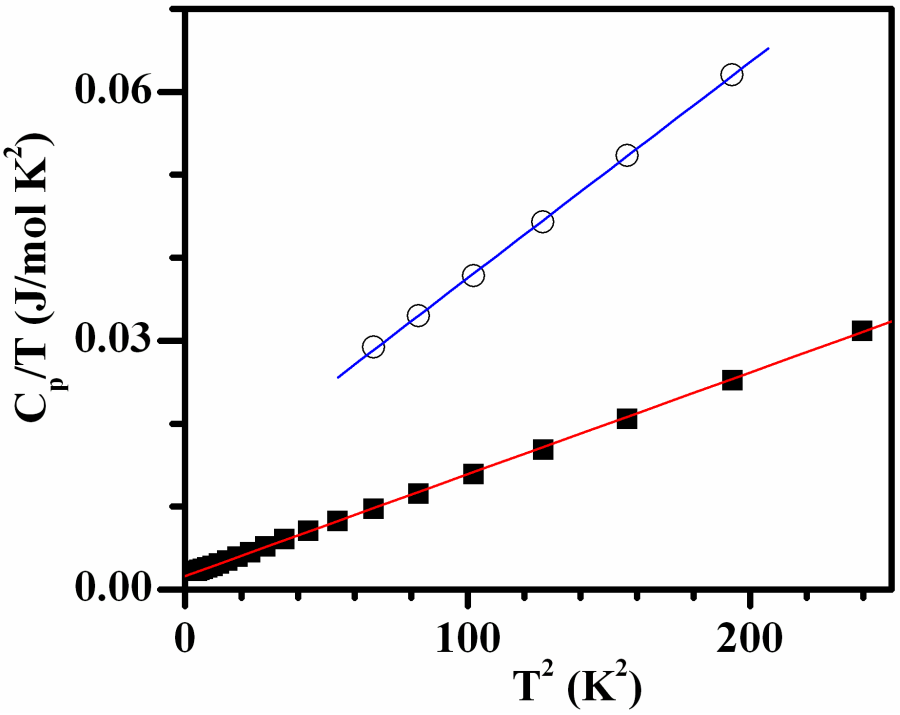

Fig.7.5.2 The linear increase of C_p/T against T^2, plotted for $CaIr_{0.5}Rh_{0.5}O_3$ (denoted as white circles) and $CaIrO_3$ (denoted as black squares) at low temperatures below 14K

Table 7.5: Heat capacity parameters of $CaIr_{1-x}Rh_xO_3$ (x = 0, 0.5, 1), where electron density of states at the Fermi energy is denoted $N(E_F)$ (previously reported parameters of $CaRhO_3$[18]; Yamaura et al., 2009 are shown for comparison)

Compound	$CaIrO_3$	$CaIr_{0.5}Rh_{0.5}O_3$	$CaRhO_3$ [18]
T_D (K)	433	335	524
Sommerfeld coefficient (mJ/mol K^2)	11.7	27.6	4.14
$N(E_F)$ (eV^{-1} mol^{-1})	2.99 x10^{24}	7.05 x10^{24}	1.06 x10^{24}
C_p at 200K (J/mol K)	78.3	79.5	80

7.6 Conclusions

The Rietveld refinement of X-ray diffraction profile of $CaIr_{0.5}Rh_{0.5}O_3$ revealed that $CaIr_{0.5}Rh_{0.5}O_3$ crystallizes in the $CaIrO_3$- structure. Elongated rod like crystal grains of 2-3 μm were observed for $CaIr_{0.5}Rh_{0.5}O_3$ using the SEM. The effect of Rh substitution results in remarkable texture of $CaIr_{0.5}Rh_{0.5}O_3$. Rh substituted $CaIrO_3$ favours (001) growth over (010) growth, similar to the case of Pt substituted $CaIrO_3$.

Rh substitution of $CaIrO_3$ induces Curie-Weiss paramagnetism and suppresses the initial Curie temperature (: 108K) to 40K, yet maintaining the initial ferromagnetic interaction. $CaIr_{0.5}Rh_{0.5}O_3$ possesses a small saturated magnetic moment of 0.04 μ_B, comparable to that of $CaIrO_3$.

Magnetic entropy of $CaIr_{0.5}Rh_{0.5}O_3$ was not observed around the Curie temperature in the heat capacity measurement, suggesting that $CaIr_{0.5}Rh_{0.5}O_3$ is intrinsically a weak ferromagnetic metal. In contrast, electrical resistivity measurement suggested that $CaIr_{0.5}Rh_{0.5}O_3$ is extrinsically a narrow bandgap semiconductor with a bandgap energy of 34 meV. The Debye temperature of $CaIr_{0.5}Rh_{0.5}O_3$ is 335 K, which is smaller than that of $CaIrO_3$ and $CaRhO_3$. This may well be a phonon softening effect due to the cation disordering of Ir^{4+}/Rh^{4+}.

8. Conclusions and future works

8.1 Conclusions

High-quality polycrystalline samples of post-perovskite type $CaIr_{1-x}Pt_xO_3$ solid solutions (x = 0.3, 0.5, 0.7) and $CaIr_{0.5}Rh_{0.5}O_3$ have been synthesised for the first time at a pressure of 15 GPa, and the detailed crystal structure, texture and morphology, phase transitions at high pressure/temperature conditions, charge-transport property, magnetic property and the behaviour of heat capacity, determined. Crystal structure parameters and the space group (: *Cmcm*) of $CaIr_{1-x}Pt_xO_3$ series (x = 0, 0.3, 0.5, 0.7) and $CaIr_{0.5}Rh_{0.5}O_3$ were successfully determined by Rietveld refinement based on the powder X-ray diffraction profile collected at ambient conditions. A marked effect of Pt substitution in $CaIr_{1-x}Pt_xO_3$ series was observed in the change of refined lattice constants. The *a*- and *b*-axis lengths change linearly with composition, while the *c*-axis length shows curvature and lies below the values of a linear interpolation between the end-members. The non-linear change of *c*-axis suggests local ordering of Ir/Pt: sustaining metal-metal (Ir^{4+}-Ir^{4+}) bonding in order to stabilise the post-perovskite structure. Substantial [100] grain growth was detected by texture analysis in all the solid solutions of $CaIrO_3$ leading to a needle-like morphology of their crystal grains. A pronounced difference between $CaIrO_3$ and its solid solutions were characterized by the distribution of the orientation of density of the crystal grains. Both Pt and Rh substitution of $CaIrO_3$ favours [001] grain growth over [010] grain growth, while $CaIrO_3$ favours [010] grain growth over [001] grain growth. Such anisotropic grain growth of the post-perovskite structure has important implication to the S-wave velocity splitting

up to 4 % for the two different ray path (SKS and SKKS) from the core mantle boundary found in the seismic data received at seismic stations positioned at circum-Pacific regions for monitoring the arrival of seismic waves (Lay et al., 1998)[3]. Since SKS and SKKS have almost identical ray paths in the upper mantle, propagation through the lower mantle must be anisotropic in order to cause the S-wave velocity splitting of 4 %, where horizontally polarized S-wave is faster than vertically polarized S-wave. While P-wave motion is parallel to the direction of propagation, S-wave shear motion is perpendicular to the direction of propagation. Thus, when seismic wave propagates through a mineral with anisotropic crystal structure, P-wave is only polarized in the direction of propagation, while S-wave splits into horizontally- and vertically- polarized S-waves. The lower mantle is mainly composed of $(Mg,Fe)SiO_3$ perovskite (Kesson et al., 1998)[2], which has an isotropic crystal structure, while the mineral composing the D" layer is not well known. Therefore, if a mineral with anisotropic crystal structure exists in the D" layer, it can explain the observed S-wave anisotropy.. Crystal grains of the $MgSiO_3$ post-perovskite are expected to grow with a platy habit, which can be synthesised at similar conditions to D" layer, and its preferred orientation due to its anisotropic crystal structure was used to explain why horizontally polarized S-wave is faster than vertically polarized S-wave by 4% difference in velocity at the D" layer (Oganov et al., 2004; Oganov et al., 2005). However, the direction of the fast axis depends on the orientation of the anisotropic crystal of $MgSiO_3$ post-perovskite. The slip plane of a mineral becomes horizontal to the ground due to the plastic deformation at high pressure conditions in the Earth. Thus, the slip plane of $MgSiO_3$ post-perovskite determines whether the observed S-wave anisotropy can be explained by

the anisotropic crystal structure of post-perovskite. Miyagi et al.(2010)[91] determined the slip plane of $MgSiO_3$ post-perovskite as (0 0 1) by conducting an axial deformation experiment at 148-185GPa with a diamond anvil cell, and S-wave polarized anisotropy calculated from elastic constants assuming (0 0 1) as the slip plane matched well with the observed S-wave anisotropy. The slip plane of $(Mg,Fe)SiO_3$ post-perovskite is also determined as (0 0 1) by a deformation experiment (Merkel et al., 2007) [92]. If the B-site substituted $MgSiO_3$ post-perovskite also possesses the (0 0 1) slip plane, the observed S-wave splitting can be fully explained. However, the Pt and Rh doping on $CaIrO_3$ suggest that B-site substitution of different elements into the $MgSiO_3$ post-perovskite can have a marked influence on external morphology of the crystal grains. Thus, the effect of $MgSiO_3$ solid solutions must be taken into account in order to fully explain the observed seismic anisotropy of the Earth. As it is very difficult to determine the external morphology of unquenchable B-site substituted $MgSiO_3$ post-perovskite, the Pt and Rh doped $CaIrO_3$ gives an insight to the driving force of the crystal grain habit of the $MgSiO_3$ solid solutions. Since the slip plane of $MgSiO_3$/$(Mg,Fe)SiO_3$ post-perovskite is (0 0 1) (Ayagi et al., 2010; Merkel et al., 2007) , the crystal plane parallel to the ground is likely to be altered from (0 0 1) to (0 1 0) by the effect of Si-site doping. S-wave propagates along the crystallographic *a*-axis due to the pronounced texture of post-perovskite structure. Fig.8.1 shows the simplified image of the polarized anisotropy of S-wave in the post-perovskite structure for (0 0 1) slip system and (0 1 0) slip system.

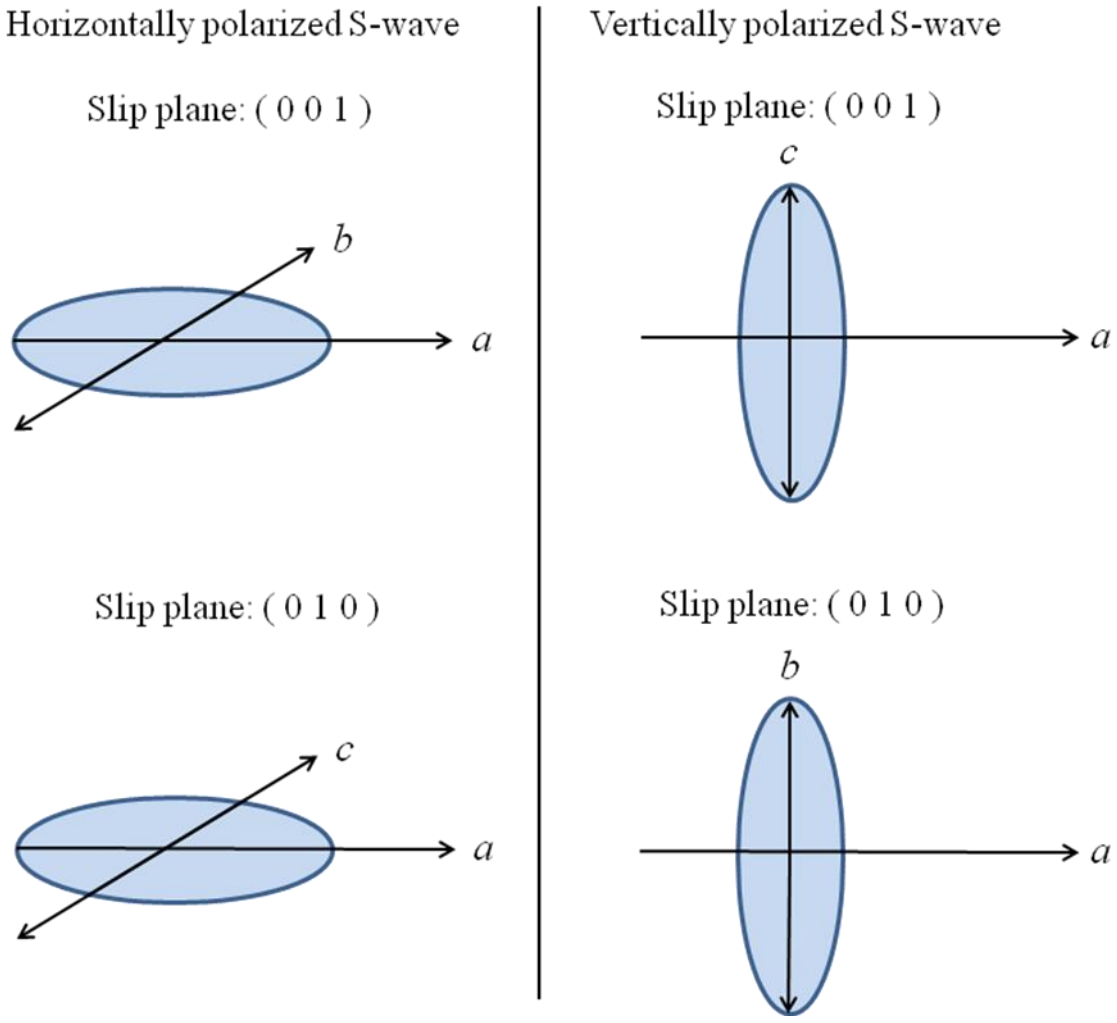

Fig.8.1 Schematic diagram of the polarized anisotropy of S-wave in the post-perovskite structure for the (0 0 1) and (0 1 0) slip system. Ellipsoids show the polarized plane of S-wave. S-wave propagates along the crystallographic *a*-axis, while the shear motion takes place along either *b*-axis or *c*-axis depending on the slip plane and the type of polarization.

When (0 0 1) is the slip plane of post-perovskite structure, the horizontally polarized plane of S-wave possesses [0 1 0] shear motion, while the vertically polarized plane of S-wave possesses [0 0 1] shear motion. Since post-perovskite structure is a layered structure with (0 0 1) as the intralayer, shear motion of [0 1 0] is stiffer than that of [0 0 1], and the [0 1 0] shear has a higher shear modulus. As the S-wave velocity is proportional to the square root of the shear modulus, the horizontally polarized S-wave propagates faster than the vertically polarized S-wave. On the other hand, if (0 1 0) is the slip plane of post-perovskite structure, the horizontally polarized plane of S-wave possesses the [0 0 1] shear motion, while the vertically polarized plane of S-wave possesses the [0 1 0] shear motion, and the vertically polarized S-wave propagates faster than the horizontally polarized S-wave. Thus, Al^{3+}- or Fe^{3+}- substitution of Si-site in the$MgSiO_3$ post-perovskite alters the slip plane from (0 0 1) to (0 1 0), and the seismic anisotropy will be weakened by the decrease of the horizontally polarized S-wave velocity. Therefore, the B-site substitution effect revealed by the texture evolution of $CaIr_{1-x}Pt_xO_3$ series, which could alter the slip plane from (0 0 1) to (0 1 0), implies that the Si-site substitution of the $MgSiO_3$ post-perovskite has to be near-zero or very little in order to be consistent with the seismic anisotropy up to 4 % at the D" layer.

Post-perovskite to perovskite phase transition of $CaIr_{0.5}Pt_{0.5}O_3$ at 60GPa, 1900K was detected from the Raman spectra of the laser-heated sample in a diamond anvil cell. A remarkable increase of 34 % in thermodynamic Grüneisen parameter γ_{th} across the post-perovskite to perovskite transition was estimated from the pressure dependent

Raman-active modes of $CaIr_{0.5}Pt_{0.5}O_3$. This increase of 34 % associated with the phase transition has a similar magnitude to $(Mg,Fe)SiO_3$ (27 %) and $MgGeO_3$ (33 %), suggesting that $CaIr_{0.5}Pt_{0.5}O_3$ is a promising analogue for experimentally simulating the competitive stability between perovskite and post-perovskite phase of magnesium silicates in Earth's lowermost mantle. As the D" topology depends on the core-mantle boundary where the temperature range is less than 200 K different from the temperature that post-perovskite transition takes place, the perovskite to post-perovskite transition can be reversed several times (Monnereau et al, 2009)[9]. Thus, it is important to investigate the factors governing the stability of $MgSiO_3$ post-perovskite at high pressures. The increase of thermodynamic Grüneisen parameter γ_{th} across the post-perovskite to perovskite transition is insensitive to the very different masses of the cations in the B-site ($CaIr_{0.5}Pt_{0.5}O_3$ is compared with $MgGeO_3$), while the increase of γ_{th} across the post-perovskite to perovskite transition is sensitive to the small difference in the masses of the cations in the A-site ($(Mg,Fe)SiO_3$ is compared with $MgGeO_3$). Therefore, the stability of the Mg-site doped $MgSiO_3$ post-perovskite will be greatly affected by the mass of the Fe or Al in the Mg-site. Furthermore, the post-perovskite to perovskite transition is favoured in the case of Mg-site doped $MgSiO_3$ compared to $MgSiO_3$ since the increase of thermodynamic Grüneisen parameter is expected to be smaller due to the larger mean mass of Fe and Al doped Mg-site compared to pure Mg. In other words, the post-perovskite to perovskite transition is enhanced and the post-perovskite phase is destabilized for the Mg-site doped $MgSiO_3$ existing in the D" layer. The estimation from the pressure dependent Raman-active modes of $CaIr_{0.5}Pt_{0.5}O_3$ is reliable since the estimated and directly calculated thermodynamic

Grüneisen parameter γ_{th} from heat capacity show consistent values. Thus, $CaIr_{0.5}Pt_{0.5}O_3$ is potentially a useful analogue of $MgSiO_3$ based post-perovskite systems. The marked effect of Pt substitution stabilising the post-perovskite structure in $CaIr_{1-x}Pt_xO_3$ solid solutions explains why the post-perovskite to perovskite phase transition has not been observed for $CaPtO_3$ in contrast to other quenchable post-perovskite oxides: $CaIrO_3$, $CaRhO_3$ and $CaRuO_3$. This instability of the perovskite phase of Pt doped $CaIrO_3$ suggests the competitive stability between perovskite and post-perovskite phase since Ir^{4+} and Pt^{4+} have similar ionic radii and electronic configuration. Such a competitive stability condition has important implications in Earth Science. The topology of the D" layer of the Earth can only be determined after taking the effect of solid solutions bearing minor elements into account since the Si- site doped $MgSiO_3$ will experience the competitive stability between perovskite and post-perovskite phase.

The temperature-independent paramagnetism above 150 K and small magnetic entropy observed in heat capacity measurements suggests that $CaIrO_3$ is intrinsically a weak itinerant ferromagnetic metal, while electrical resistivity measurements suggest that it is extrinsically a narrow bandgap semiconductor. $CaIrO_3$ undergoes a magnetic transition at 108K and possesses a small saturated magnetic moment of 0.04 μ_B; this also implies that $CaIrO_3$ is an itinerant ferromagnetic metal. Pt substitution of $CaIrO_3$ induces Curie-Weiss paramagnetism and suppresses the magnetic transition temperature, suggesting that disruption of Ir^{4+}- Ir^{4+} metal-metal bonding may play a dominant role on the electronic band structure. The anisotropic crystal structure and pronounced texture of $CaIrO_3$

combined with the Ir^{4+} spin-orbit coupling result in a remarkably large magnetic anisotropy constant of 1.77 x 10^6 Jm^{-3} comparable to values for permanent magnets, suggesting that industrial applications such as magnetic recording can be realized when $CaIrO_3$ post-perovskite is doped with a transition metal with a large electron spin. Thus, compounds on the basis of $CaIrO_3$ open up future opportunities in materials science.

8.2 Future works

Future work, leading on from results presented in this thesis, could be conducted using high pressure/temperature *in-situ* X-ray diffraction measurements in order to further investigate the stability between post-perovskite and perovskite in $CaIr_{1-x}Pt_xO_3$(x = 0.3, 0.5, 0.7) and $CaIr_{1-x}Rh_xO_3$ (x = 0.5).

As I observed a post-perovskite to perovskite phase transition in $CaIr_{0.5}Pt_{0.5}O_3$ in this study at 60GPa, 1900K, it is important to determine and refine the crystal structure of the new perovskite phase of $CaIr_{0.5}Pt_{0.5}O_3$ by high P/T *in-situ* X-ray diffraction measurements. As such a transition has not been observed for $CaPtO_3$, structural refinement of the perovskite phase and phase boundary determination of other $CaIr_{1-x}Pt_xO_3$ solid solutions (x = 0.3, 0.7) will be conducted based on the high P/T *in-situ* X-ray diffraction profile. Also, polytypes between post-perovskite and perovskite structure are expected to be accessible in $CaIr_{1-x}Pt_xO_3$ solid solutions(x = 0.3, 0.7). As an intermediate phase between post-perovskite

and perovskite has been reported for $CaRhO_3$ (Shirako et al., 2009)[93], high P/T *in-situ* X-ray diffraction measurements on $CaIr_{1-x}Rh_xO_3$($x = 0.5$) is of a great interest for finding a new post-perovskite polytype and the transition path of post-perovskite. Since the topology of the D" layer of the Earth can only be determined after taking the effect of $MgSiO_3$ solid solutions, which will experience the sensitive stability between perovskite and post-perovskite phase, it is important to systematically investigate every possible transition path of the post-perovskite phase through the $CaIr_{1-x}Pt_xO_3$ and $CaIr_{1-x}Rh_xO_3$ solid solutions and determine the factors governing the stability of the post-perovskite phase. As the post-perovskite phase of $CaIr_{1-x}Pt_xO_3$ and $CaIr_{1-x}Rh_xO_3$ solid solutions can be quenched to ambient conditions, their stability and new transition paths at high pressures will give insight to the stability of the $MgSiO_3$ post-perovskite and high-pressure phases of $MgSiO_3$ post-perovskite in the extra-solar planets which experience much larger internal pressures (> 200GPa) than those of the D" region of the Earth.

9. Publications

[1] Hirai, S; Sanehira, T; Nishiyama, N; Irifune, T; Klemme, S; Bromiley, G; Attfield, J.P. Tuning of structure, morphology and magnetism in post-perovskite oxide solid solutions, *Chem. Mater.*, **2011**, *23*, 114-121

[2] Hirai, S; Kojima, Y; Ohfuji, H; Nishiyama, N; Irifune, T; Klemme, S; Bromiley, G; Attfield, J.P. High-pressure Raman studies and heat capacity measurements on the $MgSiO_3$ analogue $CaIr_{0.5}Pt_{0.5}O_3$: Implications for the stability of post-perovskite and perovskite in Earth's D” layer, *Phys. Chem. Minerals*, **2011** to be published

10. Acknowledgement

First, I would like to thank my supervisors, Professor J. Paul Attfield, Dr Geoffrey Bromiley, Professor Stephan Klemme and Professor Simon Harley for giving me the precious opportunity and productive advices for conducting PhD research on the physics and chemistry of post-perovskite oxides. I would like to thank Professor Stephan Klemme and Professor Paul Attfield for assigning me the research grant of EPSRC for conducting 3-years' research on the physics and chemistry of post-perovskite oxides. Thanks to the diverse area of studies of my supervisors, I could freely use the multi-disciplinary facilities at Centre for Science at Extreme Conditions, School of Chemistry and School of Geosciences at the University of Edinburgh, and the Institute of Mineralogy at University of Münster, Germany. Such environment helped a lot in studying the post-peorvskite oxides in detail from different directions.

Second, I would like to thank Professor Tetsuo Irifune, Professor Norimasa Nishiyama and Dr Hiroaki Ohfuji for kindly giving me the access to the Geodynamics Research Center, Ehime University, Japan for conducting high-pressure synthesis of post-perovskite oxide solid solutions at 15GPa using the Kawai-type 2000 tonne split-sphere multi-anvil apparatus, and for conducting high-pressure Raman studies of $CaIr_{0.5}Pt_{0.5}O_3$ using a laser-heated four-pin type diamond anvil cell with a pair of bevelled culets.

Finally, I would like to thank the collaborators at School of Geosciences and Centre for Science at Extreme Conditions. Dr Ian Butler at School of Geosciences who is also my

advisor helped me with the piston-cylinder experiment, Dr Nicola Cayzer at School of Geosciences helped me with the SEM experiment, Dr Chris Hayward helped me with the electron microprobe analysis and Michael Hall for polishing the specimens for electron microprobe analysis. I would like to thank Dr Iain Main at School of Geosciences who was the examiner of my first-year report for giving me useful advices about the direction of my PhD research. The research group member of Professor Paul Attfield helped me with smoothly conducting experiments at School of Chemistry and CSEC. Finally, I would like to thank Huei Lu, Dr Wei-tin Chen, Dr Iain Robinson and the people at CSEC for their nice conversations and support during my PhD.

11. References

[1] Murakami, M.; Hirose, K.; Kawamura, K.; Sata, K.; Ohishi, Y. Post-peorvskite phase transition in $MgSiO_3$, *Science*, **2004**, *304*, 855-858

[2] Kesson, S. E.; FitzGerald, J.D.; Shelly, J.M. Mineralogy and dynamics of a pyrolite lower mantle, *Nature*, **1998**, *393*, 253-255

[3] Lay,T. Seismic wave anisotropy in the D" region and its implications, *American Geophysical Union*, **1998**, 299-318

[4] Sidorin, I. ; Gurnis, M.; Helmberger, D.V. Evidence for a ubiquitous seismic discontinuity at the base of the mantle *Science* **1999**, *298*, 1326-1331

[5] Oganov, A.R.; Ono, S. Theoretical and experimental evidence for a post-perovskite phase of $MgSiO_3$ in Earth's D" layer, *Nature*, **2004**, *430*, 445-448

[6] Iitaka, T.; Hirose, K.; Kawamura, K.; Murakami, M. The elasticity of the $MgSiO_3$ post-perovskite phase in the Earth's lowermost mantle, *Nature*, **2004**, *430*, 442-445

[7] Shim, S.; Bengtson, A.; Morgan, D.; Sturhahn, W.; Catalli, K.; Zhao, J.; Lerche, M.; Prakapenka, V.B. Electronic and magnetic structures of the postperovskite-type Fe_2O_3 and implications for planetary magnetic records and deep interiors, *PNAS*, **2009**, *106*, 5508-5512

[8] Santilla ń, J.; Shim, S.; Shen, G.; Prakapenka, V.B. High-pressure phase transition in Mn_2O_3: Application for the crystal structure and preferred orientation of the $CaIrO_3$ type, *Geophys. Res. Lett.*, **2006**, *33*, L15307

[9] Monnereau, M.; Yuen, D.A. Topology of the post-perovskite phase transition and mantle dynamics, *PNAS*, **2007**, *104*, 9156-9161

[10] Hirose, K.; Takafuji, N.; Fujino, K.; Shieh, S.R.; Duffy, T.S. Iron partitioning between perovskite and post-perovskite: A transition electron microscope study, *Am. Mineral.*, **2008**, *93*, 1678-1681

[11] Sinmyo, R.; Hirose, K.; O'Neill, H.S.C.; Okunishi, E. Ferric iron in Al-bearing post-perovskite phase, *Geophys. Res. Lett.*, **2006**, *33*, L12S13

[12] Rodi, F. *Z.* Ternare Oxide Der Ubergangsmetalle. 4. Erdalkaliiridium(4)-Oxide-Kristallstruktur Von $CaIrO_3$, *Anorg.Allg.Chem.*, **1965**, *336*, 17-22

[13] Sarkozy, R.F.; Moeller, C.W.; Chamberland, B.L. The Characterization of Calcium Iridium Oxides *J. Solid State Chem*., **1974**, *9*, 242-246

[14] He, T. The effect of Ru-site dopants on the magnetic properties of $CaRuO_3$, *J.Phys.Condens. Matter*, **2001**, *13*, 8347-8361

[15] Trzebiatowska, B.J. Magnetic and electrical properties of new ternary oxides with rhenium (IV), *Mat. Res.Bul.*, **1978**, *13*, 347-351

[16] Hirai, S.; Welch, M.D; Aguado, F.; Redfern, S.A.T. The crystal structure of $CaIrO_3$ post-perovskite revisited, *Z. Kristallogr.*, **2009**, *224*, 345-350

[17] Ohgushi, K.; Matsushita, Y.; Miyajima, N.; Katsuya, Y.; Tanaka, M.; Izumi, F.; Gotou, H.; Ueda, Y.; Yagi, T. $CaPtO_3$ as a novel post-perovskite oxide, *Phys. Chem. Minerals*, **2008**, *35*, 189-195

[18] Yamaura, K.; Shirako, Y.; Kojitani, H.; Arai, M.; Young, D.P.; Akaogi, M.; Nakashima, M.; Katsumata, T.; Inaguma, Y.; Takayama-Muromachi, E. Synthesis and magnetic and

charge-transport properties of the correlated 4d post-perovskite $CaRhO_3$ *J. Am. Chem. Soc.*, **2009**, *131*, 2722-2726

[19] Kojitani, H.; Shirako, Y.; Akaogi, M. Post-perovskite phase transition in $CaRuO_3$, *Physics of the Earth and Planetary Interiors*, **2007**, *165*, 127–134

[20] Hirai, S. MPhil thesis: *Investigation of the structure of $CaIrO_3$ and post-perovskite structure*, University of Cambridge, **2007**

[21] Syono, Y.; Akimoto, S.; Kohn, K. Structure Relations of Hexagonal Perovskite-Like Compounds ABX_3 at High Pressure, *J.Phys. Soc. Japan*, **1969**, *26*, 993-999

[22] Siegrist, T. The crystal structure of $BaIrO_3$, *J. Less common metals*, **1991**, *170*, 93-99

[23] Chamberland, B.L. A study on the $BaIrO_3$ system, *J. Less common metals*, **1991**, *171*, 377-394

[24] Kuroda, K.; Ishizawa, N.; Mizutani, N.; Kato, M. The crystal structure of α-$SrMnO_3$, *J.Solid State Chem*., **1981**, *38*, 297-299

[25] Longo, J.M. Structure and properties of the high and low pressure forms of $SrIrO_3$, *J. Solid State Chem.*, **1971**, *3*, 174-179

[26] Schmalle, H. The crystal structure of $SrIrO_3$, *Z.Kristallogr.*, **1990**, *191*, 239-247

[27] Oganov, A.R. Anisotropy of Earth's D" layer and stacking faults in the $MgSiO_3$ post-perovskite phase, *Nature*, **2005**, *438*, 1142-1144

[28] Stolen, S.; Tronnes R.G. The perovskite to post-perovskite transition in $CaIrO_3$: Clapeyron slope and changes in bulk and shear moduli by density functional theory, *Physics of the Earth and Planetary Interiors*, **2007**, *164*, 50-62

[29] Hirai, S.; Sanehira, T.; Nishiyama, N.; Irifune, T.; Klemme, S.; Bromiley, G.; Attfield, J.P. Tuning of structure, morphology and magnetism in post-perovskite oxide solid solutions *Chem. Mater.*, **2010** to be published

[30] Kim, B.J.; Jin, H.; Moon, S.J.; Kim, J.Y.; Park, B.G.; Leem, C.S.; Yu, J; Noh, T.W.; Kim,C; S.-J. Oh, S.J.; Park, J.H.; Durairaj, J; Cao, G; Rotenberg, E Novel J_{eff} =1/2 Mott State Induced by Relativistic Spin-Orbit Coupling in Sr_2IrO_4, *Phys. Rev. Lett.*, **2008**, *101*, 076402

[31] Ohgushi, K.; Gotou, H.; Yagi, T.; Kiuchi, Y.; Sakai, F.; Ueda, Y. Metal-Insulator Transition in $Ca_{1-x}Na_xIrO_3$ with Post-Perovskite Structure, *Phys. Rev. B*, **2006**, *74*, 241104

[32] Hirose, K.; Fujita, Y. Clapeyron slope of the post-perovskite phase transition in $CaIrO_3$, *Geophys. Res. Letters*, **2005**, *32*, L13313

[33] Martin, C.D.; Chapman, K.W.; Chupas, P.J.; Prakapenka, V.; Lee, P.L.; Shastri, S.D.; Parise, J.B. Compression, thermal expansion, structure, and instability of $CaIrO_3$, the structure model of $MgSiO_3$ post-perovskite, *Am. Mineral.*, **2007**, *92*, 1048-1053

[34] Martin, C.D.; Smith, R.I.; Marshall, W.G.; Parise, J.B. High-pressure structure and bonding in $CaIrO_3$: The structure model of $MgSiO_3$ post-perovskite investigated with time-of-flight neutron powder diffraction, *Am. Mineral.*,, **2007**, *92*, 1912-1918

[35] Merkel, S.; Kubo, A.; Miyagi, L.; Speziale, S.; Duffy, T.S.; Mao, H.K.; Wenk, H.R. Plastic Deformation of $MgGeO_3$ Post-Perovskite at Lower Mantle Pressure, *Science*, **2006**, *311*, 644-646

[36] Hirose, K.; Kawamura, K.; Ohishi, Y.; Tateno, S.; Sata, N. Stability and equation of state of $MgGeO_3$ post-perovskite phase,

Am. Mineral., **2005**, *90*, 262-265

[37] Kojitani, H.; Furukawa, A.; Akaogi, M. Thermochemistry and high-pressure equilibria of the post-perovskite phase transition in $CaIrO_3$, *Am. Mineral.*, **2007**, *92*, 229-232

[38] Hustoft, J.; Shim, S.; Kubo, A.; Nishiyama, N. Raman spectroscopy of $CaIrO_3$ postperovskite up to 30 GPa, *Am. Mineral.*, **2008**, *93*, 1654–1658

[39] Lindsay-Scott, A.; Wood, I.G.; Dobson D.P.; Voˇcadlo, L; Brodholt, J.P.; Crichton, W.; Hanfland, M.; Taniguchi, T. The isothermal equation of state of $CaPtO_3$ post-perovskite to 40 GPa *Physics of the Earth and Planetary Interiors*, **2010** to be published

[40] Kim, B.J.; Ohsumi, H.; Komesu, T.; Sakai, S.; Morita, T.; Takagi, H.; Arima, T. Phase-Sensitive Observation of a Spin-Orbital Mott State in Sr_2IrO_4, *Science*, **2009**, *323*, 1329-1332

[41] Moon, S.J. Dimensionality-Controlled Insulator-Metal Transition and Correlated Metallic State in 5d Transition Metal Oxides $Sr_{n+1}Ir_nO_{3n+1}$ (n = 1,2, and ∞) *Phys. Rev. Lett.*, **2008**, *101*, 226402

[42] Glazer, A.M. The classification of tilted octahedra in perovskite, *Acta Cryst.B*, **1972**, *28*, 3384-3392

[43] Tsuchiya, J.; Tsuchiya, T.; Wentzcovitch, R.M. Transition from the Rh_2O_3(II)-to-$CaIrO_3$ structure and the high-pressure-temperature phase diagram of alumina, *Phys. Rev. B*, **2005**, *72*, 020103

[44] Oganov, A.R.; Ono, S. The high-pressure phase of alumina and implications for Earth's D" layer, *PNAS*, **2005**, *102*, 10828-10831

[45] Shannon, R. D.; Prewitt, C.T. Synthesis and structure of a new high-pressure form of Rh_2O_3, *J.Solid State Chem*., **1970**, *2*, 134-136

[46] Funamori, N.; Jeanloz, R. High-Pressure Transformation of Al_2O_3, *Science*, **1997**, *278*, 1109-1111

[47] Lin, J.F.; Degtyareva, O.; Prewitt, C.T.; Dera, P.; Sata, N.; Gregoryanz, E.; Mao, H.K.; Hemley, R.J. Crystal structure of a high-pressure/high-temperature phase of alumina by in situ X-ray diffraction, *Nat. Mater*., **2004**, *3*, 389-393

[48] Adachi, G.; Imanaka, N The Binary Rare Earth Oxides, *Chem. Rev.*, **1998**, *98*, 1479-1514

[49] Meyer, C. Mössbauer and energy-dispersive x-ray-diffraction studies of the pressure-induced crystallographic phase transition in *C*-type Yb_2O_3, ***Phys***. *Rev. B*, **1995**, *51*, 12187-12193

[50] Akahama, Y.; Kawamura, H. High-pressure Raman spectroscopy of diamond anvils to 250 GPa: Method for pressure determination in the multimegabar pressure range, *J. Appl. Phys*, **2004**, *96*, 3748-3751

[51] Subramanian, N.; Chandra Shekar, N.V.; Sanjay Kumar, N.R.; Sahu, P.C. Development of laser-heated diamond anvil cell facility for synthesis of novel materials, *Current Science*, **2006**, *91*, 175-182

[52] Ming, L.C.; Basset, W.A. Laser heating in the diamond anvil press up to 2000 C sustained and 3000 C pulsed at pressures up to 260 kilobars, *Rev.Sci.Instrum.*, **1974**, *45*, 1115-1118

[53] Raman, C.V. A New Type of Secondary Radiation, *Nature,* **1928**, *121*, 501-502

[54] Kawai, N.; Endo, S. The generation of ultrahigh hydrostatic pressures by a split sphere apparatus, *Rev.Sci.Instrum.*, **1970**, *41*, 1178-1181

[55] Venkateswaran, C.; Anbukumaran, K.; Jaya, V.N.; Natarajan, S. Design and performance of a belt-type high pressure, high temperature apparatus, *Rev. Sci. Instrum.*, **1997**, *68*, 189-192

[56] Yagi, T.; Akaogi, M.; Shimomura, O. In Situ Observation of the Olivine-Spinel Phase Transformation in Fe_2SiO_4 using Synchrotron Radiation, *J. Geophys. Res.*, **1987**, *92*, 6207–6213

[57] Frost, D.J. $(Mg,Fe)_2SiO_4$ Phase Transformations in the Transition Zone, *Earth Planet. Sci. Lett.*, **2003**, *216*, 313–328

[58] Josephson, B.D. Possible New Effects in Superconducting Tunnelling, *Phys. Lett.*, **1962**, *1*, 251-253

[59] Anderson, P.W.; Rowell, J.M. Probable observation of the Josephson superconducting tunneling effect, *Phys. Rev. Lett.*, **1963**, *10*, 230-232

[60] Miyajima, N.; Ohgushi, K.; Ichihara, M.; Yagi, T. Crystal morphology and dislocation microstructures of $CaIrO_3$, A TEM study of an analogue of the $MgSiO_3$ post perovskite phase, *Geophys. Res. Lett.*, **2006**, *33*, L12302

[61] McDaniel, C. L.; Schneider, S.J. Phase relations in the CaO-IrO_2-Ir system in air, *J. Solid State Chem.*, **1972**, *4*, 275– 280

[62] Lindsay-Scott, A.; Wood, I.G.; Dobson, D.P. Thermal expansion of $CaIrO_3$ determined by X-ray powder diffraction, *Physics of the Earth and Planetary Interiors*, **2007**, *162*, 140-148

[63] Park, C.I.; Condrate, R.A.; Snyder, R. L. The Raman Spectra of Perovskite-Structured Alkaline Earth Hafnates, *Appl. Spectr.*, **1976**, *30*, 352-353

[64] Abrashev, M.V.; Bäckström, J.; Börjesson, L.; Popov, V.N.; Chakalov, R.A.; Kolev, N.; Meng, R.L.; Iliev, M.N. Raman spectroscopy of $CaMnO_3$: Mode assignment and relationship between Raman line intensities and structural distortions, *Phys. Rev. B*, **2002**, *65*, 184301

[65] Shim, S.; Kubo, A.; Duffy, T.S. Raman spectroscopy of perovskite and post-perovskite phases of $MgGeO_3$ to 123 GPa *Earth and Planet. Sci Lett*., **2007**, *260*, 166-178

[66] Chopelas, A.; Boehler, R..;Ko, T. Thermodynamics and behaviour of γ-Mg_2SiO_4 at high pressure: Implications for Mg_2SiO_4 phase equilibrium *Phys. Chem. Minerals*, **1994**, *21*, 351–359.

[67] Tuchiya, T.; Tuchiya, J.; Umemoto, K.; Wentzcovitch, R.M. Elasticity of post-perovskite $MgSiO_3$, *Geophys. Res. Lett*., **2004**, *31*, L14603

[68] Kubo, A.; Kiefer, B.; Shim, S.; Shen, G.; Prakapenka, V.B. ; Duffy, T.S. Rietveld structure refinements of $MgGeO_3$ post-perovskite phase to 1 Mbar, *Am. Mineral.*, **2008**, *93*, 965-976

[69] Shim, S.; Catalli, K.; Hustoft, J.; Kubo, A.; Prakapenka, V.B.; Caldwell, W.A.; Kunz, M. Crystal structure and thermoelastic properties of $(Mg_{0.91}Fe_{0.09})SiO_3$ postperovskite up to 135 GPa and 2700 K *PNAS*, **2008**, *105*, 7382–7386

[70] Inaguma,Y.; Hasumi, K.; Yoshida, M.; Ohba, T.; Katsumata, T. High-pressure synthesis, structure, and characterization of a post-perovskite $CaPtO_3$ with $CaIrO_3$-type structure, *Inorg. Chem.*, **2008**, *47*, 1868-1870

[71] Mizoguchi, H.; Woodward, P.M.; Byeon, S.; Parise, J.B. Polymorphism in $NaSbO_3$: Structure and bonding in ternary metal oxides, *J. Am. Chem. Soc.*, **2004**, *126*, 3175-3184

[72] Larson, A.C.; Von Dreele, R.B. *General Structure Analysis System*, Los Alamos National Laboratory Report, **2000**, 86-748

[73] Matar, S.F.; Demazeau, G.; Largeteau, A. DFT study of electronic and magnetic structure of perovskite and post-perovskite $CaRhO_3$, *Solid State Sciences*, **2010,** *12*, 373-378

[74] Grillo, M.E. Electronic control of the stability of rutile- versus corundum-type structures of ruthenium and rhodium oxides, *Comput. Mater. Sci.*, **2005**, *33*, 83-91

[75] Shimony, Y.; Ben-dor, L. Metallic interactions in dioxides with rutile and rutile related structures, *J. Mater. Sci. Lett.*, **1983**, *2*, 558-560

[76] Ivanovskii, A.L.; Chupakhina, T.I.; Zubkov, V.G; Tyutyunnik, A.P.; Krasilnikov, V.N.; Bazuev, G.V.; Okatov S.V.; Lichtenstein, A.I. Structure and electronic properties of new rutile-like rhenium (IV) dioxide ReO_2, *Phys. Lett. A*, **2005**, *348*, 66-70

[77] Brown, I.D. *The chemical bond in inorganic chemistry*, Oxford University Press, **2002**

[78] Alonso, J.A.; Martinez-Lope, M.J.; Casais, M.T. Evolution of the Jahn-Teller distortion of MnO_6 octahedra in $RMnO_3$ perovskites (R= Pr, Nd, Dy, Tb, Ho, Er, Y), *Inorg. Chem.*, **2000**, *39*, 917-923

[79] Brown, I.D. Chemical and steric constraints in inorganic solids, *Acta Cryst. B*, **1992**, *48*, 553-572

[80] Preiser, C.; Losel, J.; Brown, I.D.; Kunz, M.; Skowron, A. Long-range Coulomb forces and localized bonds, *Acta Cryst. B*, **1999,** *55*, 698-711

[81] Salinas-Sanchez, A.; Garcia-Munoz, J.L.; Rodriguez-Carvajal, J.; Saez-Puche, R.; Martinez, J.L. Structural characterization of R_2BaCuO_5 (*R* = Y, Lu, Yb, Tm, Er, Ho, Dy, Gd, Eu and Sm) oxides by X-ray and neutron diffraction, *J. Solid State Chem.*, **1992**, *100*, 201-211

[82] Von Dreele, R.B. Quantitative texture analysis by Rietveld refinement, *J.Appl. Crystallogr.*, **1997**, *30*, 517-525

[83] Goodenough, J.B. Direct Cation-Cation Interaction in Several Oxides, *Phys. Rev.*, **1960**, *117*, 1442-1451

[84] Shimizu, M. Itinerant electron magnetism, *Rep. Prog. Phys.*, **1981**, *44*, 329-409

[85] Moriya, T. Recent progress in the theory of itinerant electron magnetism, *J. Magn. Magn. Mater*., **1979**, *14*, 1-46

[86] Nunes, W.C.; Folly, W.S.D; Sinnecker, J.P.; Novak, M.A. Temperature dependence of the coercive field in single-domain particle systems, *Phys. Rev. B.*, **2004**, *70*, 014419

[87] Blundell, S. *Magnetism in Condensed Matter*, Oxford University Press, **2001**, 128-136

[88] Haskel, D.; Lang, J. C.; Islam, Z.; Cady, A.; Srajer, G.; Veenendaal, M.; Canfield, P.C. Atomic Origin of Magnetocrystalline Anisotropy in $Nd_2Fe_{14}B$, *Phys. Rev. Lett.*, **2005**, *95*, 217207

[89] Ogawa, S. Electrical resistivity of weak itinerant ferromagnet $ZrZn_2$, *J. Phys. Soc. Jpn.*, **1976**, *40*, 1007-1009

[90] Wagner, D.; Brauneck, W.; Solontsov, A.; Shimizu, M. *Itinerant electron magnetism: fluctuation effects*, Springer, **1998**, 123-150

[91] Miyagi, L.; Kantipanyacharoen, W.; Kaercher, P.; Lee, K.K.M.; Wenk, H.R. Slip plane systems in $MgSiO_3$ postperovskite: Implications for D" anisotropy, *Science*, **2010**, *329*, 1639–1641

[92] Merkel, S.; McNamara, A.K.; Kubo, A.; Speziale, S.; Miyagi, L.; Meng, Y.; Duffy, T.S.; Wenk, H.R. Deformation of $(Mg,Fe)SiO_3$ postperovskite and D″ anisotropy, *Science*, **2007**, *316*, 1729–1732

[93] Shirako, Y.; Kojitani, H.; Akaogi, M.; Yamaura, K.; Takayama-Muromachi, E. High-pressure phase transitions of $CaRhO_3$ perovskite, *Phys. Chem. Minerals*, **2009**, *36*, 455-462